

**Quantum control of dynamics of particles in a periodic
lattice potential**

by

Ping Xiang

Bachelor of Science, Nankai University, 2007

A THESIS SUBMITTED IN PARTIAL FULFILLMENT
OF THE REQUIREMENTS FOR THE DEGREE OF

Doctor of Philosophy

in

THE FACULTY OF GRADUATE STUDIES
(Chemistry)

The University Of British Columbia
(Vancouver)

June 2014

© Ping Xiang, 2014

Abstract

This document provides brief instructions for using the `ubcdiss` class to write a UBC-conformant dissertation in L^AT_EX. This document is itself written using the `ubcdiss` class and is intended to serve as an example of writing a dissertation in L^AT_EX. This document has embedded Unique Resource Locators (URLS) and is intended to be viewed using a computer-based Portable Document Format (PDF) reader.

Note: Abstracts should generally try to avoid using acronyms.

Note: at University of British Columbia (UBC), both the The Faculty of Graduate Studies (FOGS) Ph.D. defence programme and the Library's online submission system restricts abstracts to 350 words.

Preface

At UBC, a preface may be required. Be sure to check the FOGS guidelines as they may have specific content to be included.

Table of Contents

Abstract	ii
Preface	iii
Table of Contents	iv
List of Tables	vii
List of Figures	viii
Glossary	xv
Acknowledgments	xvi
1 Introduction	1
1.1 Ultracold atoms and molecules	1
2 Background material	2
2.1 Review of angular momentum theory	2
2.2 Dipole-dipole interaction	10
2.3 Diatomic molecule in DC field	10
2.4 Diatomic molecule in AC field	10
2.5 Introduction to exciton	10
3 Tunable exciton interactions in optical lattices with polar molecules	13
3.1 Introduction	13

3.2	Exciton–exciton interactions in an optical lattice	15
3.3	Biexcitons	17
3.3.1	Method to calculate biexciton energies	17
3.3.2	Analytical derivation of biexciton wavefunction	25
3.3.3	Properties of biexciton states	32
3.4	Non-optical creation of biexcitons	36
3.5	Extension to exciton trimers	40
3.6	Discussion	44
4	Non-adiabatic control of quantum energy transfer in ordered and disordered arrays	46
4.1	Introduction	46
4.2	Sudden phase transformation	49
4.2.1	Group velocity of wave packet	50
4.2.2	Phase kicking in quasimomentum space	52
4.3	Focusing of a delocalized excitation	57
4.3.1	Focusing to a single site	58
4.3.2	Focusing a broad wavepacket in coordinate space	60
4.3.3	Focusing a plane wave in coordinate space	64
4.3.4	Numerical results	66
4.4	Experimental feasibility of phase transformation	69
4.4.1	Supressing spontaneous emission in system of ultracold atoms	69
4.4.2	Phase kicking in system of ultracold molecules	71
4.4.3	Focusing in system of ultracold molecules	76
4.5	Control of energy transfer in dipolar systems	79
4.5.1	The effect of long-range interaction	80
4.5.2	Anisotropy of dipolar interaction	81
4.5.3	Computation details	83
4.6	Energy transfer in the presence of vacancies	93
4.7	Focusing in the presence of strong disorder	95
4.8	Conclusion	101

5 Lattice Green's function of two-particle state	104
5.1 Introduction	104
5.2 Equation of motion for Green's function	104
5.3 Recursive calculation of Green's function	107
5.3.1 In the nearest neighbor approximation	107
5.3.2 Extension to long-range interaction	113
5.3.3 Extension to high-dimensional system	116
5.3.4 Advantages of the recursive method	117
5.4 The tunneling of biexciton state through disorders	120
5.5 Conclusion	120
Bibliography	121
A Supporting Materials	132

List of Tables

List of Figures

Figure 3.4	Population dynamics for the transition from $ g\rangle \rightarrow f\rangle$ exciton (middle panel) and from an f state localized on a single molecule (lower panel) to coherent $ g\rangle \rightarrow e\rangle$ excitons and biexcitons. The green dashed curves denote the population accumulated in the pairs of non-bound $ g\rangle \rightarrow e\rangle$ exciton states, the red solid curves the biexciton state and the blue dot-dashed curves the f state. The shaded region in the upper panel encapsulates the band of the continuum two-exciton states. The calculation is for a 1D ensemble of $N_{mol} = 501$ LiCs molecules on an optical lattice with lattice separation $a = 400$ nm. The electric field of magnitude 6.88 kV/cm is perpendicular to the molecular array.	38
Figure 3.5	Three-excitation spectra of a 1D array of molecules on an optical lattice. The calculation is done for a system of 20 lattice sites with the hopping interaction $J = 10$ kHz and the dynamic interaction $D = 30$ kHz. The black dots represent energies of all three-exciton states, the red curves denote the boundaries of energy continuum of three free excitons, and the blue curves represent the boundaries of energy continuum for a biexciton plus a free exciton.	44
Figure 4.1	The dispersion curve of an exciton. The interaction between site m and site n is proportional to $1/ n - m ^3$	52

Figure 4.2 Example of controlled energy transfer in a one-dimensional array of quantum monomers subjected to a linear phase transformation. The graph illustrates the evolution of the exciton wave packet centered at $k = 0$ and initially positioned at the center of the array. The phase of the wave function is shown by color. The brightness of color corresponds to the amplitude of the excitation with white color corresponding to zero amplitude. The calculation is for a one-dimensional array of 201 monomers with $\alpha = 22.83$ kHz and $\Delta E_{e-g} = 12.14$ GHz, and the linear phase transformation $\Phi_n \simeq \Phi_0 - 1.29n$. The corresponding experimental setup is illustrated in figure (4.6) . . .

55

Figure 4.3 “Bloch oscillation” of the exciton wave packet in the momentum and coordinate spaces. The phase of the wave function is shown by color as in figure (4.2). A low laser intensity of 10^6 W/cm 2 is used and all other parameters are the same as in figure (4.2). Part (a) shows that the wave packet moves in k space in response to the linear laser field. However, since the wave vector is limited in the first Brillouin zone, when the wave packet reaches $-\pi$ or π , it disappears at the boundary and reappears at the other boundary. Part (b) presents the motion of the wave packet in coordinate space in accordance with the phase kicking in k space. Note that the wave packet spreads in both the momentum and coordinate spaces because the laser intensity profile along the molecular array is not perfect and this is amplified over extended time period.

56

Figure 4.4	Focusing of a completely delocalized collective excitation (panels a and b) and a broad Gaussian wave packet of Frenkel excitons (panels c and d) in a one-dimensional array using the quadratic phase transformations at $t = 0$ as described in text. In panels (b) and (d), the excitation probability distribution is displayed by color. The dashed lines show the initial distribution magnified by 20 and 5 respectively in (a) and (c). The solid curves in panels (a) and (c) correspond to two different phase transformations focusing the same wave packet onto different parts of the array. The calculations are performed with the same parameters α , a , and ΔE_{e-g} as in Figure 4.2. The results are computed with all couplings accounted for.	67
Figure 4.5	Focusing of a delocalized excitation in a 2D array shown at $t = 0$ in panel (a) onto different parts of the lattice (panels b–d). For better visualization, the probability distribution in panel (a) is magnified by a factor of 60. The calculations are performed with the same parameters α , a , and ΔE_{e-g} as in Figure 4.2 and the quadratic phase transformation at $t = 0$	68
Figure 4.6	The experimental setup for the calculation corresponding to figure (4.2). A 1D array of LiCs molecules trapped on an optical lattice with lattice constant $a = 400$ nm is subjected to a homogeneous DC field of 1 kV/cm directed perpendicular to the intermolecular axis. The kicking potential leading to the phase transformation presented by equation (4.54) can be provided by a $\lambda = 1064$ nm Gaussian laser beam that is linearly polarized in the direction of the DC field, with the propagation direction along the array axis, focused to a radius of 5 μm , with the intensity at the focus equal to 10^7 W/cm^2 . The laser pulse is on between 0 and 3 μs	74

Figure 4.7 An illustration to show the orientations of 1D and 2D molecular arrays inside the gaussian beam. (a): the 1D lattice lies along the x -axis of the $z = 0$ plane and the DC field is at some angle with the x -axis such that the coupling α between molecules is negative. (b): the 2D square lattice is at the center of the $z = 0$ plane and the DC field is at 45° degree with the x -axis. In both cases, the laser is linearly polarized along the direction of the DC field.

77

Figure 4.8 Control of excitation transfer in a 1D many-body system with dipolar interactions by varying the direction of an external electric field. Panel (a): Exciton dispersion curves for a 1D ensemble of diatomic molecules on an optical lattice for different angles θ between the direction of the external DC electric field and the axis of the molecular array. In 1D, the coupling $\alpha \propto (1/3 - \cos^2 \theta)$. Panel (b): Propagation of a wave packet centered at $ak = -\pi/3$ controlled by tuning the electric field direction. Thin dotted line depicts the corresponding angle variations with time. The brightness of color corresponds to the probability of the excitation.

82

Figure 4.9 Control of excitation transfer in a 2D many-body system with dipolar interactions by varying the direction of an external electric field. Panels (a) and (b) show the trajectories of the center of an exciton wave packet in a 2D lattice during the time from 0 to 3 ms; Panels (c) and (d) represent the changing of the dressing DC field orientation (θ, ϕ) associated with (a) and (b) respectively. The initial wave packet is a 2D Gaussian distribution centered around $ak_x = ak_y = \pi/2$ and has a width of ~ 60 lattice sites in coordinate space. The magnitude of the DC field is fixed to 6 kV/cm while its direction is changing. The calculations are done for a 2D array of LiCs molecules in a lattice with $a = 400$ nm.

84

Figure 4.10 The orientations of the DC field and molecular arrays in the coordinate systems. (a): The DC field is along the z -axis and the 1D molecular array is in the direction represented by θ_R and ϕ_R . (b): The 2D molecular array is on the XY plane and the orientation of DC field is represented by (θ, ϕ) . For clarity, we have only drawn the molecules (as blue dots) along a particular axis which is at angle γ with the X -axis. It is to be understood that there are also other intermolecular axes which are at different angles with the X -axis. Note part (a) and part (b) have different coordinate systems and the meaning of (θ_R, ϕ_R) is different from that of (θ, ϕ) . In fact, the angle θ_R between the DC field and the molecular array in (b) is related to θ and ϕ by $\cos \theta_R = \cos \theta \cos(\phi - \gamma)$.	86
Figure 4.11 Enhancement factors η (red symbols) and χ (blue symbols) as functions of vacancy percentage in a 2D lattices. See text for the definitions of η and χ . The error bars are for 95% of confidence interval.	94
Figure 4.12 Time snapshots of a collective excitation in a 2D array with a vacancy concentration of 10 % (a) The distribution of the vacant sites; (b) The initial probability distribution of the excited state; (c) The probability distribution of the excitation at the focusing time when the focusing scheme is applied. The focusing time is found numerically as the time when the probability at the target molecule (71, 71) reaches maximum for a given phase transformation. (d) The probability distribution of the wave function at the focusing time when the focusing scheme is not applied. The calculations are performed with the same parameters as in Figure 4.5. The probabilities in (b) and (d) are magnified by 16 and 6 respectively.	96

Figure 4.13 Focusing of a collective excitation in a strongly disordered system with 60% of lattice sites unoccupied. Panel (a) shows different phases applied to different blocks of the lattice before the time evolution. (b) The initial probability distribution of the excited state. (c) The probability distribution of the excited state at the focusing time $T = 3$ ms with the phase transformation depicted in panel (a) before the time evolution. (d) The probability distribution of the excited state at the focusing time $T = 3$ ms with no phase transformation applied. The calculations are performed with the same parameters as in Figure 4.5. The probabilities in (b) and (d) are magnified by 60 and 5, respectively.

99

Figure 4.14 Efficiency of focusing collective excitations in strongly disordered 2D lattices. The molecular array is divided into 400 blocks as shown in Fig.4.13(a). The focusing time t_* is arbitrarily set to 4 ms. For each realization of disorder, we use Eq.(4.99) with $T = t_*$ to find the phase mask applied to different blocks. Shown are the enhancement factors η (red symbols) defined in Eq.(4.90), as a function of the vacancy percentage. The error bars are for 95% confidence interval. . . . 100

Glossary

This glossary uses the handy `acronym` package to automatically maintain the glossary. It uses the package's `printonlyused` option to include only those acronyms explicitly referenced in the `LATEX` source.

FOGS The Faculty of Graduate Studies

PDF Portable Document Format

URL Unique Resource Locator, used to describe a means for obtaining some resource on the world wide web

Acknowledgments

Thank those people who helped you.

Don't forget your parents or loved ones.

You may wish to acknowledge your funding sources.

Chapter 1

Introduction

1.1 Ultracold atoms and molecules

Chapter 2

Background material

This chapter briefly outlines the background knowledge that is directly related to the research in later chapters. Instead of giving a comprehensive picture as various books have already done, we take a pragmatic approach that is more concerned with numerical calculations and intuitive understanding.

2.1 Review of angular momentum theory

The energy difference between the excited state and the ground state, Δ_{eg} can be easily calculated by diagonalizing the total Hamiltonian including the external potential. We know how to calculate the potential due to dipole-dipole interaction

$$\hat{V}_{dd} = \left(\frac{1}{R^3} \right) [\mathbf{d}_A \cdot \mathbf{d}_B - 3(\mathbf{d}_A \cdot \hat{\mathbf{R}})(\mathbf{d}_B \cdot \hat{\mathbf{R}})] ,$$

(\mathbf{R} is the vector connecting the centers of mass of two molecules, and $\hat{\mathbf{R}}$ is an unit vector in the direction of \mathbf{R}),

In this appendix, we will calculate the dipole-dipole interaction between two molecules by using the theory of angular momentum. The treatment of the theory of angular momentum is simplified so that only the necessary part that are directly used in the derivation of dipole-dipole interaction is covered. The structure of this appendix is unconventional. We starts with a problem and then develop the techniques to solve it. In a sense, the appendix is a series of problem-solving

blocks. However, in order not to interrupt the logic of problem solving, we will not separate them into different subsections.

We have two molecules A and B, which are in states $|N_A M_A\rangle$ and $|N_B M_B\rangle$ respectively. In free space, the molecules can rotate along the axis connecting their center of mass, then their state are expressed by

$$|N_A M_A\rangle |N_B M_B\rangle |lm\rangle ,$$

where l is the total angular momentum of A and B together.

However, in solid state or optical lattices, the position of molecules are fixed to a good approximation, they cannot rotate along that axis. In this case, their states are given by $|N_A M_A\rangle |N_B M_B\rangle$ if there is no interaction between them. If we consider the interaction between the two molecules, we can always use $|N_A M_A\rangle |N_B M_B\rangle$ as basis set. By expanding the Hamiltonian in this basis set and diagonalizing it, we can get the new eigenstates.

As the first step, we have to know what the interaction between the two molecules is. If A has a permanent dipole of \mathbf{d}_A and B has a permanent dipole of \mathbf{d}_B and the vector connecting their centers of mass is \mathbf{R} , then the dipole-dipole interaction between A and B is given by

$$\hat{V}_{dd} = \left(\frac{1}{R^3} \right) [\mathbf{d}_A \cdot \mathbf{d}_B - 3(\mathbf{d}_A \cdot \hat{\mathbf{R}})(\mathbf{d}_B \cdot \hat{\mathbf{R}})] . \quad (2.1)$$

Here we only consider the dipole moment, there also exists quadrupole, octopole, ..., etc., but their magnitudes are so small that we can ignore them at large distances, say, 400 nm. Our final goal is to evaluate the matrix element $\langle N_A M_A | \langle N_B M_B | \hat{V}_{dd} | N'_A M'_A \rangle | N'_B M'_B \rangle$. The general scheme to calculate the matrix elements is based on the fact that the dipole-dipole operator (Eq. (2.1)) can be expressed in terms of harmonics operators. Then its matrix elements can be written in terms of 3-j symbols, which can be calculated numerically.

We first consider the simpler term in Eq. (2.1), $\mathbf{d}_A \cdot \mathbf{d}_B$, which can be expressed in terms of a tensor product:

$$\mathbf{d}_A \cdot \mathbf{d}_B = -\sqrt{3} \left[\mathbf{d}_A^{(1)} \otimes \mathbf{d}_B^{(1)} \right]_0^{(0)} . \quad (2.2)$$

But why should we do that? The answer will become clear later when you see the tensor product is related to spherical harmonics. Now, the task is to prove Eq. (2.2). The proof is enclosed between two straight lines.

Based on the property of tensor product, we have

$$\left[A^{(1)} \otimes B^{(1)} \right]_q^{(k)} = \sum_m \langle 1m, 1 q-m | kq \rangle A(1, m) B(1, q-m) , \quad (2.3)$$

where the superscript (k) is the rank of the tensor. A tensor T of rank one is a vector operator. It consists of three operators

$$T(1, 1) = -\frac{1}{\sqrt{2}}(x + iy) , \quad (2.4)$$

$$T(1, 0) = z , \quad (2.5)$$

and

$$T(1, -1) = \frac{1}{\sqrt{2}}(x - iy) . \quad (2.6)$$

The intuitive understanding of Eq. (2.3) is that two angular momentums $j_1 = 1$ and $j_2 = 1$ couple to give rise to another angular momentum $j_3 = k$ with the projection along some direction to be q .

In order to know the relation between $\mathbf{d}_A \cdot \mathbf{d}_B$ and $\left[\mathbf{d}_A^{(1)} \otimes \mathbf{d}_B^{(1)} \right]_0^{(0)}$, we need to calculate $\langle 1m, 1 q-m | kq \rangle$ in Eq. (2.3). They are the Clebsch-Gordan coefficients, which appear when you express the couple representation $|j_1 j_2 jm\rangle$ in terms of the uncouple representation $|j_1 m_1\rangle |j_2 m_2\rangle$. Due to symmetry consideration, it is often convenient to expressed the coefficients by the 3-j symbols. The relation between Clebsch-Gordan coefficient and 3-j symbol is given by the following two equations:

$$\begin{pmatrix} j_1 & j_2 & j_3 \\ m_1 & m_2 & m_3 \end{pmatrix} \equiv (-1)^{j_1-j_2-m_3} (2j_3+1)^{-\frac{1}{2}} \langle j_1 m_1, j_2 m_2 | j_3 - m_3 \rangle , \quad (2.7)$$

$$\langle j_1 m_1, j_2 m_2 | j_3 - m_3 \rangle \equiv (-1)^{j_1-j_2+m_3} (2j_3+1)^{\frac{1}{2}} \begin{pmatrix} j_1 & j_2 & j_3 \\ m_1 & m_2 & -m_3 \end{pmatrix} . \quad (2.8)$$

The 3-j symbols are more symmetric than Clebsch-Gordan coefficients. They have the following important property:

$$\left\{ \begin{array}{ccc} j_1 & j_2 & j_3 \\ m_1 & m_2 & m_3 \end{array} \right\} = 0 \quad \text{unless } m_1 + m_2 + m_3 = 0 \quad (2.9)$$

which physically means that only certain angular momentum eigenstates $|j, m\rangle$ are coupled. An even permutation of the columns of 3-j symbol does not change its value and an odd permutation multiplier the initial value by $(-1)^{j_1+j_2+j_3}$. Moreover,

$$\left\{ \begin{array}{ccc} j_1 & j_2 & j_3 \\ m_1 & m_2 & m_3 \end{array} \right\} = (-1)^{j_1+j_2+j_3} \left\{ \begin{array}{ccc} j_1 & j_2 & j_3 \\ -m_1 & -m_2 & -m_3 \end{array} \right\} \quad (2.10)$$

This implies

$$\left\{ \begin{array}{ccc} j_1 & j_2 & j_3 \\ 0 & 0 & 0 \end{array} \right\} = 0 \quad \text{unless } j_1 + j_2 + j_3 = \text{even.} \quad (2.11)$$

First, we consider the case where $k = 1$ in Eq. (2.3), that is $\left[\mathbf{d}_A^{(1)} \otimes \mathbf{d}_B^{(1)} \right]_0^{(0)}$. Based on Eq. (2.3), we obtain

$$\begin{aligned} \left[\mathbf{d}_A^{(1)} \otimes \mathbf{d}_B^{(1)} \right]_0^{(0)} &= \sum_{m=-1,0,1} \langle 1m, 1-m | 00 \rangle \mathbf{d}_A(1, m) \mathbf{d}_B(1, -m) \\ &= \langle 11, 1-1 | 00 \rangle \mathbf{d}_A(1, 1) \mathbf{d}_B(1, -1) + \langle 10, 10 | 00 \rangle \mathbf{d}_A(1, 0) \mathbf{d}_B(1, 0) \\ &\quad + \langle 1-1, 11 | 00 \rangle \mathbf{d}_A(1, -1) \mathbf{d}_B(1, 1) \\ &= \frac{1}{\sqrt{3}} \mathbf{d}_A(1, 1) \mathbf{d}_B(1, -1) - \frac{1}{\sqrt{3}} \mathbf{d}_A(1, 0) \mathbf{d}_B(1, 0) + \frac{1}{\sqrt{3}} \mathbf{d}_A(1, -1) \mathbf{d}_B(1, 1) \end{aligned} \quad (2.12)$$

(Mathematica can be used to evaluate the Clebsch-Gordan coefficients.) Substituting Eq. (2.4), (2.5) and (2.6) into the above equation, we obtain

$$\left[\mathbf{d}_A^{(1)} \otimes \mathbf{d}_B^{(1)} \right]_0^{(0)} = -\frac{1}{\sqrt{3}} (\mathbf{d}_{A,x} \mathbf{d}_{B,x} + \mathbf{d}_{A,y} \mathbf{d}_{B,y} + \mathbf{d}_{A,z} \mathbf{d}_{B,z}) = -\frac{1}{\sqrt{3}} \mathbf{d}_A \cdot \mathbf{d}_B . \quad (2.13)$$

Therefore, the tensor product of rank $k = 0$ is related to the scalar product. Similarly, it can be shown that the tensor product of rank $k = 1$ is related to the cross product.

$$\left[A^{(1)} \otimes B^{(1)} \right]_q^{(k)} = (\mathbf{A} \times \mathbf{B}) \cdot \hat{\mathbf{e}}_q , \quad (2.14)$$

where

$$\begin{aligned} \hat{\mathbf{e}}_{+1} &= -\frac{1}{\sqrt{2}}(\hat{\mathbf{X}} + i\hat{\mathbf{Y}}) \\ \hat{\mathbf{e}}_0 &= \hat{\mathbf{Z}} \\ \hat{\mathbf{e}}_{-1} &= \frac{1}{\sqrt{2}}(\hat{\mathbf{X}} - i\hat{\mathbf{Y}}) \end{aligned} \quad (2.15)$$

As for the second term in the square bracket in Eq. (2.1), we can do the same thing. Instead of considering the product of two scalars $(\mathbf{d}_A \cdot \hat{R})(\mathbf{d}_B \cdot \hat{R})$, we consider it as a special case of the scalar product of two vectors (thinking of a vector with two components being zero). Then according to Eq. (2.2), we have

$$(\mathbf{d}_A \cdot \hat{R})(\mathbf{d}_B \cdot \hat{R}) = 3 \left[\left[\mathbf{d}_A^{(1)} \otimes \hat{\mathbf{R}}^{(1)} \right]^{(0)} \otimes \left[\mathbf{d}_B^{(1)} \otimes \hat{\mathbf{R}}^{(1)} \right]^{(0)} \right]_0^{(0)} . \quad (2.16)$$

There is a simple understanding of the above equation: an angular momentum \mathbf{d}_A with $j_1 = 1$ couples another angular momentum \hat{R} with $j_2 = 1$ to give rise to a new angular momentum, and an angular momentum \mathbf{d}_B with $j_3 = 1$ couples another angular momentum \hat{R} with $j_4 = 1$ to give rise to another new angular momentum, and then these two new angular momentum couples with each other. It is necessary to regroup these operators such that dipole operators are separated from the position operators. The regrouping of operators corresponds to different coupling schemes (orders) of the four angular momentums. In the following, we will talk about the coupling of four angular momentums.

The coupling of four angular momenta has more than one possible coupling

scheme, and all these coupling schemes are related by unitary transformations. We might couple j_1 , j_2 , j_3 and j_4 in such a way that $j_1 + j_4 = j_{14}$, $j_2 + j_3 = j_{23}$, and $j_{14} + j_{23} = j$. The eigenfunctions in this coupling scheme is give by $|(j_1 j_4) j_{14} (j_2 j_3) j_{23} j m\rangle$. The relation between the states corresponding to different coupling schemes is

$$|(j_1 j_4) j_{14} (j_2 j_3) j_{23} j m\rangle = \sum_{j_{12}} \sum_{j_{34}} \langle (j_1 j_2) j_{12} (j_3 j_4) j_{34} j | (j_1 j_4) j_{14} (j_2 j_3) j_{23} j \rangle \\ \times |(j_1 j_4) j_{14} (j_2 j_3) j_{23} j m\rangle , \quad (2.17)$$

and the $9 - j$ symbol is defined by

$$\langle (j_1 j_2) j_{12} (j_3 j_4) j_{34} j | (j_1 j_4) j_{14} (j_2 j_3) j_{23} j \rangle \\ = \sqrt{(2j_{12}+1)(2j_{34}+1)(2j_{14}+1)(2j_{23}+1)} \left\{ \begin{array}{ccc} j_1 & j_2 & j_{12} \\ j_3 & j_4 & j_{34} \\ j_{14} & j_{23} & j \end{array} \right\} \quad (2.18)$$

The first two rows of the $9 - j$ symbol is related to the coupling scheme served as the basis set and the last row is associated with the coupling scheme of $|(j_1 j_4) j_{14} (j_2 j_3) j_{23} j m\rangle$, the eigenfunction that we want to expand.

Let's expand $\left[\left[\mathbf{d}_A^{(1)} \otimes \hat{\mathbf{R}}^{(1)} \right]^{(0)} \otimes \left[\mathbf{d}_B^{(1)} \otimes \hat{\mathbf{R}}^{(1)} \right]^{(0)} \right]_0^{(0)}$ in terms of another coupling scheme, namely \mathbf{d}_A couples \mathbf{d}_B and $\hat{\mathbf{R}}$ couples $\hat{\mathbf{R}}$. Based on Eq. (2.17) and (2.18), we have

$$(\mathbf{d}_A \cdot \hat{\mathbf{R}})(\mathbf{d}_B \cdot \hat{\mathbf{R}}) = 3 \sum_k (2k+1) \left\{ \begin{array}{ccc} 1 & 1 & k \\ 1 & 1 & k \\ 0 & 0 & 0 \end{array} \right\} \left[\left[\mathbf{d}_A^{(1)} \otimes \mathbf{d}_B^{(1)} \right]^{(k)} \otimes \left[\hat{\mathbf{R}}^{(1)} \otimes \hat{\mathbf{R}}^{(1)} \right]^{(k)} \right]_0^{(0)} . \quad (2.19)$$

Obviously, in the above $9 - j$ symbol $1 + 1 = k$ and $1 + 1 = k$ is the new coupling scheme, and $0 + 0 = 0$ is the original coupling scheme. The $9 - j$ symbols can be expressed in terms of $6 - j$ symbols (related to the coupling of 3 angular momenta).

In the special case where the final angular momentum $j_9 = 0$, we have

$$\begin{aligned} \left\{ \begin{array}{ccc} j_1 & j_2 & j_3 \\ j_4 & j_5 & j_6 \\ j_7 & j_8 & j_9 \end{array} \right\} &= (-1)^{j_2+j_3+j_4+j_7} [(2j_3+1)(2j_7+1)]^{-\frac{1}{2}} \\ &\times \left\{ \begin{array}{ccc} j_1 & j_2 & j_3 \\ j_5 & j_4 & j_7 \end{array} \right\} \delta_{j_3 j_6} \delta_{j_7 j_8}. \end{aligned} \quad (2.20)$$

Then

$$\begin{aligned} \left\{ \begin{array}{ccc} 1 & 1 & k \\ 1 & 1 & k \\ 0 & 0 & 0 \end{array} \right\} &= (-1)^{k+2} (2k+1)^{-\frac{1}{2}} \left\{ \begin{array}{ccc} 1 & 1 & k \\ 1 & 1 & 0 \end{array} \right\} \\ &= (-1)^{k+2} (2k+1)^{-\frac{1}{2}} \begin{cases} \frac{1}{3}(-1)^{-k} & 0 \leq k \leq 2 \\ 0 & \text{otherwise} \end{cases} \end{aligned} \quad (2.21)$$

Because k results from the coupling of $j_1 = 1$ and $j_2 = 1$, it is in the range of $|j_1 - j_2|, \dots, |j_1 + j_2|$, and the above equation can be simplified as

$$\left\{ \begin{array}{ccc} 1 & 1 & k \\ 1 & 1 & k \\ 0 & 0 & 0 \end{array} \right\} = \frac{(2k+1)^{-\frac{1}{2}}}{3}. \quad (2.22)$$

Substituting Eq. (2.22) into Eq. (2.19) and using Eq. (2.3), we obtain

$$\begin{aligned} (\mathbf{d}_A \cdot \hat{\mathbf{R}})(\mathbf{d}_B \cdot \hat{\mathbf{R}}) &= \sum_{k=0,1,2} \sum_q (2k+1)^{\frac{1}{2}} \langle kq, k-q | 00 \rangle \left[\mathbf{d}_A^{(1)} \otimes \mathbf{d}_B^{(1)} \right]_q^{(k)} \left[\hat{\mathbf{R}}^{(1)} \otimes \hat{\mathbf{R}}^{(1)} \right]_{-q}^{(k)} \\ &= \sum_{k=0,1,2} \sum_q (-1)^{k-q} \left[\mathbf{d}_A^{(1)} \otimes \mathbf{d}_B^{(1)} \right]_q^{(k)} \left[\hat{\mathbf{R}}^{(1)} \otimes \hat{\mathbf{R}}^{(1)} \right]_{-q}^{(k)}. \end{aligned} \quad (2.23)$$

Since the tensor product of rank 1 is related to the cross product, $\left[\hat{\mathbf{R}}^{(1)} \otimes \hat{\mathbf{R}}^{(1)} \right]_{-q}^{(k=1)}$ is associated with $\hat{\mathbf{R}} \times \hat{\mathbf{R}}$ and it is zero. Then Eq. (2.23) can be simplified further

as

$$\begin{aligned}
(\mathbf{d}_A \cdot \hat{\mathbf{R}})(\mathbf{d}_B \cdot \hat{\mathbf{R}}) &= \left[\mathbf{d}_A^{(1)} \otimes \mathbf{d}_B^{(1)} \right]_0^{(0)} \left[\hat{\mathbf{R}}^{(1)} \otimes \hat{\mathbf{R}}^{(1)} \right]_0^{(0)} \\
&\quad + \sum_{|q|=0,1,2} (-1)^q \left[\mathbf{d}_A^{(1)} \otimes \mathbf{d}_B^{(1)} \right]_q^{(2)} \left[\hat{\mathbf{R}}^{(1)} \otimes \hat{\mathbf{R}}^{(1)} \right]_{-q}^{(2)} \\
&= \left(-\frac{1}{\sqrt{3}} \mathbf{d}_A \cdot \mathbf{d}_B \right) \left(-\frac{1}{\sqrt{3}} \hat{\mathbf{R}} \cdot \hat{\mathbf{R}} \right) \\
&\quad + \sum_q (-1)^q \left[\mathbf{d}_A^{(1)} \otimes \mathbf{d}_B^{(1)} \right]_q^{(2)} \left[\hat{\mathbf{R}}^{(1)} \otimes \hat{\mathbf{R}}^{(1)} \right]_{-q}^{(2)} \\
&= \frac{\mathbf{d}_A \cdot \mathbf{d}_B}{3} + \sum_q (-1)^q \left[\mathbf{d}_A^{(1)} \otimes \mathbf{d}_B^{(1)} \right]_q^{(2)} \left[\hat{\mathbf{R}}^{(1)} \otimes \hat{\mathbf{R}}^{(1)} \right]_{-q}^{(2)}
\end{aligned} \tag{2.24}$$

Substitution of Eq. (2.24) into the expression for the dipole-dipole interaction (Eq. (2.1)) yields

$$\hat{V}_{dd}(\mathbf{R}) = \frac{-3}{R^3} \sum_q (-1)^q \left[\mathbf{d}_A^{(1)} \otimes \mathbf{d}_B^{(1)} \right]_q^{(2)} \left[\hat{\mathbf{R}}^{(1)} \otimes \hat{\mathbf{R}}^{(1)} \right]_{-q}^{(2)}. \tag{2.25}$$

Before we go on, it is helpful to get familiar with rotational matrices and spherical harmonics.

2.2 Dipole-dipole interaction

2.3 Diatomic molecule in DC field

2.4 Diatomic molecule in AC field

2.5 Introduction to exciton

We describe the state of a crystal system by specifying the occupation state of each molecules that constitute the crystal. For example, we denote the crystal wavefunction as

$$|N_{1f_1}N_{2f_2}\dots N_{nf_n}\dots\rangle ,$$

where N_{nf} represents the occupation number of state f in molecule n and it is either 0 or 1. Accordingly, the occupation number operator is defined as

$$\hat{N}_{nf}|...N_{nf}\dots\rangle = N_{nf}|...N_{nf}\dots\rangle . \quad (2.26)$$

For one molecule n , it must be in some state g , therefore

$$\sum_g \hat{N}_{ng} = 1 . \quad (2.27)$$

It is convenient to introduce two operators b_{nf}^\dagger and b_{nf} associated with molecule n and state f ,

$$\begin{aligned} b_{nf}^\dagger |...N_{nf}\dots\rangle &= (1 - N_{nf}) |...(N_{nf} + 1)\dots\rangle , \\ b_{nf} |...N_{nf}\dots\rangle &= N_{nf} |...(N_{nf} - 1)\dots\rangle , \end{aligned} \quad (2.28)$$

and express the occupation number operator as the product of these two operators,

$$\hat{N}_{nf} = b_{nf}^\dagger b_{nf} . \quad (2.29)$$

The physical meaning of the two operators is clear: b_{nf} creates a state f in molecule n and b_{nf} destroy a state f in molecule n . It follows from Eq. (2.28) that

$$\begin{aligned} b_{nf}b_{nf}^\dagger &+ b_{nf}^\dagger b_{nf} = 1, \\ b_{nf}b_{nf} &= b_{nf}^\dagger b_{nf}^\dagger = 0. \end{aligned} \quad (2.30)$$

Because an operator for a specific molecule n and state f does not operate on other molecules and other states, any two operators that correspond to different molecules n and m or different states f and f' commute all the time.

Based on the physical meaning of b_{nf}^\dagger and b_{nf} , it can be easily seen that the exciton creation and annihilation operators can be written as

$$P_{nf}^\dagger = b_{nf}^\dagger b_{n0}, \quad P_{nf} = b_{n0}^\dagger b_{nf}. \quad (2.31)$$

Substituting Eq. (2.30), we have

$$\begin{aligned} P_{nf}^\dagger P_{nf} &= b_{nf}^\dagger b_{n0} b_{n0}^\dagger b_{nf} \\ &= b_{nf}^\dagger (1 - b_{n0}^\dagger b_{n0}) b_{nf} \\ &= \hat{N}_{nf}, \end{aligned} \quad (2.32)$$

$$\begin{aligned} P_{nf} P_{nf}^\dagger &= b_{n0}^\dagger b_{nf} b_{nf}^\dagger b_{n0} \\ &= b_{n0}^\dagger (1 - b_{nf}^\dagger b_{nf}) b_{n0} \\ &= \hat{N}_{n0}. \end{aligned} \quad (2.33)$$

Subtracting Eq. (2.32) from Eq. (2.33) and making use of Eq. (2.27), we obtain

$$P_{nf} P_{nf}^\dagger - P_{nf}^\dagger P_{nf} = 1 - \hat{N}_{nf} - \sum_{g \neq 0} \hat{N}_{ng}. \quad (2.34)$$

Because P_{nf} and P_{nf}^\dagger don't operate on a different molecule m , any exciton operators corresponding to different molecules commute with each other. Then the exact

statistics is given by

$$P_{nf}P_{n'f}^\dagger - P_{n'f}^\dagger P_{nf} = \delta_{nn'} \left(1 - \hat{N}_{nf} - \sum_{g \neq 0} \hat{N}_{ng} \right) \quad (2.35)$$

and

$$P_{nf}P_{nf'}^\dagger - P_{nf'}^\dagger P_{nf} = \delta_{ff'} . \quad (2.36)$$

Unfortunately, it is cumbersome to take into account of the exact statistics of excitons in most cases. So it is often desirable to approximate excitons as Boles when only a small number of molecules in the crystal are excited. In other words, if the following inequality

$$\langle N_{nf} \rangle \ll 1 \quad (2.37)$$

holds, the exciton creation and annihilation operators satisfy the commutation rules for Bose operators

$$P_{n'f'}P_{nf}^\dagger - P_{nf}^\dagger P_{n'f'} = \delta_{nn'}\delta_{ff'} . \quad (2.38)$$

In the following derivation, we are assuming the exciton operators are Bose operators and satisfy Eq. (2.38).

The way to use operator P_{nf} and P_{nf}^\dagger to describe excitons is called site representation. Due to the periodicity of crystal, there is another way to represent excitons by making use of the Fourier transforms of P_{nf} and P_{nf}^\dagger :

$$\begin{aligned} P_{nf} &= \frac{1}{\sqrt{N}} \sum_k P_f(k) e^{ikn} \\ P_{nf}^\dagger &= \frac{1}{\sqrt{N}} \sum_k P_f^\dagger(k) e^{-ikn} , \end{aligned} \quad (2.39)$$

and this is called wavevector representation. Since the unitary transformation does not change the commutation rule of operators, we expect that the following equation

$$P_{f',k'}P_{f,k}^\dagger - P_{f,k}^\dagger P_{f',k'} = \delta_{kk'}\delta_{ff'} . \quad (2.40)$$

also hold. This can be verified by substituting Eq. (2.39) into Eq. (2.38).

Chapter 3

Tunable exciton interactions in optical lattices with polar molecules

Rotational excitation of polar molecules trapped in an optical lattice gives rise to rotational excitons. Here we show that non-linear interactions of such excitons can be controlled by an electric field. The exciton–exciton interactions can be tuned to induce exciton pairing, leading to the formation of biexcitons. Tunable non-linear interactions between excitons can be used for many applications ranging from the controlled preparation of entangled quasiparticles to the study of polaron interactions and the effects of non-linear interactions on quantum energy transport in molecular aggregates.

3.1 Introduction

The absorption of photons by a solid-state crystal gives rise to quasiparticles called excitons. There are two limiting models of excitons: Wannier-Mott excitons and Frenkel excitons. Wannier-Mott excitons occur in crystals with band structure leading to collective excitations with an effective radius much greater than the lattice constant, while Frenkel excitons are typical for molecular crystals, where collective excitations are superpositions of elementary excitations localized on different

lattice sites. These properties lead to important differences in non-linear exciton interactions for the two models. The interactions between the Wannier-Mott excitons are determined by the Coulomb interaction and the phase space filling [1, 2], while the interactions of Frenkel excitons are determined by shorter range dynamical couplings [3]. Multiple experiments demonstrated that Wannier-Mott excitons can form two-exciton bound states called biexcitons [4–10]. By contrast, despite many theoretical studies [11–14], Frenkel biexcitons have eluded the experimental observation, with one notable exception [15, 16]. In the present work, we show that rotational excitation of ultracold molecules trapped on an optical lattice gives rise to Frenkel excitons with controllable non-linear interactions. We demonstrate that the exciton–exciton interactions can be tuned to induce the formation of Frenkel biexciton and that the biexciton binding energy can be controlled by an external electric field.

Several experiments have recently demonstrated that ultracold molecules can be trapped in a periodic potential of an optical lattice [17–19]. Such systems can be used for the study of quantum energy transfer [20, 21], non-linear photon–photon interactions [22], novel quantum memory devices [23, 24] and, most notably, for quantum simulation of lattice models [25–34]. Although describing different phenomena, the Hamiltonians presented in these references, and in the present work, can be cast in the same form. For example, the exciton Hamiltonian discussed here can be mapped onto the t - V model, which is the special case of the Heisenberg-like models studied in the context of ultracold molecules in Refs. [26–28, 33, 34]. The key difference of the present work from those in Refs. [26–28, 33, 34] is that we explore phenomena associated with the excitation spectrum of the many-body system in the limit of a small number of excitations. Because we consider a simpler Hamiltonian, our scheme is conceptually simpler, requiring fewer molecular states and external field parameters. We use the rotational states of molecules as a probe of the collective interactions, i.e. the experiments proposed here can be carried out by measuring site-selective populations of the rotational states. This can be achieved by applying a gradient of an electric field and detecting resonant transitions from Stark-shifted levels, as described in Ref. [35].

3.2 Exciton-exciton interactions in an optical lattice

We consider an ensemble of polar diatomic molecules in the ${}^1\Sigma$ electronic state trapped on an optical lattice in the ro-vibrational ground state. The rotational states of the molecules $|NM_N\rangle$ are described by the rotational angular momentum \hat{N} and its projection on the quantization axis M_N . We assume that the molecules are in the Mott-insulator phase [17–19] and that each lattice site contains only one molecule. We consider the rotational excitation $|N=0, M_N=0\rangle \rightarrow |N=1, M_N=0\rangle$ of molecules in the lattice [36]. For simplicity, we denote the ground state of the molecule in site n by $|g_n\rangle$ and the excited state by $|e_n\rangle$. Because the molecules are coupled by the dipole-dipole interaction, the rotational excitation gives rise to a rotational Frenkel exciton [20], which is an eigenstate of the Hamiltonian:

$$\hat{H}_{\text{exc}} = E_0 \sum_{n=1}^{N_{\text{mol}}} \hat{P}_n^\dagger \hat{P}_n + \sum_{n,m \neq n}^{N_{\text{mol}}} J(n-m) \hat{P}_n^\dagger \hat{P}_m, \quad (3.1)$$

where $J(n-m) = \langle e_n, g_m | \hat{V}_{dd}(n-m) | g_n, e_m \rangle$ with $\hat{V}_{dd}(n-m)$ representing dipole-dipole interaction between molecules in sites n and m , E_0 is the energy difference between the states $|g\rangle$ and $|e\rangle$, and the operators \hat{P}_n^\dagger and \hat{P}_n are defined by the relations $\hat{P}_n^\dagger |g_m\rangle = \delta_{nm} |e_n\rangle$ and $\hat{P}_n |e_m\rangle = \delta_{nm} |g_n\rangle$. The \hat{P}_n and \hat{P}_m operators satisfy the bosonic commutation

$$\hat{P}_n \hat{P}_m^\dagger - \hat{P}_m^\dagger \hat{P}_n = \delta_{n,m} = 0, \quad (3.2)$$

if $n \neq m$, and the fermionic commutation

$$\hat{P}_n \hat{P}_m^\dagger + \hat{P}_m^\dagger \hat{P}_n = 1, \quad (3.3)$$

if $n = m$ [3]. It is useful to combine the two commutation relations as

$$\hat{P}_n \hat{P}_m^\dagger + \hat{P}_m \hat{P}_n^\dagger = \delta_{m,n} + (1 - \delta_{m,n}) 2 \hat{P}_n^\dagger \hat{P}_m, \quad (3.4)$$

which gives rise to

$$\hat{P}_m \hat{P}_n^\dagger = \delta_{m,n} + (1 - 2\delta_{m,n}) \hat{P}_n^\dagger \hat{P}_m. \quad (3.5)$$

We will make frequent usage of equation (3.5) when evaluating the matrix elements of Hamiltonians.

Multiple excitations lead to dynamical exciton–exciton interactions described by [3]:

$$\hat{H}_{\text{dyn}} = \frac{1}{2} \sum_{n,m \neq n}^{N_{\text{mol}}} D(n-m) \hat{P}_n^\dagger \hat{P}_m^\dagger \hat{P}_n \hat{P}_m \quad (3.6)$$

where

$$\begin{aligned} D(n-m) &= \langle e_n, e_m | \hat{V}_{dd}(n-m) | e_n, e_m \rangle + \langle g_n, g_m | \hat{V}_{dd}(n-m) | g_n, g_m \rangle \\ &\quad - 2 \langle e_n, g_m | \hat{V}_{dd}(n-m) | e_n, g_m \rangle, \end{aligned} \quad (3.7)$$

and the factor 1/2 is there to cancel the effect of double counting of the pairs (n, m) . In the above summations, we have restricted that m cannot equal to n because two excitations cannot sit at the same lattice site (or in other word a molecule can't be excited twice to the same excited state). The dipole - dipole interaction operator $\hat{V}_{dd}(n-m)$ can only couple states of different parity [37]. If $|g\rangle$ and $|e\rangle$ are states of well-defined parity, such as the rotational states $|N, M_N\rangle$, the matrix elements $D(n-m)$ must be zero.

The inversion symmetry (parity) of molecules on an optical lattice can be broken by applying an external dc electric field. In an electric field, $|g_n\rangle$ and $|e_n\rangle$ are eigenstates of the Hamiltonian $\hat{H}_n^{\text{mol}} = B_e \hat{N}_n^2 - \mathbf{d}_n \cdot \mathcal{E}_f$, where \mathbf{d}_n is the dipole moment of molecule in site n and \mathcal{E}_f is the electric field vector. They can be expressed as $|g\rangle = \sum_N a_N |N, M_N = 0\rangle$ and $|e\rangle = \sum_N b_N |N, M_N = 0\rangle$, where a_N and b_N are determined by the electric field strength. Note that we choose $M_N = 0$ states because they adiabatically connects to nondegenerate rotational bare states as the external field goes to zero, leading to a single isolated exciton band. For other $M_N \neq 0$ states, for example $M_N = 1$ states, there will be two crossing exciton bands corresponding to the excitation from the dressed state $|0, 1\rangle$ to $|1, 1\rangle$. See figure 2 in Ref. [20].

The Hamiltonian (3.1) can be diagonalized by the Fourier transforms: $\hat{P}^\dagger(k) = \frac{1}{\sqrt{N_{\text{mol}}}} \sum_n e^{ikn} \hat{P}_n^\dagger$ and $\hat{P}(k) = \frac{1}{\sqrt{N_{\text{mol}}}} \sum_n e^{-ikn} \hat{P}_n$, where k is the wave vector of the exciton. This transformation leads to $\hat{H}_{\text{exc}} = \sum_k E(k) \hat{P}^\dagger(k) \hat{P}(k)$, where $E(k) = E_0 + J(k)$ with

$J(k) = \sum_n J(n)e^{-ikn}$, and $\hat{P}^\dagger(k)$ and $\hat{P}(k)$ create and annihilate Frenkel excitons with energies $E(k)$. The interaction (3.6) in the momentum representation is:

$$\hat{H}_{\text{dyn}} = \frac{1}{N_{\text{mol}}} \sum_{k_1, k_2, q} \tilde{D}(q) \hat{P}^\dagger(k_1 + q) \hat{P}^\dagger(k_2 - q) \hat{P}(k_1) \hat{P}(k_2), \quad (3.8)$$

where $\tilde{D}(q) = \sum_n D(n)e^{-iqn}$.

3.3 Biexcitons

The exciton–exciton interactions generally have little effect on the energy spectrum of two-particle continuum states $E(k_1) + E(k_2)$. However, under certain conditions discussed below, non-linear interactions may result in the formation of a bound two-exciton complex, biexciton. The biexciton state is split from the two-particle continuum. The splitting is the biexciton binding energy.

3.3.1 Method to calculate biexciton energies

In the following, we discuss how to calculate the energy of a biexciton. We start from the Hamiltonian

$$\begin{aligned} \hat{H} &= \hat{H}_{\text{exc}} + \hat{H}_{\text{dyn}} \\ &= E_0 \underbrace{\sum_{n=1}^{N_{\text{mol}}} \hat{P}_n^\dagger \hat{P}_n}_{(1)} + \underbrace{\sum_{n,m} J(n-m) \hat{P}_n^\dagger \hat{P}_m}_{(2)} + \underbrace{\frac{1}{2} \sum_{n,m} D(n-m) \hat{P}_n^\dagger \hat{P}_m^\dagger \hat{P}_n \hat{P}_m}_{(3)}, \end{aligned} \quad (3.9)$$

where the constraint that $m \neq n$ is removed by assuming $J(0) = 0$ and $D(0) = 0$. The task is to find the eigenvalues and eigenfunctions of the above Hamiltonian in the two-excitation basis sets:

$$|\psi\rangle = \sum_{n,m} C_{n,m} \hat{P}_n^\dagger \hat{P}_m^\dagger |0\rangle. \quad (3.10)$$

Normally, we would exclude the terms in which $n = m$ from the above expansion. But in the current case, we assume $C_{n,n} = 0$ and keep those terms so that the Fourier

transformation for the coefficients $C_{n,m}$ to a quasimomentum space

$$C_{n,m} = \frac{1}{N_{\text{mol}}} \sum_{k_1, k_2} C_{k_1, k_2} e^{i(k_1 n + k_2 m)} \quad (3.11)$$

is well-defined. More importantly, by doing so, we can derive an equation that will correspond to the case of two noninteracting bosons. This will become evident later. Based on the physical meaning of the coefficients $C_{n,m}$, we conclude that $C_{n,m}$ satisfy the symmetry relation

$$C_{n,m} = C_{m,n} \quad (3.12)$$

and are to be normalized by

$$\sum_{n,m} |C_{n,m}|^2 = 1 \quad (3.13)$$

Assuming the wavefunction ψ satisfies the Schrödinger equation

$$\hat{H}|\psi\rangle = E|\psi\rangle, \quad (3.14)$$

we can obtain the equations for the coefficients $C_{n,m}$. Note since the terms $C_{n,n}$ are added into equation (3.11) for artificial purposes, their values are not determined by the Schrödinger equation. To derive the equations for $C_{n,m}$, we let the Hamiltonian \hat{H} operate on the wavefunction term by term. The first term in equation (3.14) gives rise to:

$$\begin{aligned} \textcircled{1} |\psi\rangle &= E_0 \sum_{n',n,m} C_{n,m} \hat{P}_{n'}^\dagger \hat{P}_{n'} \hat{P}_n^\dagger \hat{P}_m^\dagger |0\rangle \\ &= E_0 \sum_{n',n,m} C_{n,m} \hat{P}_{n'}^\dagger [\delta_{n',n} + (1 - 2\delta_{n',n}) \hat{P}_n^\dagger \hat{P}_{n'}] \hat{P}_m^\dagger |0\rangle \\ &= E_0 \sum_{n',n,m} C_{n,m} [\delta_{n',n} \hat{P}_{n'}^\dagger \hat{P}_m^\dagger + (1 - 2\delta_{n',n}) \hat{P}_{n'}^\dagger \hat{P}_n^\dagger \hat{P}_{n'}^\dagger \hat{P}_m^\dagger] |0\rangle \\ &= E_0 \sum_{n',n,m} C_{n,m} [\delta_{n',n} \hat{P}_{n'}^\dagger \hat{P}_m^\dagger + (1 - 2\delta_{n',n}) \hat{P}_{n'}^\dagger \hat{P}_n^\dagger \delta_{n',m}] |0\rangle \\ &= E_0 \sum_{n,m} C_{n,m} [\hat{P}_n^\dagger \hat{P}_m^\dagger + (1 - 2\delta_{m,n}) \hat{P}_m^\dagger \hat{P}_n^\dagger] |0\rangle, \end{aligned} \quad (3.15)$$

where $|0\rangle$ is the vacuum state that every particle is in the ground state. In the above derivation, equation (3.5) and $\hat{P}_n|0\rangle = 0$ has been used. Similarly, the second term and the third term give rise to

$$\textcircled{2} |\psi\rangle = \sum_{n,m} \left[\sum_{n'} J(n' - n) C_{n',m} \hat{P}_n^\dagger \hat{P}_m^\dagger + \sum_{n'} J(n' - m) C_{n,n'} (1 - 2\delta_{m,n}) \hat{P}_m^\dagger \hat{P}_n^\dagger \right] \quad (3.16)$$

and

$$\textcircled{3} |\psi\rangle = \frac{1}{2} \sum_{n,m} [D(n - m) C_{n,m} \hat{P}_m^\dagger \hat{P}_n^\dagger + D(n - m) C_{n,m} (1 - 2\delta_{m,n}) \hat{P}_n^\dagger \hat{P}_m^\dagger] \quad (3.17)$$

respectively. The right hand side of equation (3.14) is given by

$$E|\psi\rangle = E \sum_{n,m} C_{n,m} \hat{P}_n^\dagger \hat{P}_m^\dagger |0\rangle . \quad (3.18)$$

Given the fact that $\hat{P}_n^\dagger \hat{P}_m^\dagger$ and $\hat{P}_m^\dagger \hat{P}_n^\dagger$ are equivalent, a comparsion of both sides of the Schrödinger equation yields the following equation for $C_{n,m}$ when $n \neq m$:

$$(E - 2E_0)C_{n,m} - \sum_{n'} J(n' - n) C_{n',m} - \sum_{n'} J(n' - m) C_{n,n'} = D(n - m) C_{n,m} \quad (3.19)$$

When $n = m$, the above equation becomes

$$\begin{aligned} & (E - 2E_0)C_{n,m} - \sum_{n'} J(n' - n) C_{n',m} - \sum_{n'} J(n' - m) C_{n,n'} \\ &= (E - 2E_0)C_{n,n} - 2 \sum_{n'} J(n - n') C_{n,n'} . \end{aligned} \quad (3.20)$$

Note the two sides of equation (3.20) are equivalent, so we cannot obtain the value of $C_{n,n}$ from it. This is consistent with the previous assumption that $C_{n,n} = 0$ because equation (3.20) allows us to take an arbitrary value for $C_{n,n}$. By Combining

equation (3.19) for $n \neq m$ and equation (3.20) for $n = m$, we obtain a new equation

$$\underbrace{(E - 2E_0)C_{n,m}}_{\textcircled{4}} - \underbrace{\sum_{n'} J(n' - n)C_{n',m}}_{\textcircled{5}} - \underbrace{\sum_{n'} J(n' - m)C_{n,n'}}_{\textcircled{6}} \\ = \underbrace{\delta_{n,m}(E - 2E_0)C_{n,m}}_{\textcircled{7}} - \underbrace{2\delta_{n,m} \sum_{n'} J(n - n')C_{n,n'}}_{\textcircled{8}} + \underbrace{D(n - m)C_{n,m}}_{\textcircled{9}}, \quad (3.21)$$

which is valid for all coefficients $C_{n,m}$. The left hand side of equation (3.21) now corresponds to the case of two noninteracting bosons since the summations include terms like $C_{m,m}$ and $C_{n,n}$. On the right hand side, the first two terms describe the kinematic interaction of excitons due to equation (3.4) and equation (3.5), and the last term represents the dynamical interaction of excitons.

The dimension of the system of coupled equations (3.21) is about $N_{\text{mol}} \times N_{\text{mol}}$, which is large even for a lattice with moderate size. To reduce the number of equations that we need to solve, we make use of the translational symmetry of the lattices and convert equation (3.21) into a quasimomentum representation. Since the conversion involves some nontrivial derivations, we give the details for (8) in

equation (3.21) which are characteristic for the whole calculations.

$$\begin{aligned}
(8) &= \delta_{n,m} \left[\sum_{n'} J(n' - n) C_{n',m} + \sum_{n'} J(n' - m) C_{n,n'} \right] \\
&= \frac{\delta_{n,m}}{N_{\text{mol}}} \left[\sum_{n'} J(n' - n) \sum_{k_1, k_2} C_{k_1, k_2} e^{i(k_1 n' + k_2 m)} + \sum_{n'} J(n' - m) \sum_{k_1, k_2} C_{k_1, k_2} e^{i(k_1 n + k_2 n')} \right] \\
&= \frac{\delta_{n,m}}{N_{\text{mol}}} \left[\sum_{k_1, k_2} C_{k_1, k_2} e^{i(k_2 m + k_1 n)} \sum_{n'} J(n' - n) e^{ik_1(n' - n)} \right. \\
&\quad \left. + \sum_{k_1, k_2} C_{k_1, k_2} e^{i(k_1 n + k_2 m)} \sum_{n'} J(n' - m) e^{ik_2(n' - m)} \right] \\
&= \frac{\delta_{n,m}}{N_{\text{mol}}} \left[\sum_{k_1, k_2} C_{k_1, k_2} e^{i(k_2 m + k_1 n)} \sum_{n' - n} J(n' - n) e^{ik_1(n' - n)} \right. \\
&\quad \left. + \sum_{k_1, k_2} C_{k_1, k_2} e^{i(k_1 n + k_2 m)} \sum_{n' - m} J(n' - m) e^{ik_2(n' - m)} \right] \\
&= \frac{\delta_{n,m}}{N_{\text{mol}}} \sum_{k_1, k_2} e^{i(k_1 n + k_2 m)} C_{k_1, k_2} [\tilde{J}(k_1) + \tilde{J}(k_2)] \\
&= \frac{1}{N_{\text{mol}}^2} \sum_{k_3} e^{ik_3(n-m)} \sum_{k_1, k_2} e^{i(k_1 n + k_2 m)} C_{k_1, k_2} [\tilde{J}(k_1) + \tilde{J}(k_2)] \\
&= \frac{1}{N_{\text{mol}}^2} \sum_{k_1, k_2, k_3} e^{i(k_1 + k_3)n} e^{i(k_2 - k_3)m} C_{k_1, k_2} [\tilde{J}(k_1) + \tilde{J}(k_2)] \\
&= \frac{1}{N_{\text{mol}}^2} \sum_{k'_1 = k_1 + k_3, k'_2 = k_2 - k_3} e^{i(k'_1 n + k'_2 m)} C_{k'_1 - k_3, k'_2 + k_3} \sum_{k_3} [\tilde{J}(k'_1 - k_3) + \tilde{J}(k'_2 + k_3)] \\
&= \frac{1}{N_{\text{mol}}^2} \sum_{k_1, k_2} e^{i(k_1 n + k_2 m)} C_{k_1 - k_3, k_2 + k_3} \sum_{k_3} [\tilde{J}(k_1 - k_3) + \tilde{J}(k_2 + k_3)] . \tag{3.22}
\end{aligned}$$

In the above derivation, we have made use of equation (3.11), the definition of $\tilde{J}(k)$:

$$\tilde{J}(k) \equiv \sum_n e^{ikn} J(n) \tag{3.23}$$

and the normalization relation of plane wave:

$$\frac{1}{N} \sum_k e^{ik(n-m)} = \delta_{n,m} . \tag{3.24}$$

In the last step of equation (3.22), since k'_1 and k'_2 have the same range as k_1 and k_2 , we have dropped their prime superscripts. Similar derivations like the above yield

$$\textcircled{4} = \frac{(E - 2E_0)}{N_{\text{mol}}} \sum_{k_1, k_2} C_{k_1, k_2} e^{i(k_1 n + k_2 m)}, \quad (3.25)$$

$$\textcircled{5} = \frac{1}{N_{\text{mol}}} \sum_{k_1, k_2} C_{k_1, k_2} e^{i(k_1 n + k_2 m)} \tilde{J}(k_1), \quad (3.26)$$

$$\textcircled{6} = \frac{1}{N_{\text{mol}}} \sum_{k_1, k_2} C_{k_1, k_2} e^{i(k_1 n + k_2 m)} \tilde{J}(k_2), \quad (3.27)$$

$$\textcircled{7} = \frac{(E - 2E_0)}{N_{\text{mol}}^2} \sum_{k_1, k_2} e^{i(k_1 n + k_2 m)} \sum_{k_3} C_{k_1 - k_3, k_2 + k_3}, \quad (3.28)$$

and

$$\textcircled{9} = \frac{1}{N_{\text{mol}}^2} \sum_{k_1, k_2} e^{i(k_1 n + k_2 m)} \sum_{k_3} \tilde{D}(k_3) C_{k_1 - k_3, k_2 + k_3}. \quad (3.29)$$

Then equation (3.21) reduces to an equation for C_{k_1, k_2} :

$$\begin{aligned} [E - \varepsilon(k_1) - \varepsilon(k_2)] C_{k_1, k_2} &= \sum_{k_3} \frac{E - \varepsilon(k_1 - k_3) - \varepsilon(k_2 + k_3)}{N_{\text{mol}}} C_{k_1 - k_3, k_2 + k_3} \\ &+ \frac{1}{N_{\text{mol}}} \sum_{k_3} \tilde{D}(k_3) C_{k_1 - k_3, k_2 + k_3}, \end{aligned} \quad (3.30)$$

where $\varepsilon(k)$ is the energy of an exciton and is given by

$$\varepsilon(k) = E_0 + \sum_n J(n) e^{ikn}. \quad (3.31)$$

There is an additional constraint for C_{k_1, k_2} which is due to the assumption that

$C_{n,n} = 0$:

$$\begin{aligned}
\sum_{k_1+k_2=K} C_{k_1,k_2} &= \sum_{k_1,k_2} \frac{1}{N} \sum_{n,m} C_{n,m} e^{-i(k_1 n + k_2 m)} \\
&= \sum_{k_1} \frac{1}{N} \sum_{n,m} C_{n,m} e^{-i[k_1 n + (K - k_1)m]} \\
&= \sum_{n,m} C_{n,m} e^{iKm} \frac{1}{N} \sum_{k_1} e^{-ik_1(n-m)} \\
&= \sum_{n,m} C_{n,m} e^{iKm} \delta_{n,m} \\
&= \sum_n C_{n,n} = 0 . \tag{3.32}
\end{aligned}$$

Because of equation (3.32), we can eliminate E terms in first summation on the right hand side of equation (3.30) and obtain

$$[E - \varepsilon(k_1) - \varepsilon(k_2)] C_{k_1,k_2} = \frac{1}{N_{\text{mol}}} \sum_{k_3} [\tilde{D}(k_3) - \varepsilon(k_1 - k_3) - \varepsilon(k_2 - k_3)] C_{k_1-k_3, k_2+k_3} . \tag{3.33}$$

Note in the above equation, the range of the wavevectors k_1 , k_2 and k_3 is $[-\pi, \pi]$. Then the range of $k_1 - k_3$ and $k_2 + k_3$ is $(-\pi, \pi)$ which is outside the first Brillouin zone. However, due to the symmetry property of the lattice, we can always bring $k_1 - k_3$ or $k_2 + k_3$ back to the first Brillouin zone by adding or subtracting 2π . Thus, we define two new wavevectors

$$k'_1 = k_1 - k_3 \pm 2\pi , \tag{3.34}$$

and

$$k'_2 = k_2 - k_3 \pm 2\pi , \tag{3.35}$$

in which $+$ or $-$ is used to make sure the values of k'_1 and k'_2 are within the first Brillouin zone. Then equation (3.33) becomes

$$[E - \varepsilon(k_1) - \varepsilon(k_2)] C_{k_1,k_2} = \frac{1}{N_{\text{mol}}} \sum_{k'_1+k'_2=k_1+k_2} [\tilde{D}(k_1 - k'_1) - \varepsilon(k'_1) - \varepsilon(k'_2)] C_{k'_1, k'_2} . \tag{3.36}$$

To avoid double counting of exciton pairs (k_1, k_2) , we can restrict the summation to

$k_1 \geq k_2$ and $k'_1 \geq k'_2$, reducing the dimension of equation (3.36) by half. This leads to

$$\begin{aligned} [E - \varepsilon(k_1) - \varepsilon(k_2)] C_{k_1, k_2} &= \frac{1}{N_{\text{mol}}} \sum_{\substack{k'_1 \geq k'_2 \\ k'_1 + k'_2 = k_1 + k_2}} \left\{ \tilde{D}(k_1 - k'_1) + (1 - \delta_{k'_1, k'_2}) \tilde{D}(k_1 - k'_2) \right. \\ &\quad \left. - (2 - \delta_{k'_1, k'_2}) [\varepsilon(k'_1) + \varepsilon(k'_2)] \right\} C_{k'_1, k'_2}. \end{aligned} \quad (3.37)$$

As can be seen from the above equation, each coefficient C_{k_1, k_2} is only coupled to other coefficients $C_{k'_1, k'_2}$ when $k_1 + k_2 = k'_1 + k'_2$. Therefore we can separate equation (3.37) into different sets and solve them independently. This will reduce the number of equation by a factor of N_{mol} , which is the reason that we want to convert equation (3.21) from the site representation to the quasimomentum representation. For each set of equations, the summation of wavevectors $k_1 + k_2 = K$ is fixed for all pairs, so equation (3.37) can be written in the form of eigenvalue equation

$$\mathbf{A}(K)\mathbf{C} = E(K)\mathbf{C}(K) \quad (3.38)$$

where the elements of the matrix $\mathbf{A}(K)$ are given by

$$\begin{aligned} \mathbf{A}_{(k_1, k_2), (k'_1, k'_2)} &= \frac{1}{N_{\text{mol}}} \left\{ \tilde{D}(k_1 - k'_1) + (1 - \delta_{k'_1, k'_2}) \tilde{D}(k_1 - k'_2) \right. \\ &\quad \left. - (2 - \delta_{k'_1, k'_2}) [\varepsilon(k'_1) + \varepsilon(k'_2)] \right\} \\ &\quad + \delta_{k_1, k'_1} \delta_{k_2, k'_2} [\varepsilon(k_1) + \varepsilon(k_2)], \end{aligned} \quad (3.39)$$

and \mathbf{C} is a vector composed of all the relevant coefficients C_{k_1, k_2} :

$$\mathbf{C} = \begin{pmatrix} \vdots \\ C_{k_1, k_2} \\ \vdots \\ C_{k'_1, k'_2} \\ \vdots \end{pmatrix} \quad (3.40)$$

By solving equation (3.38) under the constraint presented in equation (3.32), we

can obtain all the eigenvalues and eigenvectors of the two-exciton system. Under some conditions, a set of eigen energies is split from the energy continuum of two free excitons and they correspond to the biexciton states.

3.3.2 Analytical derivation of biexciton wavefunction

To gain a deeper understanding of the biexciton state, we aim to derive the biexciton wavefunction in site representation using the nearest neighbor approximation. In this section, I will sketch the entire derivation and give some details of the difficult part.

To begin, let's examine the coefficients $C_{n,m}$ in the most general two-exciton wavefunction equation (3.10). These $C_{n,m}$'s are related to C_{k_1,k_2} by equation (3.11):

$$C_{n,m} = \frac{1}{N_{\text{mol}}} \sum_{k_1,k_2} C_{k_1,k_2} e^{i(k_1 n + k_2 m)} .$$

From the analysis in Section 3.3.1, we know the sum of wavevectors of two excitons is a good quantum number for a biexciton state. Thus, it makes sense to define two new wavevectors in terms of k_1 and k_2 :

$$K = k_1 + k_2 , \quad (3.41)$$

$$k = \frac{k_1 - k_2}{2} . \quad (3.42)$$

Substituting the above two equations into equation (3.11), and using the Fourier transform

$$C_k^K = \frac{1}{\sqrt{N_{\text{mol}}}} \sum_l C^K(l) e^{-ikl} \quad (3.43)$$

and

$$C^K(l) = \frac{1}{\sqrt{N_{\text{mol}}}} \sum_k C_k^K e^{ikl} , \quad (3.44)$$

we arrive at

$$\begin{aligned}
C_{n,m} &= \frac{1}{N_{\text{mol}}} \sum_{k_1,k_2} C_{k_1,k_2} e^{i(K/2+k)n} e^{i(K/2-k)m} \\
&= \frac{1}{N_{\text{mol}}} \sum_K C^K e^{i(K/2+k)n} e^{i(K/2-k)m} \\
&= \frac{1}{\sqrt{N_{\text{mol}}}} \sum_K C^K (n-m) e^{iK(n+m)/2}.
\end{aligned} \tag{3.45}$$

Then the two-exciton wavefunction (equation (3.10)) can be written as

$$|\psi\rangle = \frac{1}{\sqrt{N_{\text{mol}}}} \sum_{n,m} \sum_K C^K (n-m) e^{iK(n+m)/2} \hat{P}_n^\dagger \hat{P}_m^\dagger |0\rangle. \tag{3.46}$$

The above equation inspires us to introduce a wavefunction that corresponds to a particular K :

$$|\psi_b^K\rangle = \frac{1}{\sqrt{N_{\text{mol}}}} \sum_{n,m} C^K (n-m) e^{iK(n+m)/2} \hat{P}_n^\dagger \hat{P}_m^\dagger |0\rangle, \tag{3.47}$$

and we are expecting it to be the wavefunction for a biexciton state. To verify our guess, we check the orthonormality of the wavefunction. The calculation of the overlap between two K -wavefunctions gives rise to

$$\langle \psi_b^Q | \psi_b^K \rangle = 2\delta_{Q,K} \sum_l |C^K(l)|^2. \tag{3.48}$$

This indicates that the wavefunctions for different K 's are orthogonal and the normalization of the wavefunction can be satisfied as long as

$$2 \sum_l |C^K(l)|^2 = 1. \tag{3.49}$$

Now the problem of finding the biexciton wavefunction becomes the problem of finding the values of $C^K(l)$ that satisfy equation (3.49). As usual, wavefunctions can be obtained by solving the Schrödinger equation, so we work with equation (3.36) which is equivalent to the Schrödinger equation for the biexciton states. The main idea is to substitute equation (3.43) into equation (3.36) and get rid of the

individual wavevector k_1 , k_2 , k'_1 and k'_2 . In this way, we will finally obtain an equation for $C^K(l)$ that depends on the summation of the wavevectors $K = (k_1 + k_2)/2$ rather than the individual wavevectors. However before doing that, we need to introduce the Green's function

$$G_{k_1, k_2}^K = \frac{1}{E - \epsilon(k_1) - \epsilon(k_2)} \quad (3.50)$$

and its fourier transform

$$\begin{aligned} G^K(n) &= \frac{1}{N_{\text{mol}}} \sum_q \frac{e^{iqn}}{E - \epsilon(K/2 + q) - \epsilon(K/2 - q)} \\ &= \frac{1}{N_{\text{mol}}} \sum_{k_1+k_2=2K} \frac{e^{i(k_1-k_2)n/2}}{E - \epsilon(k_1) - \epsilon(k_2)}. \end{aligned} \quad (3.51)$$

In the nearest neighbor approximation where only the interaction between the nearest sites is considered, the energy $\epsilon(k_1)$ of an exciton with wavevector k_1 is given by

$$\epsilon(k_1) = E_0 + 2J \cos(k_1), \quad (3.52)$$

and equation (3.51) reduces to

$$\begin{aligned} G^K(n) &= \frac{1}{N_{\text{mol}}} \sum_q \frac{e^{iqn}}{(E - 2E_0) - 2J \cos(K/2 + q) - 2J \cos(K/2 - q)} \\ &= \frac{1}{N_{\text{mol}}} \sum_q \frac{e^{iqn}}{(E - 2E_0) - 2J_K \cos(q)}, \end{aligned} \quad (3.53)$$

where J_K can be understood as the half bandwidth of the two free excitons with wavevector $K/2 + q$ and $K/2 - q$, and is given by

$$J_K = 2J \cos(K/2). \quad (3.54)$$

When the number of sites N_{mol} becomes very large, equation (3.53) can be approximated by an integral

$$G^K(n) = \frac{1}{2\pi} \int_{-\pi}^{\pi} dq \frac{e^{iqn}}{(E - 2E_0) - 2J_K \cos(q)}, \quad (3.55)$$

which can be transformed into another integral over the complex variable $w = e^{iq}$ along the unit circle

$$G^K(n) = \frac{1}{2\pi i |J_K|} \oint dw \frac{w^{|n|}}{w^2 + 2xw + 1}, \quad (3.56)$$

where $x = E/2J_K$. Then equation (3.55) can be calculated from the Residue theorem. In the case of a biexciton state, its energy E_b^K is outside the energy continuum of two free excitons $\epsilon(K+q) + \epsilon(K-q)$. There are two scenarios: first, when $E - 2E_0 > 2J_K > 0$, $G^K(n)$ is given by

$$G^K(n) = \frac{1}{\sqrt{(E - 2E_0)^2 - (2J_K)^2}} \left[-\frac{E - 2E_0}{2J_K} + \sqrt{\left(\frac{E - 2E_0}{2J_K}\right)^2 - 1} \right]^{|n|}; \quad (3.57)$$

second, when $E - 2E_0 < 2J_K < 0$, $G^K(n)$ is given by

$$G^K(n) = \frac{1}{\sqrt{(E - 2E_0)^2 - (2J_K)^2}} \left[-\frac{E - 2E_0}{2J_K} - \sqrt{\left(\frac{E - 2E_0}{2J_K}\right)^2 - 1} \right]^{|n|}. \quad (3.58)$$

For the derivations of the above two equations, please refer to page 88 of Economou's book on Green's function [38]. Since the analysis for the two scenarios are very similar, we will only concern with the first one in the following discussions.

The reason why we want to calculate $G^K(n)$ before working with equation (3.36) is that equation (3.36) contains G_{k_1, k_2}^K and G_{k_1, k_2}^K is the Fourier transform of $G^K(n)$,

$$G_{k_1, k_2}^K = \sum_m G^K(m) e^{-i(k_1 - k_2)m/2}. \quad (3.59)$$

To utilize the known analytical expression of $G^K(n)$, we divide both sides of equa-

tion (3.36) by G_{k_1, k_2}^K to get

$$\begin{aligned}
\underbrace{C_{k_1, k_2}}_{(10)} &= \underbrace{\frac{1}{N_{\text{mol}}} G_{k_1, k_2}^K \sum_{k'_1 + k'_2 = k_1 + k_2} D(n) e^{i(k_1 - k'_1)n} C_{k'_1, k'_2}}_{(11)} \\
&\quad - \underbrace{\frac{1}{N_{\text{mol}}} G_{k_1, k_2}^K \sum_{k'_1 + k'_2 = k_1 + k_2} \varepsilon(k'_1) C_{k'_1, k'_2}}_{(12)} \\
&\quad - \underbrace{\frac{1}{N_{\text{mol}}} G_{k_1, k_2}^K \sum_{k'_1 + k'_2 = k_1 + k_2} \varepsilon(k'_2) C_{k'_1, k'_2}}_{(13)}. \tag{3.60}
\end{aligned}$$

This is the equation we work with to derive an equation for $C^K(n)$. Since the derivation is not straightforward, we illustrate some difficult points by dealing with the equation term by term.

Substitution of equation (3.59) and equation (3.43) into equation (3.60) gives rise to:

$$(10) = \frac{1}{\sqrt{N_{\text{mol}}}} \sum_l C^K(l) e^{-i(k_1 - k_2)l/2}, \tag{3.61}$$

$$\begin{aligned}
(11) &= \frac{1}{N_{\text{mol}}} \sum_m G^K(m) e^{-i(k_1 - k_2)m/2} \sum_{k'_1 + k'_2 = k_1 + k_2} D(n) e^{i(k_1 - k'_1)n} \frac{1}{\sqrt{N_{\text{mol}}}} \sum_l C^K(l) e^{-i(k'_1 - k'_2)l/2} \\
&= \frac{1}{N_{\text{mol}} \sqrt{N_{\text{mol}}}} \sum_{m, n, l} \sum_{k'_1 + k'_2 = k_1 + k_2} G^K(m) e^{-i(k_1 - k_2)m/2} D(-n) e^{-i(k_1 - k'_1)n} \\
&\quad \times C^K(l) e^{-i[k'_1 - (k_1 + k_2 - k'_1)]l/2} \\
&= \frac{1}{N_{\text{mol}} \sqrt{N_{\text{mol}}}} \sum_{m, n, l} G^K(m) e^{-i(k_1 - k_2)m/2} D(n) e^{-ik_1 n} C^K(l) e^{i(k_1 + k_2)l/2} \sum_{k'_1 + k'_2 = k_1 + k_2} e^{ik'_1(n-l)} \\
&= \frac{1}{\sqrt{N_{\text{mol}}}} \sum_{m, n, l} G^K(m) e^{-i(k_1 - k_2)m/2} D(n) e^{-ik_1 n} C^K(l) e^{i(k_1 + k_2)l/2} \delta_{n, l} \\
&= \frac{1}{\sqrt{N_{\text{mol}}}} \sum_{m, l} G^K(m) e^{-i(k_1 - k_2)m/2} D(l) C^K(l) e^{-i(k_1 - k_2)l/2}, \tag{3.62}
\end{aligned}$$

$$\begin{aligned}
(11) &= \frac{1}{N_{\text{mol}}} \sum_m G^K(m) e^{-i(k_1 - k_2)m/2} \sum_{k'_1 + k'_2 = k_1 + k_2} \left[E_0 + \sum_n J(n) e^{ik'_1 n} \right] \frac{1}{\sqrt{N_{\text{mol}}}} \sum_l C^K(l) e^{-i(k'_1 - k'_2)l/2} \\
&= \frac{1}{\sqrt{N_{\text{mol}}}} \sum_{m,l} G^K(m) e^{-i(k_1 - k_2)m/2} e^{i(k_1 + k_2)l/2} \left[E_0 C^K(l) \frac{1}{N_{\text{mol}}} \sum_{k'_1 + k'_2 = k_1 + k_2} e^{-ik'_1 l} \right. \\
&\quad \left. + J(l) C^K(l) \frac{1}{N_{\text{mol}}} \sum_{k'_1 + k'_2 = k_1 + k_2} e^{ik'_1 (n-l)} \right] \\
&= \frac{1}{\sqrt{N_{\text{mol}}}} \sum_{m,l} G^K(m) e^{-i(k_1 - k_2)m/2} e^{i(k_1 + k_2)l/2} [E_0 C^K(l) \delta_{l,0} + J(l) C^K(l) \delta_{l,n}] \\
&= \frac{1}{\sqrt{N_{\text{mol}}}} \sum_{m,l} G^K(m) e^{-i(k_1 - k_2)m/2} J(l) C^K(l) e^{iKl}
\end{aligned} \tag{3.63}$$

and

$$(12) = \frac{1}{\sqrt{N_{\text{mol}}}} \sum_{m,l} G^K(m) e^{-i(k_1 - k_2)m/2} J(l) C^K(l) e^{-iKl}. \tag{3.64}$$

A comparison between the left hand side and the right hand side of equation (3.60) indicates that we can eliminate the exponent $e^{-i(k_1 - k_2)m/2}$ from (12) and (13) by exchanging the index l with m . However, term (11) will cause a problem because after exchanging l with m it becomes

$$(11) = \frac{1}{\sqrt{N_{\text{mol}}}} \sum_{m,l} G^K(l) e^{-i(k_1 - k_2)l/2} D(m) C^K(m) e^{-i(k_1 - k_2)m/2}. \tag{3.65}$$

After dividing both sides of equation (3.60) by the common factor $e^{-i(k_1 - k_2)l/2}$, the exponent $e^{-i(k_1 - k_2)m/2}$ will still remain in term (13). As mentioned before, we want to obtain an equation for $C^K(n)$ that has only dependence on the summation of wavevectors $K = k_1 + k_2$, so we don't want $e^{-i(k_1 - k_2)m/2}$ to appear. It turns out this problem can be resolved by making use of the periodicity of the lattices. Due to the translational symmetry of the lattices, $l - m$ takes the same range $(-\infty, \infty)$ as l for a crystal with infinite size, then we can replace the summation over l with the

summation over $l - m$:

$$\begin{aligned} \sum_l G^K(l) e^{-i(k_1-k_2)l/2} &= \sum_{l-m} G^K(l-m) e^{-i(k_1-k_2)(l-m)/2} \\ &= \sum_l G^K(l-m) e^{-i(k_1-k_2)(l-m)/2}. \end{aligned} \quad (3.66)$$

Although this equation is only strictly valid for a lattice with infinite number of sites, we can still use it for the case of a sufficiently large lattices with a large N_{mol} . Substituting equation (3.66) into equation (3.65), we can obtain

$$(11) = \frac{1}{\sqrt{N_{\text{mol}}}} \sum_{m,l} G^K(l-m) D(m) C^K(m). \quad (3.67)$$

Then equation (3.60) reduces to

$$C^K(l) = \sum_m C^K(m) [G^K(l-m)D(m) - 2G^K(l)J(m)\cos(Km)]. \quad (3.68)$$

In the nearest neighbor approximation, the above equation for $C^K(m)$ can be simplified as

$$C^K(l) = C^K(1) \{D(1) [G^K(l-1) + G^K(l+1)] - 2G^K(l)J_K\}, \quad (3.69)$$

where $G^K(l)$ can be calculated from equation (3.57) and J_K is defined by equation (3.54).

Substituting equation (3.57) into equation (3.69) and taking l to be 1, we obtain an equation for the biexciton energy E_b^K which can be solved to give rise to

$$E_b^K = E_0 + D + \frac{J_K^2}{D}. \quad (3.70)$$

Substituting this solution into equation (3.57), we can obtain the expression of $G^K(n)$ in terms of D and J :

$$G^K(n) = \frac{D}{D^2 - J_K^2} \left(\frac{J_K}{D}\right)^{|n|} \quad (3.71)$$

Up to now, everything else except $C^K(l)$ in equation (3.69) are known, therefore every other $C^K(l)$ can be written in terms of $C^K(1)$. Then the normalization condition for $C^K(l)$, i.e., equation (3.49), becomes an equation for $C^K(1)$ only. We can easily solve equation (3.49) by assuming N_{mol} is sufficiently large and $D > J_K$ and then obtain

$$C^K(n) = \frac{\sqrt{D^2 - J_K^2}}{2D} \left(\frac{J_K}{D} \right)^{|n|-1}. \quad (3.72)$$

So the biexciton wave function in the site representation in the nearest neighbor approximation is:

$$\begin{aligned} |\Psi_b(K)\rangle &= \sum_{n,m \neq n} e^{iK(n+m)/2} \psi_K(|n-m|) |\hat{P}_n^\dagger \hat{P}_m^\dagger\rangle, \\ \psi_K(r) &= \frac{\sqrt{D^2 - 4J^2 \cos^2(K/2)}}{2D\sqrt{N_{\text{mol}}}} \left(\frac{2J \cos(K/2)}{D} \right)^{|r|-1}, \end{aligned}$$

where $r = |n - m|$ is the distance between two excitations. Since $J_K = 2J \cos(K/2) > J$, we can see from the biexciton wavefunction that the amplitude $\psi_K(r)$ for two excitations to appear at two sites decays exponentially with the distance between the two sites, which indicates that the biexciton states are indeed bound states.

3.3.3 Properties of biexciton states

Ref. [11] shows that biexcitons can generally form in 1D and 2D crystals if

$$|D| \geq 2|J| \quad (3.73)$$

where D and J are the coupling constants $D(n - m)$ and $J(n - m)$ for $n - m = 1$. In 3D crystals, biexcitons can form if $|D| > 6|J|$ [14]. For 1D crystals, the biexciton energy in the nearest neighbor approximation (NNA) is $E_b(K) = 2E_0 + D + \frac{4J^2 \cos^2(aK/2)}{D}$, where K is the total wave vector of two interacting excitons and a is the lattice constant, and the biexciton binding energy is $\Delta = (D - 2J)^2/D$. The maximum number of exciton-exciton bound states is equal to the dimensionality of the crystal, i.e. one biexciton state for 1D, two for 2D and three for 3D [11, 39].

For molecules in an optical lattice, the magnitudes of J and D depend on the strength of the applied electric field and the angle between the field and the molec-

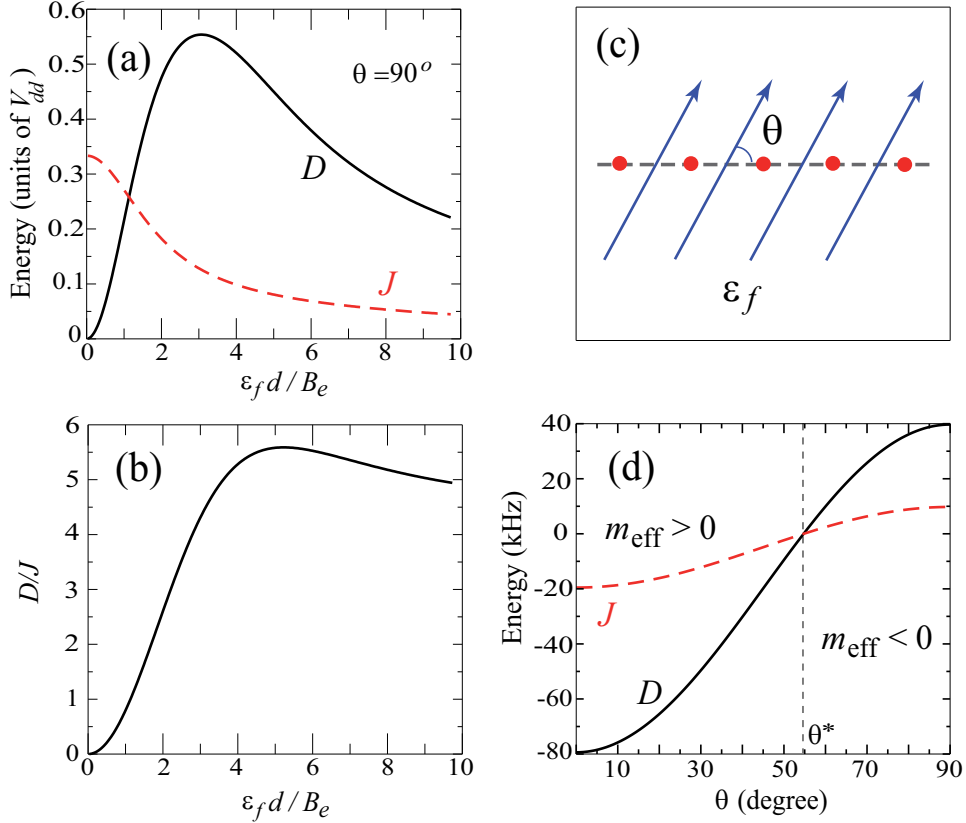


Figure 3.1: (a) The parameters D and J (in units of $V_{dd} = d^2/a^3$) as functions of the electric field strength. (b) The ratio D/J as a function of the electric field strength. The field is perpendicular to the intermolecular axis. For LiCs molecules possessing the dipole moment $d=5.529$ Debye, the value $\epsilon_f d/B_e = 1$ corresponds to $\epsilon_f = 2.12$ kV/cm. (c) Schematic depiction of the angle θ between the field (represented by blue arrows) and the molecular array (represented by red dots). (d) D and J for a 1D array of LiCs molecules separated by 400 nm as functions of θ for $\epsilon_f = 6$ kV/cm.

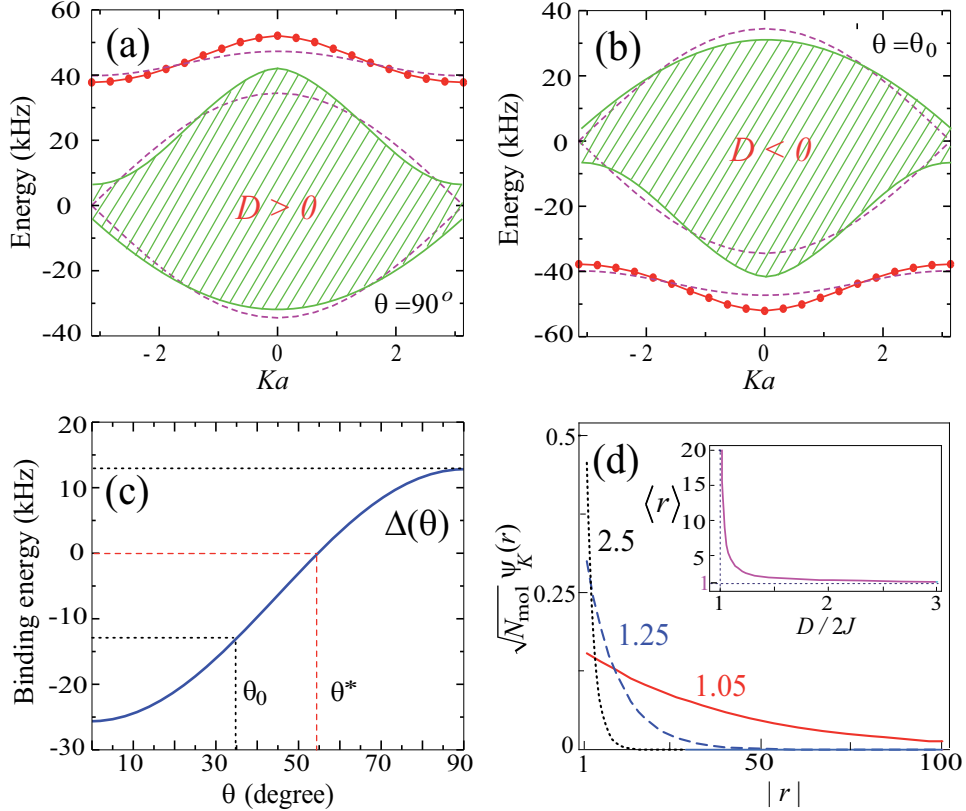


Figure 3.2: (a) and (b): Two-excitation spectra of a 1D array of LiCs molecules on an optical lattice: NNA (dashed lines) and exact solutions (solid lines). The shaded regions encapsulate the bands of the continuum two-exciton states. (c) θ -dependence of the biexciton binding energy Δ . The electric field magnitude is 6.88 kV/cm, $\theta_0 = \arccos\sqrt{2/3}$, $\theta^* = \arccos\sqrt{1/3}$. (d) Biexciton wave function vs the lattice site separation $|r| = |n - m|$ of the two excitations for $K = 0$. Inset: Mean width of the biexciton wave function $\langle r \rangle$ calculated as the width of $\psi_K^2(r)$ at half maximum. Numbers at each curve indicate the value of $D/2J$.

ular array (θ) (see figure (3.1) (c)). We calculate these parameters for a 1D array of ${}^1\Sigma$ polar molecules (such as alkali metal dimers produced in ultracold molecule experiments) trapped on an optical lattice with the lattice separation $a = 400$ nm. Figure (3.1) (b) shows that for a fixed angle θ the ratio D/J increases as the electric field magnitude increases. For LiCs molecules, the condition (3.73) is satisfied for electric fields > 3.6 kV/cm. Note that the ratio D/J is independent of θ .

Frenkel excitons are quasiparticles characterized by an effective mass (m_{eff}). The sign of J determines the sign of the effective mass [20]: negative J corresponds to positive m_{eff} and vice versa (see figure (3.1) (d)). Due to the linearity of the Schrödinger equation, a positive potential is attractive for particles with negative mass, just like a negative potential is attractive for particles with positive mass. Because the sign of J and D is the same (and consequently the signs of D and m_{eff} are opposite), the dynamical interaction (3.6) between excitons in this system is attractive.

To demonstrate the formation of the biexciton and calculate the biexciton energy, we diagonalize the Hamiltonian $\hat{H}_{\text{exc}} + \hat{H}_{\text{dyn}}$ for a one-dimensional array of $N_{\text{mol}} = 501$ LiCs molecules. The matrix of the Hamiltonian is evaluated by expanding the biexciton states as

$$\begin{aligned} |\Psi_b(K)\rangle &= \sum_{\substack{k_1+k_2=K \\ k_1 \geq k_2}} C_{k_1,k_2} |k_1, k_2\rangle \\ &= \sum_{k \geq 0} C_k^K |\hat{P}^\dagger(K/2+k)\hat{P}^\dagger(K/2-k)\rangle, \end{aligned} \quad (3.74)$$

where $K = k_1 + k_2$ and $k = (k_1 - k_2)/2$, and k_1 and k_2 denote the wavevectors of the interacting excitons. The Hamiltonian matrix is diagonalized numerically for fixed values of K , which is conserved. Figure (3.2) shows that for $\theta = 90^\circ > \theta^* = \arccos(1/\sqrt{3})$ the biexciton energy is above the two-exciton continuum (binding for particles with negative mass), and for $\theta = \arccos(\sqrt{2}/3) < \theta^*$ below it (binding for particles with positive mass). The binding energy of the biexciton changes sign at $\theta = \theta^*$. The biexciton wave function $\psi_K(r)$ is plotted in figure (3.2) (d). Figure (3.1) and figure (3.2) thus illustrate that the biexciton binding energy and size can be tuned by varying the strength and orientation of the electric field.

3.4 Non-optical creation of biexcitons

The possibility of formation of Frenkel biexcitons has been proposed quite long ago [40]. However, in contrast to the well-known Wannier-Mott biexcitons in semiconductors, Frenkel biexcitons in solid-state molecular crystal are very difficult to observe. We now explain the reasons. First, many molecular crystals, such as anthracene or naphthalene, possess inversion symmetry. In these crystals, the constant D as defined in the line after equation (3.6) must vanish and equation (3.73) is not satisfied. Second, it is difficult to excite biexciton states optically: it was shown in Ref.[12] that the oscillator strength for the photon-induced transitions to the biexciton state must decrease with the increasing binding energy of the biexcitons. Therefore, two-photon excitation can only produce unstable weakly bound biexcitons. Third, excitons in molecular crystals decay via bimolecular annihilation processes into higher-energy states and subsequent relaxation accompanied by emission of phonons. This process is prohibited by conservation of energy in an optical lattice with diatomic molecules. Figure (3.1) demonstrates that the first obstacle can be removed by tuning the electric field. To overcome the second obstacle, we propose a non-optical method of populating deeply bound biexciton states based on the unique structure of ${}^1\Sigma$ polar molecules. As zero electric field the rotational states $|g\rangle$ and $|e\rangle$ are separated by the energy $\Delta\epsilon_{e-g} = 2B_e$, while the energy separation between state $|e\rangle$ and the next rotationally excited state $|f\rangle \equiv |N=2, M_N=0\rangle$ is equal to $\Delta\epsilon_{e-f} = 4B_e$. As the electric field increases, $\Delta\epsilon_{e-g}$ increases faster than $\Delta\epsilon_{e-f}$ (see figure (3.3)). When $\mathcal{E}_f d / B_e \simeq 3.24$ (corresponding to $\mathcal{E}_f \simeq 6.88$ kV/cm for LiCs), $\Delta\epsilon_{f-g} = 2\Delta\epsilon_{e-g}$. At electric fields near this magnitude, two $|g\rangle \rightarrow |e\rangle$ excitons can undergo the transition to the $|f\rangle$ state, and, inversely, the $|g\rangle \rightarrow |f\rangle$ excitation can produce a pair of $|g\rangle \rightarrow |e\rangle$ excitons or a biexciton state depicted in figure (3.2). The coupling between states $|e\rangle$ and $|f\rangle$ is $\hat{H}_{12} = \sum_{n \neq m} M(n-m) \hat{R}_n \hat{P}_n^\dagger \hat{P}_m^\dagger$, where $M(n-m) = \langle e_n, e_m | V_{dd}(n-m) | f_n, g_m \rangle$, and the operator \hat{R}_n annihilates the $|f\rangle$ excitation in lattice site n . The total Hamiltonian describing this three-level system is $\hat{H}_{g-e-f} = \hat{H}_{\text{exc}} + \hat{H}_{\text{dyn}} + \hat{H}_2 + \hat{H}_{12}$, where $\hat{H}_2 = E_f \sum_n \hat{R}_n^\dagger \hat{R}_n + \sum_{n,m \neq n} J_{g-f}(n-m) \hat{R}_n^\dagger \hat{R}_m$ and $J_{g-f}(n-m) = \langle g_n, f_m | V_{dd}(n-m) | f_n, g_m \rangle$.

In order to calculate the probability of the population transfer from state f to the biexciton state, we solve the time-dependent Schrödinger equation with the

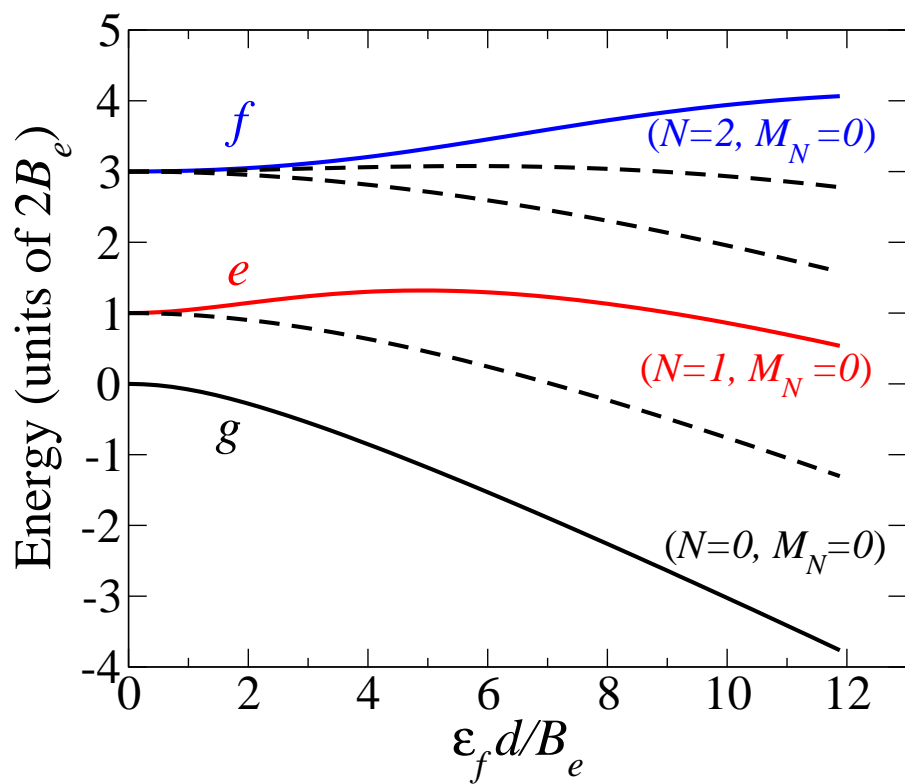


Figure 3.3: The rotational energies of a closed-shell polar molecule as functions of the strength of the DC field. The dashed lines represent other rotational states with $M_N \neq 0$.

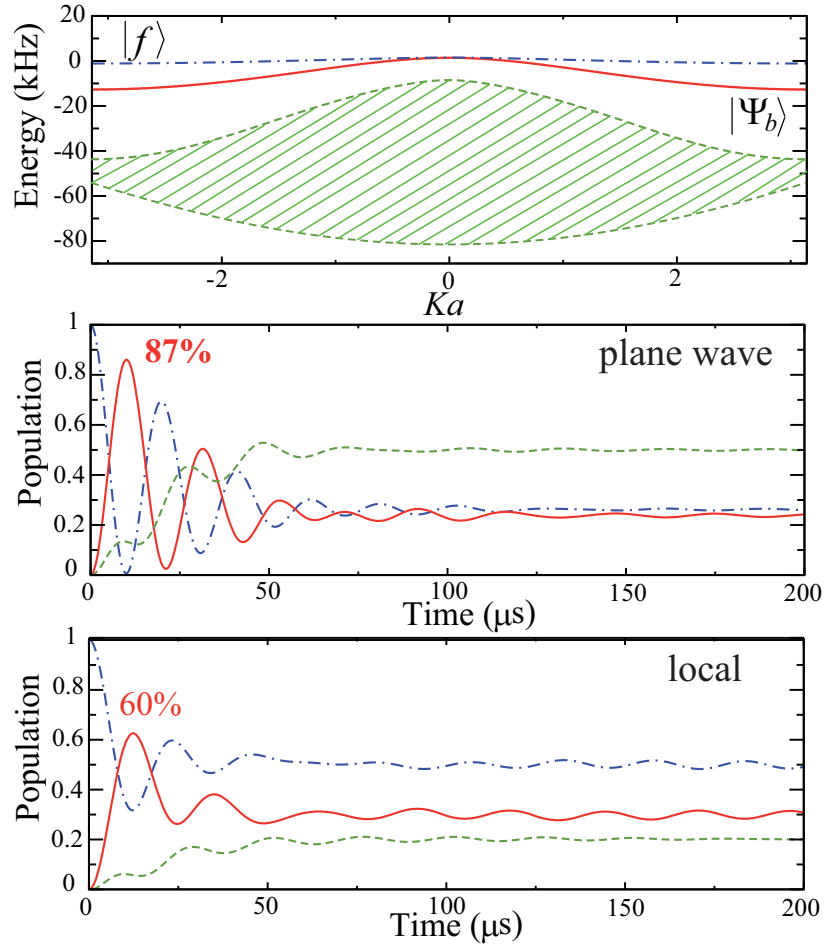


Figure 3.4: Population dynamics for the transition from $|g\rangle \rightarrow |f\rangle$ exciton (middle panel) and from an f state localized on a single molecule (lower panel) to coherent $|g\rangle \rightarrow |e\rangle$ excitons and biexcitons. The green dashed curves denote the population accumulated in the pairs of non-bound $|g\rangle \rightarrow |e\rangle$ exciton states, the red solid curves the biexciton state and the blue dot-dashed curves the f state. The shaded region in the upper panel encapsulates the band of the continuum two-exciton states. The calculation is for a 1D ensemble of $N_{mol} = 501$ LiCs molecules on an optical lattice with lattice separation $a = 400$ nm. The electric field of magnitude 6.88 kV/cm is perpendicular to the molecular array.

Hamiltonian \hat{H}_{g-e-f} evaluated in the basis of products of the eigenstates of $\hat{H}_{\text{exc}} + \hat{H}_{\text{dyn}}$ and the eigenstates of \hat{H}_2 . This leads to coupled differential equations:

$$i\hbar\dot{\mathbf{C}} = \mathbf{H}\mathbf{C} , \quad (3.75)$$

where \mathbf{C} is a vector that represents a wavefunction in the basis set and $\dot{\mathbf{C}}$ is its derivative with respect to time. Since the total Hamiltonian \mathbf{H} is time-independent, we can make a basis-set transformation to diagonalize \mathbf{H}

$$\mathbf{U}^T \mathbf{H} \mathbf{U} = \mathbf{D} , \quad (3.76)$$

so that \mathbf{C} in the new basis set can then be solved by direct integration and then \mathbf{C} in the original basis set can be found by the inverse basis-set transformation. Multiplying both sides of equation (3.75) by \mathbf{U}^T , we obtain

$$i\hbar\mathbf{U}^T\dot{\mathbf{C}} = \mathbf{U}^T \mathbf{H} \mathbf{U} \mathbf{U}^T \mathbf{C} , \quad (3.77)$$

where $\mathbf{U}\mathbf{U}^T = \mathbf{I}$ has been used. Let's define

$$\mathbf{A} \equiv \mathbf{U}^T \mathbf{C} , \quad (3.78)$$

then

$$\dot{\mathbf{A}} = \mathbf{U}^T\dot{\mathbf{C}} \quad (3.79)$$

because \mathbf{H} is time-independent and \mathbf{U}^T must be time-independent too. So equation (3.75) can be rewritten as

$$i\hbar\dot{\mathbf{A}} = \mathbf{D}\mathbf{A} , \quad (3.80)$$

which can solved easily by direct integration:

$$\mathbf{A}(t) = e^{-\frac{i}{\hbar}\mathbf{D}t} \mathbf{A}(0) . \quad (3.81)$$

Substituting equation (3.78) into equation (3.81), we get

$$\mathbf{C}(t) = \mathbf{U} e^{-\frac{i}{\hbar}\mathbf{D}t} \mathbf{U}^T \mathbf{C}(0) , \quad (3.82)$$

where \mathbf{D} is a diagonal matrix whose non-zero elements are the eigenvalues of \mathbf{H} , and each column of \mathbf{U} is an eigenvector of \mathbf{H} . Therefore, given the eigenvalues and eigenvectors of the total Hamiltonian and the initial wavefunction $\mathbf{C}(0)$, the wavefunction $\mathbf{C}(t)$ at any time t can be calculated from equation (3.82). In our numerical calculations, we use subroutines from the LAPACK library to calculate the eigenvalues and eigenvectors of the matrix.

The magnitude of J_{g-f} is about ten times smaller than J . In the absence of decoherence, the $|g\rangle \rightarrow |f\rangle$ excitation gives rise to the Frenkel exciton and the transition from the f states to the biexciton state is a coherent exciton-exciton transition. In the presence of decoherence, the exciton states become localized. If the decoherence rate is larger than J_{g-f}/h , but smaller than J/h , the $|g\rangle \rightarrow |f\rangle$ excitation is localized, while the biexciton states remain coherent. Figure (3.4) presents the calculations of the population transfer probabilities for both scenarios. The results show that the biexciton states can be populated with high efficiency. The equilibrium populations (in the limit of large t) depend on the relative energies of the f state, the biexciton bound state and exciton-exciton continuum states, which can be tuned by varying the electric field magnitude. The efficiency of the population transfer can be maximized if the electric field is detuned far away from resonance when the biexciton population oscillations reach the first maximum. Detuning the electric field to low magnitudes effectively decouples the f state from the states in the $\{g, e\}$ subspace and interrupts the population dynamics. This corresponds to switching off the channel for bimolecular annihilation of excitons, which is one of the reasons of the biexciton population depletion in solids. We have confirmed that the calculations with electric fields < 5.0 kV/cm yield no noticeable population transfer.

3.5 Extension to exciton trimers

In Section 3.3, it is shown that Frenkel rotational biexcitons exist under some conditions in optical lattices. Then the question arises naturally: if two excitons can bind together, what about three excitons? In this section, we extend the method to handle the three-exciton case and answer the question about exciton trimers.

Similar to the case of biexciton, we define a three-exciton wavefunction in site

representation

$$|\Psi\rangle = \sum_{n_1, n_2, n_3} C_{n_1, n_2, n_3} \hat{P}_{n_1}^\dagger \hat{P}_{n_2}^\dagger \hat{P}_{n_3}^\dagger |0\rangle , \quad (3.83)$$

and start from the Schrödinger equation with the same Hamiltonian $\hat{H} = \hat{H}_{\text{exc}} + \hat{H}_{\text{dyn}}$

$$\hat{H}|\Psi\rangle = E_{\text{trimer}}|\Psi\rangle . \quad (3.84)$$

Since two excitations can't sit at the same molecule, we have the constraint on C_{n_1, n_2, n_3} :

$$C_{n_1, n_2, n_3} = 0 \text{ if } n_1 = n_2 \text{ or } n_2 = n_3 \text{ or } n_1 = n_3 . \quad (3.85)$$

After similar derivations as we did for the biexciton case, equation (3.84) and equation (3.85) lead to

$$\begin{aligned} & [3E_0D(n_1 - n_2) + D(n_1 - n_3) + D(n_2 - n_3) - E_{\text{trimer}}] C_{n_1, n_2, n_3} \\ & + \sum_n [J(n - n_1)C_{n, n_2, n_3} + J(n - n_2)C_{n_1, n, n_3} + J(n - n_3)C_{n_1, n_2, n}] \\ & = 2\delta_{n_1, n_2} \sum_n J(n_1 - n)C_{n, n_2, n_3} + 2\delta_{n_2, n_3} \sum_n J(n_2 - n)C_{n_1, n, n_3} \\ & + 2\delta_{n_1, n_3} \sum_n J(n_3 - n)C_{n_1, n_2, n} . \end{aligned} \quad (3.86)$$

Note that the equation can't be used to determine the values of C_{n_1, n_2, n_3} when any two of n_1 , n_2 , and n_3 are equal. Using the following Fourier transform

$$C_{n_1, n_2, n_3} = \frac{1}{(\sqrt{N_{\text{mol}}})^3} \sum_{k_1, k_2, k_3} C(k_1, k_2, k_3) e^{i(k_1 n_1 + k_2 n_2 + k_3 n_3)} \quad (3.87)$$

we can transform equation (3.86) to

$$\begin{aligned} & \frac{1}{N_{\text{mol}}} \sum_q \tilde{D}(q) [C(k_1 - q, k_2 + q, k_3) + C(k_1 - q, k_2, k_3 + q) + C(k_1, k_2 - q, k_3 + q)] \\ & + [\epsilon(k_1) + \epsilon(k_2) + \epsilon(k_3) - E_{\text{trimer}}] C(k_1, k_2, k_3) \\ & = \frac{2}{N_{\text{mol}}} \sum_q [\tilde{J}(k_1 - q)C(k_1 - q, k_2 + q, k_3) + \tilde{J}(k_2 - q)C(k_1, k_2 - q, k_3 + q) \\ & + \tilde{J}(k_3 - q)C(k_1 + q, k_2 + q, k_3 - q)] , \end{aligned} \quad (3.88)$$

which can be written as an eigenvalue problem

$$\sum_{k'_1+k'_2+k'_3=K} \mathbf{A}_{k_1 k_2 k_3; k'_1 k'_2 k'_3} C(k'_1, k'_2, k'_3) = E_{\text{trimer}} C(k_1, k_2, k_3), \quad (3.89)$$

where

$$\begin{aligned} \mathbf{A}_{k_1 k_2 k_3; k'_1 k'_2 k'_3} &= \delta_{k_1, k'_1} \delta_{k_2, k'_2} \delta_{k_3, k'_3} [\varepsilon(k_1) + \varepsilon(k_2) + \varepsilon(k_3)] \\ &\quad + \frac{1}{N_{\text{mol}}} \left\{ \delta_{k_1, k'_1} [\tilde{D}(k_2 - k'_2) - 2\tilde{J}(k'_2)] \right. \\ &\quad \left. + \delta_{k_2, k'_2} [\tilde{D}(k_3 - k'_3) - 2\tilde{J}(k'_3)] \right. \\ &\quad \left. + \delta_{k_3, k'_3} [\tilde{D}(k_1 - k'_1) - 2\tilde{J}(k'_1)] \right\}. \end{aligned} \quad (3.90)$$

The above equations clearly show that only those coefficients $C(k_1, k_2, k_3)$ whose wavevectors add up to a fixed K are coupled to each other. Therefore, the eigenvalues for each value of K can be calculated independently. However, since we assumed that $C_{n_1, n_2, n_3} = 0$ when any two of n_1, n_2, n_3 are equal, we need to take care of the constraint when solving equation (3.89).

Let's examine the effect of the constraint on C_{n_1, n_2, n_3} . Assuming k_3 is fixed, we have

$$\begin{aligned} \sum_{k_1+k_2=K-k_3} C(k_1, k_2, k_3) &= \sum_{k_1} \sum_{n_1, n_2, n_3} \frac{1}{(\sqrt{N_{\text{mol}}})^3} e^{i(k_1 n_1 + k_2 n_2 + k_3 n_3)} C_{n_1, n_2, n_3} \\ &= \sum_{n_1, n_2, n_3} \frac{1}{\sqrt{N_{\text{mol}}}} \left(\frac{1}{N_{\text{mol}}} \sum_{k_1} e^{i k_1 (n_1 - n_2)} \right) e^{i(K-k_3) n_2} e^{i k_3 n_3} C_{n_1, n_2, n_3} \\ &= \sum_{n_1, n_2, n_3} \frac{1}{\sqrt{N_{\text{mol}}}} \delta_{n_1, n_2} e^{i(K-k_3) n_2} e^{i k_3 n_3} C_{n_1, n_2, n_3} \\ &= \sum_{n_2, n_3} \frac{1}{\sqrt{N_{\text{mol}}}} e^{i(K-k_3) n_2} e^{i k_3 n_3} C_{n_2, n_2, n_3} \\ &= 0. \end{aligned} \quad (3.91)$$

Since the fixed wavevector k_3 can be chosen arbitrarily, a condition similar to equation (3.91) will hold for a fixed k_1 and a fixed k_2 as well. This means: for a particular K if you add up all $C(k'_1, k'_2, k'_3)$ whose first (second or third) wavevector

k'_1 (k'_2 or k'_3) equal to a fixed k , you will get zero. Thus we can add the zero

$$\frac{1}{N_{\text{mol}}} \sum_{k'_1, k'_2, k'_3} \left[-2\tilde{J}(k_2)\delta_{k'_1, k_1} C(k'_1, k'_2, k'_3) - 2\tilde{J}(k_3)\delta_{k'_2, k_2} C(k'_1, k'_2, k'_3) - 2\tilde{J}(k_1)\delta_{k'_3, k_3} C(k'_1, k'_2, k'_3) \right] = 0 \quad (3.92)$$

to the left hand side of equation (3.89) to produce a new equation

$$\sum_{k'_1 + k'_2 + k'_3 = K} \mathbf{B}_{k_1 k_2 k_3; k'_1 k'_2 k'_3} C(k'_1, k'_2, k'_3) = E_{\text{trimer}} C(k_1, k_2, k_3), \quad (3.93)$$

where

$$\begin{aligned} \mathbf{B}_{k_1 k_2 k_3; k'_1 k'_2 k'_3} &= \delta_{k_1, k'_1} \delta_{k_2, k'_2} \delta_{k_3, k'_3} [\varepsilon(k_1) + \varepsilon(k_2) + \varepsilon(k_3)] \\ &\quad + \frac{1}{N_{\text{mol}}} \left\{ \delta_{k_1, k'_1} \left[\tilde{D}(k_2 - k'_2) - 2\tilde{J}(k_2) - 2\tilde{J}(k'_2) \right] \right. \\ &\quad \left. + \delta_{k_2, k'_2} \left[\tilde{D}(k_3 - k'_3) - 2\tilde{J}(k_3) - 2\tilde{J}(k'_3) \right] \right. \\ &\quad \left. + \delta_{k_3, k'_3} \left[\tilde{D}(k_1 - k'_1) - 2\tilde{J}(k_1) - 2\tilde{J}(k'_1) \right] \right\}. \end{aligned} \quad (3.94)$$

The advantage of equation (3.93) over equation (3.89) is that the matrix \mathbf{B} is symmetric, which leads to easier diagonalization.

The energies of three-exciton states can be obtained by diagonalizing the matrix \mathbf{B} in equation (3.93) and filtering out the eigenvalues whose corresponding eigenvectors don't satisfy equation (3.91). As a proof-of-principle example, we have solved equation (3.93) for a small lattices under the nearest-neighbor approximation and presented the results in figure (3.5). As can be seen from the figure, three excitons may form a three-body bound state or a biexciton plus a free exciton. Since the energies of three-body bound states are located outside the energy continuum of a biexciton plus a free exciton, an interesting question arise: does three-body bound states of excitons exist when two-body bound states don't form, that is, does the Efimov effect occur in the current case? Unfortunately, numerical investigation shows that the three-body and two-body bound states always occur at the same time when D/J reaches 2, indicating no Efimov effect. However, this

is not a conclusive result as only the interaction between nearest neighbors are included in the calculation and the effect of long-range interaction need to be examined.

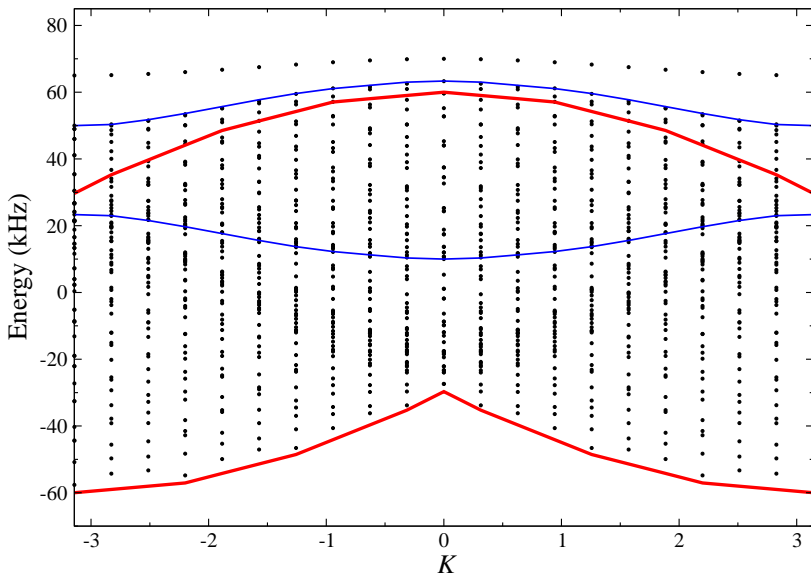


Figure 3.5: Three-excitation spectra of a 1D array of molecules on an optical lattice. The calculation is done for a system of 20 lattice sites with the hopping interaction $J = 10$ kHz and the dynamic interaction $D = 30$ kHz. The black dots represent energies of all three-exciton states, the red curves denote the boundaries of energy continuum of three free excitons, and the blue curves represent the boundaries of energy continuum for a biexciton plus a free exciton.

3.6 Discussion

We have shown that rotational excitation of molecules trapped on an optical lattice gives rise to rotational excitons whose interactions can be controlled by an external electric field. The exciton–exciton interactions can be tuned to produce two-exciton

bound states. A biexciton is an entangled state of two Frenkel excitons. The creation of biexcitons as described in the previous section and tuning the electric field to the regime of zero binding energy can thus be used for the controlled preparation of entangled pairs of non-interacting excitons. In order to observe the biexcitons, one could measure correlations between the populations of the rotationally excited states of molecules in different lattice sites using the method proposed in Ref. [35].

The present work suggests several interesting questions. For example, it was recently shown that Frenkel excitons in shallow optical lattices can be coupled to lattice phonons, leading to polarons [41]. Coupling a Frenkel biexciton to phonons would produce strongly interacting polarons. It would be interesting to explore if these interactions lead to the formation of bipolarons.

We have repeated the calculations presented here for a system of three excitons and similarly observed the formation of three-exciton bound states. It would be interesting to explore the effect of tunable exciton–exciton interactions on excitation correlations, both as a function of D/J and the density of excitations, to understand fundamental limits of exciton clustering [42].

The creation of biexcitons with tunable binding energy and measuring quantum energy transport for different ratios D/J can be used to study the effects of exciton–exciton entanglement on energy transfer in molecular aggregates [43–45]. The ability to tune exciton–exciton interactions can be used to explore the role of multiple excitation correlations on energy transfer in disordered systems (the confining lattice potential can be tilted or the molecules can be perturbed by a disorder potential produced by an inhomogeneous electric field).

Chapter 4

Non-adiabatic control of quantum energy transfer in ordered and disordered arrays

An elementary excitation in an aggregate of coupled particles generates a collective excited state. We show that the dynamics of these excitations can be controlled by applying a transient external potential which modifies the phase of the quantum states of the individual particles. The method is based on an interplay of adiabatic and sudden time scales in the quantum evolution of the many-body states. We show that specific phase transformations can be used to accelerate or decelerate quantum energy transfer and spatially focus delocalized excitations onto different parts of arrays of quantum particles. We consider possible experimental implementations of the proposed technique and study the effect of disorder due to the presence of impurities on its fidelity. We further show that the proposed technique can allow control of energy transfer in completely disordered systems.

4.1 Introduction

The experiments with ultracold atoms and molecules trapped in optical lattices have opened a new frontier of condensed-matter physics research. The unique properties of these systems – in particular, large (> 400 nm) separation of lattice

sites, the possibility of tuning the tunnelling amplitude of particles between lattice sites by varying the trapping field and the possibility of controlling interparticle interactions with external electric or magnetic fields – offer many exciting applications ranging from quantum simulation of complex lattice models [25–34, 46–49] to the study of novel quasi-particles [50] that cannot be realized in solid-state crystals. In the limit of strong trapping field, each site of an optical lattice is populated by a fixed number of ultracold atoms or molecules. Such states can be produced with either bosonic or fermionic particles [48, 51]. Here, we consider an optical lattice fully or partially filled with one particle per lattice site, and assume that tunnelling between lattice sites is completely suppressed. Such an array can be thought of as a prototype of a system, in which a single lattice site (or a small number of lattice sites) can be individually addressed by an external field of a focused laser beam. This can be exploited for engineering the properties of quantum many-body systems by changing the energy of particles in individual lattice sites [52].

In the present work, we consider the generic problem of energy transfer – i.e. the time evolution of an elementary quantum excitation – in such a system. In particular, we explore the possibility of controlling energy transfer through an array of coupled quantum monomers by applying monomer-specific external perturbations. This is necessary for several applications. First, collective excitations in molecular arrays in optical lattices have been proposed as high-fidelity candidates for quantum memory [23, 24]. The ability to manipulate collective excitations is necessary for building scalable quantum computing networks [53]. Second, ultracold atoms and molecules in optical lattices can be perturbed by a disorder potential with tunable strength [54]. Engineering localized and delocalized excitations in such systems can be used to investigate the role of disorder-induced perturbations on quantum energy transfer, a question of central importance for building efficient light-harvesting devices [55]. Third, the possibility of controlling energy transfer in an optical lattice with ultracold atoms or molecules can be used to realize inelastic scattering processes with both spatial and temporal control. Finally, control over energy transfer in quantum systems can be used for studying condensed-matter excitations and energy transport without statistical averaging.

An excitation of a coupled many-body system generates a wave packet rep-

resenting a coherent superposition of single-particle excitations. The method proposed here is based on shaping such many-body wave packets by a series of sudden perturbations, in analogy with the techniques developed for strong-field alignment and orientation of molecules in the gas phase [56]. Alignment is used in molecular imaging experiments and molecular optics [56–59], and is predicted to provide control over mechanical properties of molecular scattering [60, 61]. Here, we consider the use of similar techniques for controlling quantum energy transfer in an interacting many-body system. When applied to a completely ordered system, the proposed method is reminiscent of the techniques used to move atoms in optical lattices, where a uniform force is applied for a short period of time [62]. The conceptual difference comes from the fact that in the present case the momentum is acquired by a quasi-particle – a collective excitation distributed over many monomers. During the subsequent evolution, the particles do not move – rather, the excitation is transferred from one monomer to another. In order to control such excitations, we exploit an interplay of the adiabatic and sudden time scales, which correspond to single-monomer and multi-monomer evolution. We also exploit the wave-like nature of the excitation wave function to draw on the analogy with wave optics. This analogy, too, is not complete due to the discrete nature of the lattice.

In order to emphasize the generality of the proposed method, we formulate the problem in terms of the general Hamiltonian parameters. We then describe in detail how the required external perturbations can be realized in experiments with ultracold atoms and molecules. The possibility of using rotational excitations in molecular arrays is particularly interesting due to the long lifetime of rotationally excited states. Electronic excitations of atoms in an optical lattice may also give rise to collective excitations [63]. However, the lifetime of these excited states is limited by fast spontaneous emission [64, 65]. We propose a mechanism for suppressing spontaneous decay by tailoring the properties of the excitation wave packets.

The paper has the following structure. Section (4.2) and Section 4.3 present the results in terms of the general Hamiltonian parameters. Section (4.4) addresses the particular case of ultracold atoms and molecules. Section (4.5) discusses controlled energy transfer in systems with, specifically, dipole - dipole interactions. Section (4.6) considers the effects of lattice vacancies on the possibility of con-

trolling energy transfer and Section 4.7 extends the proposed technique to control of excitation dynamics in strongly disordered arrays with a large concentration of impurities. Section (4.8) presents the conclusions.

4.2 Sudden phase transformation

Consider, first, an ensemble of N coupled identical monomers possessing two internal states arranged in a one-dimensional array with translational symmetry. The Hamiltonian for such a system is given by

$$H_{\text{exc}} = \Delta E_{e-g} \sum_n |e_n\rangle\langle e_n| + \sum_{n,m} \alpha(n-m) |e_n, g_m\rangle\langle g_n, e_m|, \quad (4.1)$$

where $|g_n\rangle$ and $|e_n\rangle$ denote the ground and excited states in site n , ΔE_{e-g} is the monomer excitation energy and $\alpha(n-m)$ represents the coupling between two monomers at sites n and m . Any singly excited state of the system is given by

$$|\psi_{\text{exc}}\rangle = \sum_{n=1}^N C_n |e_n\rangle \prod_{i \neq n} |g_i\rangle. \quad (4.2)$$

In general, the expansion coefficients C_n are complicated functions of n determined by the properties of the system, in particular, the translational invariance or lack thereof as well as the strength of disorder potential. If an ideal, periodic system with lattice constant a is excited by a single-photon transition, the expansion coefficients are $C_n = e^{iakn}/\sqrt{N}$ and $|\psi_{\text{exc}}\rangle \Rightarrow |k\rangle$ represents a quasi-particle called Frenkel exciton, characterized by the wave vector k [3]. The magnitude of the wave vector k is determined by the conservation of the total (exciton plus photon) momentum. The energy of the exciton is given by

$$E(k) = \Delta E_{e-g} + \alpha(k) \quad (4.3)$$

with $\alpha(k) = \sum_n \alpha(n) e^{-iakn}$. In the nearest neighbor approximation,

$$E(k) = \Delta E_{e-g} + 2\alpha \cos ak, \quad (4.4)$$

where $\alpha = \alpha(1)$.

With atoms or molecules on an optical lattice, it is also possible to generate a localized excitation placed on a single site (or a small number of sites) by applying a gradient of an external electric or magnetic field and inducing transitions in selected atoms by a pulse of resonant electromagnetic field [35]. The presence of a disorder potential, whether coming from jitter in external fields or from incomplete population of lattice sites, also results in spatial localization. Similar to how equation (4.2) defines the collective excited states in the basis of lattice sites, the same excitation state $|\psi_{\text{exc}}\rangle$ can be generally written as a coherent superposition of the exciton states $|k\rangle$ with different k :

$$|\psi\rangle = \sum_k G_k |k\rangle, \quad (4.5)$$

where G_k 's are the fourier transforms of C_n 's in equation (4.2).

Control over energy transfer in an ordered array can be achieved by (i) shifting the exciton wave packets in the momentum representation (which modifies the group velocity and the shape evolution of the wave packets) and (ii) focusing the wave packets in the coordinate representation to produce localized excitations in an arbitrary part of the lattice. To achieve this, we propose to apply a series of site-dependent perturbations that modify the phases of the quantum states of spatially separated monomers. These phase transformations change the dynamics of the time evolution of the collective excitations. Here we consider the transformations leading to acceleration or deceleration of collective excitations, while the focusing phase transformations are described in Section 4.3.

4.2.1 Group velocity of wave packet

Before we discuss how to accelerate or decelerate the motion of collective excitations, we first need to figure out what determine their propagation behaviors. It turns out that the propagation behavior of an exciton wave packet can be implied from the exciton dispersion curve. More specifically, the first derivative of the dispersion curve gives approximately the propagation speed of a wave packet in real space. This can be easily shown by simple derivations.

In a perfect crystal, the eigenstates of the system is characterized by a wavevec-

tor k and its time evolution is determined by $E(k)$ through

$$\begin{aligned} |k(t)\rangle &= e^{-i\frac{E(k)}{\hbar}t}|k(t=0)\rangle \\ &= \frac{1}{\sqrt{N}} \sum_n e^{i[kan - \frac{E(k)}{\hbar}t]} |n(t=0)\rangle \end{aligned} \quad (4.6)$$

where N is the number of sites in the crystal and $|n(t=0)\rangle$ represents the state of system in which only site n is in the excited state. It can be seen from equation (4.6) that the probability at each site is always $1/N$ for state $|k\rangle$. So the plane wave $|k\rangle$ doesn't move in real space, which is expected. Different from a plane wave state, a wave packet composed of different $|k(t)\rangle$ states is not stationary in real space. This is because different $|k(t)\rangle$ components correspond to different energy $E(k)$ thus different evolutions, leading to a time-dependent interference pattern in real space. To illustrate this point, we consider a Gaussian wave packet in k space

$$\begin{aligned} |\psi(t)\rangle &= A \sum_k e^{-\frac{(k-k_0)^2}{2\sigma_k^2}} |k(t)\rangle \\ &= \frac{A}{\sqrt{N}} \sum_k e^{-\frac{(k-k_0)^2}{2\sigma_k^2}} \sum_n e^{i[kan - \frac{E(k)}{\hbar}t]} |n(t=0)\rangle , \end{aligned} \quad (4.7)$$

where A is the normalization constant. Expanding $E(k)$ around the point $k = k_0$ and ignoring second and higher-order terms of $(k - k_0)$, and replacing the summation over k by integration, we obtain an equation that describes the time-evolution of the wave packet in real space:

$$|\psi(t)\rangle = A' \sum_n e^{-\frac{(n-v_g t)^2}{2(1/\sigma_k)^2}} |n(t=0)\rangle , \quad (4.8)$$

where A' is some constant that normalizes the wavefunction and the group velocity

$$v_g = \frac{1}{\hbar} \left. \frac{dE(k)}{dk} \right|_{k=k_0} \quad (4.9)$$

determines how fast the center of the wave packet moves in real space. Therefore, once the exciton dispersion curve is known, the propagation speed of a wave packet that centered around k_0 in momentum space can be calculated from the slope of

dispersion curve at k_0 .

4.2.2 Phase kicking in quasimomentum space

As an example, figure (4.1) presents an exciton dispersion curve. It can be seen that different regions of the dispersion curve have different slopes that correspond to different group velocities. Direct optical excitation can create an exciton wave packet which centers around $k \approx 0$ in the k space. However, such a wave packet hardly travel in real space as a whole since its group velocity is zero. Based on figure (4.1), if we want accelerate a $k = 0$ wave packet, a sensible way is to move the wave packet to the region near $k = \pi/2$ where the slope of the dispersion curve is deep. Similarly, to decelerate a wave packet we should move it to a place where the slope is more shallow. Now the problem of accelerating/decelerating an exciton wave packet becomes the problem of moving the wave packet as a whole in k space.

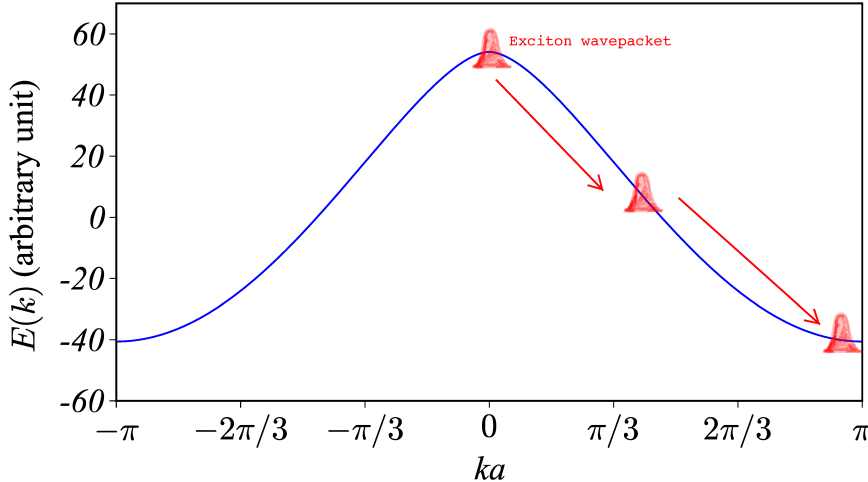


Figure 4.1: The dispersion curve of an exciton. The interaction between site m and site n is proportional to $1/|n - m|^3$.

But how do we move an exciton wave packet in k space without changing its

shape? We can get some hint from the expression of the plane wave state

$$|k(t)\rangle = \frac{1}{\sqrt{N}} \sum_n e^{ikan} |n(t)\rangle . \quad (4.10)$$

Equation (4.10) suggests that we can change $|k\rangle$ to $|k + \delta\rangle$ by adding a factor $e^{i\delta an}$ to each term in the expansion. Since the increment δ is independent of the $|k\rangle$ state, each $|k\rangle$ component in a wave packet (equation (4.2)) can be transformed into $|k + \delta\rangle$ in this way. This transformation shifts the wave packets by δ in k -space while preserving their shape. As a result, one can engineer wave packets probing any part of the dispersion $E(k)$ leading to different group velocity and shape evolution.

Knowing that adding the proper phases is a key step, we now study how to add those phases. There are two different time scales involved: one is related to the evolution of the free monomer states, $T_m = \hbar/\Delta E_{e-g}$, and the other is related to the excitation population transfer between monomers, $T_e = \hbar/\alpha$. Usually, T_m is smaller than T_e by several orders of magnitude. This huge difference in magnitude enable us to work with the adiabatic and sudden time scales at the same time as described below. Consider the n -th monomer subjected to an external field $\mathcal{E}_n(t)$ which varies from 0 to some value and then back to 0 in time T . If the variation is adiabatic with respect to the evolution of the free monomer states, $T \gg T_m$, each eigenstate $|f\rangle$ of the monomer acquires a state-dependent phase shift [66]

$$|f_n(T)\rangle = e^{i\phi_n^f} |f_n(0)\rangle , \quad (4.11)$$

where

$$\phi_n^f = -\frac{1}{\hbar} \int_0^T E_n^f(t) dt , \quad (4.12)$$

$E_n^f(t)$ is the instantaneous eigenenergy and f can be e or g . Now consider the action of such phase change on the collective excitation state (4.2). If $T \ll T_e$, the change is sudden with respect to the excitation transfer between monomers, so during the time T the excitation probability doesn't have enough time to propagate between different monomers and C_n 's in equation (4.2) remain almost the same. Since G_k 's are just fourier transforms of C_n 's, G_k will remain the same as well, conserving the

shape of the wave packet $|\psi_{\text{exc}}\rangle$ in k space. Then the wave packet $|\psi_{\text{exc}}\rangle$ acquires a site-dependent phase $\Phi_n = \phi_n^e - \phi_n^g$ that will influence each $|k\rangle$ component in the same way. If $\Phi_n = \Phi_0 + na\delta$, then the momentum δ is imparted onto the excitonic wavefunction without changing its shape. By analogy with “pulsed alignment of molecules” [56], we call this transformation a “phase kick” or “momentum kick”. Its action is also similar to that of a thin prism on a wavefront of a monochromatic laser beam.

In order to illustrate the shifting of exciton wave packets in the momentum space, we solve numerically the time-dependent Schrödinger equation with the unperturbed Hamiltonian (4.1), subjected to a transient site-dependent external perturbation that temporarily modulates ΔE_{e-g} . We choose the parameters $\Delta E_{e-g} = 12.14$ GHz, $\alpha = 22.83$ kHz and the lattice constant $a = 400$ nm that correspond to an array of polar molecules trapped in an optical lattice, as described in detail in Section 4.4. The time-dependent perturbation has the form of a short pulse with the duration $T = 3 \mu\text{s}$. The phase acquired by the particles during this time is given by $\Phi_n \simeq \Phi_0 - 1.29n$, which can be achieved with a focused laser beam, as described in Section 4.4.

The excitation at $t = 0$ is described by a Gaussian wave packet of the exciton states $|\psi_{\text{exc}}(k)\rangle$, with the central wavevector $k = 0$. Figure (4.2) shows that the entire wave packet acquires momentum during the external perturbation pulse (left panels). This is manifested as a phase variation in the coordinate representation, and as a shift of the central momentum in the k -representation. After the external perturbation is gone, the wave packet does not evolve in the k -representation and moves with the acquired uniform velocity in the coordinate representation.

As a side note, we find that if the laser intensity remains the same after reaching the maximum, the oscillation of the wave packet in momentum and coordinate space can be observed (see figure (4.3)). This phenomenon is a special Bloch oscillation since the force is acting on a quasi-particle rather than real particles in conventional cases [67], which allows for the possibility to study condensed-matter excitations and energy transport without statistical averaging.

The results presented in figure (4.2) and all subsequent results of this work are for a single collective excitaion in an interacting many-particle system. A general experimental implementation may result in multiple excitations, leading to non-

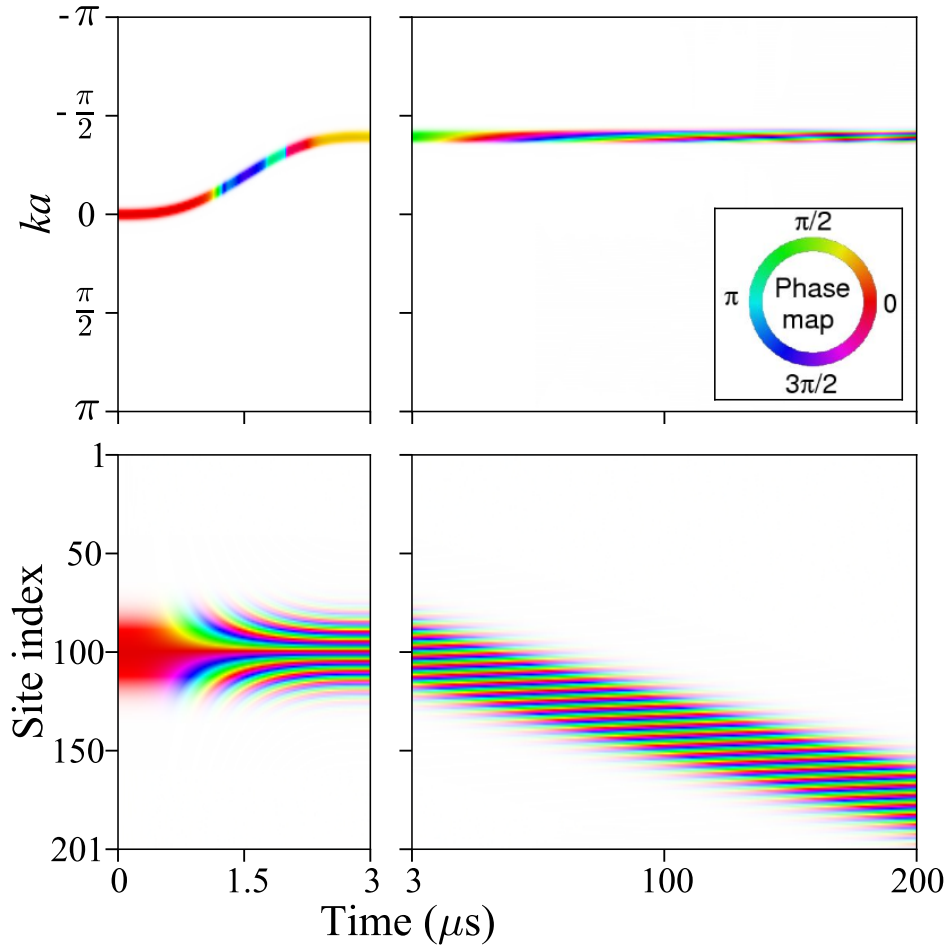


Figure 4.2: Example of controlled energy transfer in a one-dimensional array of quantum monomers subjected to a linear phase transformation. The graph illustrates the evolution of the exciton wave packet centered at $k = 0$ and initially positioned at the center of the array. The phase of the wave function is shown by color. The brightness of color corresponds to the amplitude of the excitation with white color corresponding to zero amplitude. The calculation is for a one-dimensional array of 201 monomers with $\alpha = 22.83$ kHz and $\Delta E_{e-g} = 12.14$ GHz, and the linear phase transformation $\Phi_n \simeq \Phi_0 - 1.29n$. The corresponding experimental setup is illustrated in figure (4.6)

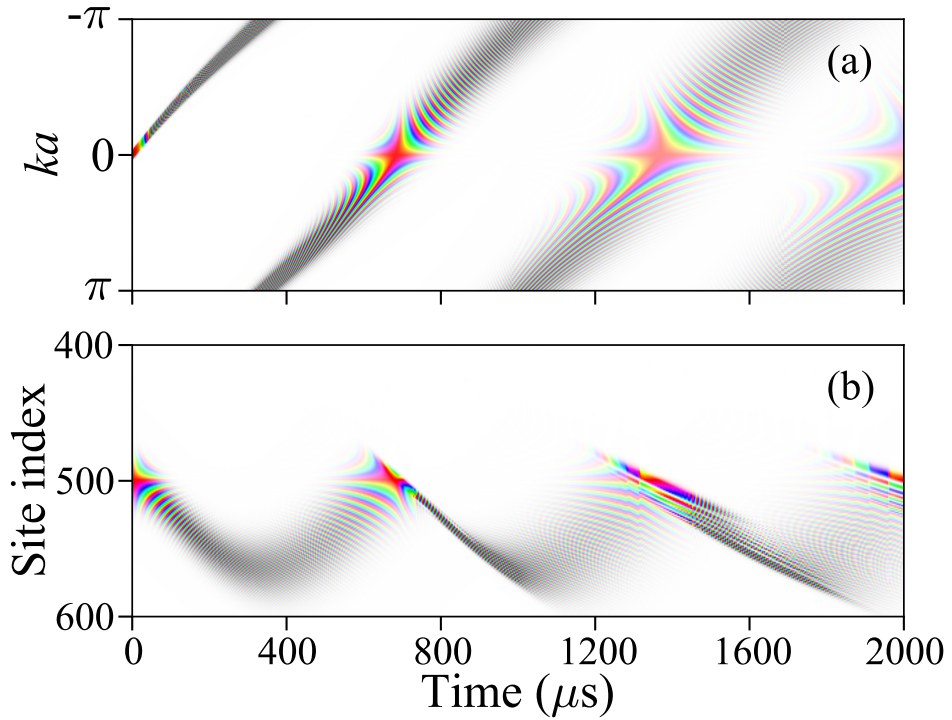


Figure 4.3: “Bloch oscillation” of the exciton wave packet in the momentum and coordinate spaces. The phase of the wave function is shown by color as in figure (4.2). A low laser intensity of 10^6 W/cm^2 is used and all other parameters are the same as in figure (4.2). Part (a) shows that the wave packet moves in k space in response to the linear laser field. However, since the wave vector is limited in the first Brillouin zone, when the wave packet reaches $-\pi$ or π , it disappears at the boundary and reappears at the other boundary. Part (b) presents the motion of the wave packet in coordinate space in accordance with the phase kicking in k space. Note that the wave packet spreads in both the momentum and coordinate spaces because the laser intensity profile along the molecular array is not perfect and this is amplified over extended time period.

linear exciton interactions. There are two mechanisms for exciton - exciton interactions: kinematic interactions arising from the statistical properties of excitons and dynamical interactions determined by the matrix elements of the inter-particle interactions in the Hilbert sub-space of binary excitations [3, 68]. The effects of the kinematic interactions on energy transfer in molecular crystals have never been observed so these interactions are considered to be weak, especially in the limit of a small number of excitations easily achievable in experiments [69]. For molecules on an optical lattice, the dynamical interactions are important in the presence of strong external electric fields where molecular states of different parity are strongly mixed [20, 50]. At weak parity-mixing fields considered here, the exciton-exciton interactions insignificantly mix different k states of the individual excitons, contributing weakly to localization. These effects are expected to be much smaller than the disorder-induced perturbations, discussed in Section 4.6 and Section 4.7.

4.3 Focusing of a delocalized excitation

In order to achieve full control over excitation transfer, it is desirable to find a particular phase transformation that focuses a delocalized many-body excitation onto a small part of the lattice, ideally a single lattice site. In optics, a thin lens focuses a collimated light beam by shifting the phase of the wavefront, thus converting a plane wave to a converging spherical wave. Similarly, a phase kick can serve as a time domain “lens” for collective excitations: an excitation initially delocalized over a large number of monomers can be focused onto a small region of the array after some time. By analogy with optics, a concave or convex symmetric site-dependent phase $\Phi(n)$ applied simultaneously to all monomers may turn a broad initial distribution $C_n(t = 0)$ into a narrow one.

The dynamics of the excitation state in the lattice is determined by the time dependence of the coefficients $C_n(t)$ in equation (4.2). In order to find the expression for $C_n(t)$, we expand the amplitudes at $t = 0$ in a Fourier series

$$C_n(t = 0) = \sum_q \frac{e^{iqan}}{\sqrt{N}} C(q; t = 0) \quad (4.13)$$

and apply the propagator $e^{-iE(q)t/\hbar}$ to each q -component with $E(q)$ representing the

exciton energy given by equation (4.4). Transforming the amplitudes $C(q)$ back to the site representation then yields

$$C_m(t) = \frac{1}{N} \sum_{n,k} C_n(t=0) e^{i[\Phi(n)+ka(m-n)-E(k)t/\hbar]}, \quad (4.14)$$

where $\Phi(n)$ is a site-dependent phase applied at $t = 0$, as described in the previous section. Note that the phase $\Phi(n)$ does not have to be applied instantaneously. The phase $\Phi(n,t)$ can be applied continuously over an extended time interval as long as the accumulated phase gives the desired outcome $\int_0^T \Phi(n,t) dt = \Phi(n)$.

4.3.1 Focusing to a single site

As equation (4.14) shows, the focusing efficiency is determined by the phase transformation and the shape of the dispersion curve $E(k)$. Given the cosine dispersion of excitons (4.4), is it possible to focus a delocalized excitation onto a single lattice site? To answer this question, we assume an initial condition where the excitation is localized to the site n_0 , that is,

$$C_n(t=0) = \delta_{n,n_0}, \quad (4.15)$$

and run a backward-in-time evolution to calculate the coefficients $C_m(t)$ at $t = -\tau$: using the expansion of an exponent in Bessel functions (Jacobi-Anger expansion, see Ref. [70])

$$e^{ia \cos x} = \sum_n e^{-i(x-\pi/2)n} J_n(a), \quad (4.16)$$

we obtain

$$\begin{aligned}
C_m(-\tau) &= \frac{1}{N} \sum_{n,k} C_n(t=0) e^{i[ka(m-n)-E(k)(-\tau)/\hbar]} \\
&= \frac{1}{N} \sum_{n,k} C_n(t=0) e^{i[ka(m-n)]} \sum_{n'} e^{-i(ka-\pi/2)n'} J_{n'}(2\alpha\tau/\hbar) \\
&= \frac{1}{N} \sum_{n,k} \delta_{n,n_0} e^{i[ka(m-n)]} \sum_{n'} e^{-i(ka-\pi/2)n'} J_{n'}(2\alpha\tau/\hbar) \\
&= \frac{1}{N} \sum_k e^{ika(m-n_0)} \sum_{n'} e^{-i(ka-\pi/2)n'} J_{n'}(2\alpha\tau/\hbar) \\
&= \sum_{n'} e^{i\pi n'} J_{n'}(2\alpha\tau/\hbar) \left(\frac{1}{N} \sum_k e^{ika(m-n_0-n')} \right) \\
&= \sum_{n'} e^{i\pi n'} J_{n'}(2\alpha\tau/\hbar) \delta_{n',m-n_0} \\
&= e^{i\pi(m-n_0)/2} J_{m-n_0}(2\alpha\tau/\hbar), \tag{4.17}
\end{aligned}$$

where J is the Bessel function of first kind. This calculation shows that an wavepacket with the site representation, i.e., $C_m(0) = e^{i\pi(m-n_0)/2} J_{m-n_0}(2\alpha t/\hbar)$, will focus onto the lattice site n_0 after evolving for time t . We can be easily verify the result by running a forward-in-time evolution starting with the initial wave packet and making use of the orthonormality of the Bessel functions

$$\sum_n J_n(x) J_{n-m}(x) = \delta_{m,0}. \tag{4.18}$$

Equation (4.17) shows that the focusing of a wave packet onto a single site would require not only adding the phase $\Phi(n) = \text{Arg}[C_m(-\tau)]$, but also the amplitude modulations of the coefficients equal to the absolute values of $C_m(-\tau)$. This second task is beyond the manipulation tools considered here. However, creating such a wave packet may require multiple and complicated phase transformations, which may be difficult to realize in experiments.

4.3.2 Focusing a broad wavepacket in coordinate space

A simpler procedure can be implemented if the phase transformations are restricted to a particular part of the exciton dispersion. From wave optics, waves with quadratic dispersion can be focused, while those with linear dispersion propagate without changing the wave packet shape [71, 72]. It is this interplay of the quadratic (at low k) and linear (at $k \approx \pm\pi/2a$) parts of the cosine-like exciton dispersion (equation (4.4)) that precludes perfect focusing of a general collective excitation. In order to avoid the undesirable amplitude modulations, it may be possible to focus delocalized excitations by a phase transformation that constrains the wave packet (4.5) to the quadratic part of the dispersion $E(k)$. For such wave packets, adding a quadratic phase $\Phi(n) = \Phi_0(n - n_0)^2$ must lead to focusing around site n_0 . Below we illustrate the effect of the quadratic phase transformation for a broad wave packet in coordinate space. In the next subsection (Section 4.3.3), we continue to explore the case of a plane wave.

Consider a Gaussian wave packet with a narrow width $\sigma_{k,0}$ which centers around $k = 0$ in k space

$$C_k = A e^{-\frac{a^2 k^2}{2\sigma_{k,0}^2}}, \quad (4.19)$$

where A is some normalization factor. Since these normalization factors doesn't matter for the discussion here, we will just ignore them in the following derivations. The wave packet represented by equation (4.19) is also a Gaussian wave packet in coordinate space. This can be verified by the following transformation from k space

to coordinate space :

$$\begin{aligned}
C_n &= \frac{1}{\sqrt{N}} \sum_k C_k(t=0) e^{ikan} \\
&\approx \frac{A}{\sqrt{N}} \int_{-\infty}^{\infty} dk e^{-\frac{a^2 k^2}{2\sigma_{k,0}^2} + ikan} \\
&= \frac{A}{\sqrt{N}} e^{-\frac{n^2}{2\sigma_{k,0}^2}} \int_{-\infty}^{\infty} dk e^{-\frac{1}{2\sigma_{k,0}^2}(ka - in\sigma^2)^2} \\
&= \frac{A}{\sqrt{N}} \frac{\sigma_{k,0} \sqrt{2\pi}}{a} e^{-\frac{n^2 \sigma_{k,0}^2}{2}} \\
&\propto e^{-\frac{n^2}{2(1/\sigma_{k,0})^2}}, \tag{4.20}
\end{aligned}$$

where in the second step we use the integration to approximate the summation of k in the first Brillouin zone and extend the integration range from $(-\pi/a, \pi/a]$ to $(-\infty, \infty)$ since the width σ_k is very small. Equation (4.20) also shows the width of the wave packet in coordinate space is the inverse of its width in k space, that is, $\sigma_{x,0} = 1/\sigma_{k,0}$.

To focus the wave packet, we apply an inhomogeneous phase $\Phi(n) = \Phi_0(n - n_0)^2$ at $t = 0$. Then the wave packet becomes

$$C_n(t=0) \propto e^{-\frac{n^2}{2(1/\sigma_{k,0})^2}} e^{i\Phi_0(n-n_0)^2}, \tag{4.21}$$

which upon a transformation from coordinate space to k space gives rise to

$$\begin{aligned}
C_k(t=0) &= \frac{1}{\sqrt{N}} \sum_n C_n(t=0) e^{-ikan} \\
&\approx \frac{1}{\sqrt{N}} \int_{-\infty}^{\infty} dn C_n(t=0) e^{-ikan} \\
&\propto e^{\frac{-a^2 k^2 + 4akn_0\Phi_0 + 2in_0^2\sigma_{k,0}^2\Phi_0}{2(\sigma_{k,0}^2 - 2i\Phi_0)}}. \tag{4.22}
\end{aligned}$$

The power of e in equation (4.22) can be separated into a real part and an imaginary part. Since the imaginary part contributes only a trivial phase to the wavefunction

and doesn't change the shape of the wave packet, we can ignore it and obtain

$$C_k(t=0) \propto e^{-\frac{\sigma_{k,0}^2(ka-2n_0\Phi_0)^2}{2(\sigma_{k,0}^4+4\Phi_0^2)}}. \quad (4.23)$$

So the width of the wave packet after adding the phase is

$$\sigma_k(t=0) = \sqrt{\sigma_{k,0}^2 + \frac{4\Phi_0^2}{\sigma_{k,0}^2}}, \quad (4.24)$$

which is obviously larger than the initial width $\sigma_{k,0}$. This indicates that the phase applied for focusing cannot be too large otherwise the wave packet will be broadened beyond the quadratic region of the dispersion curve where the focusing scheme doesn't work. Note that the phase does not affect the width of the wave packet in coordinate space since it only adds some phase to the coefficients $C_n(t=0)$ in equation (4.20).

To see how the wave packet evolves after the phase adding, we can apply the propagator $e^{-iE(k)t/\hbar}$ to equation (4.23) and convert the wavefunction into coordinate space. Assuming the width $\sigma_k(t=0)$ is very small so that a large proportion of the wave packet is within the quadratic region of the dispersion curve, then the eigen energy of of the $|k\rangle$ state can be approximated as

$$E(k) \approx E_0 + \beta a^2 k^2. \quad (4.25)$$

Using equation (4.25), we obtain the wavefunction of the wave packet after time t

$$\begin{aligned} C_n(t) &= \frac{1}{\sqrt{N}} \sum_k e^{ikan} e^{-iE(k)t} C_k(0) \\ &\propto \sum_k e^{ikan} e^{-iE(k)t/\hbar} e^{-\frac{\sigma_{k,0}^2(ka-2n_0\Phi_0)^2}{2(\sigma_{k,0}^4+4\Phi_0^2)}} \\ &\propto e^{-\frac{(n+4t\beta\Phi_0 n_0)^2}{2\sigma_k^2(t)}} \end{aligned} \quad (4.26)$$

where $\sigma_x(t)$ is a time-dependent width given by

$$\sigma_x(t) = \sigma_{x,0} \sqrt{(1+4t\beta\Phi_0)^2 + \frac{4t^2\beta^2}{\sigma_{x,0}^4}}. \quad (4.27)$$

Taking the derivative of $\sigma_x(t)$ with respect to time and setting it to zero, we can find the time at which the wave packet is most focused:

$$T_F = -\frac{\Phi_0 \sigma_{x,0}^4}{\beta \left(1+4\Phi_0^2 \sigma_{x,0}^4\right)}. \quad (4.28)$$

At time T_F , the minimum width is

$$\sigma_{x,F} = \frac{\sigma_{x,0}}{\sqrt{1+4\Phi_0^2 \sigma_{x,0}^4}}, \quad (4.29)$$

and the center of the wave packet is

$$n_c = 4T_F \beta \Phi_0 n_0 = \frac{4\Phi_0^2}{\sigma_{k,0}^4 + 4\Phi_0^2} n_0 \approx n_0. \quad (4.30)$$

Equation (4.29) shows that the wave packet will become more focused at site n_0 at T_F since $\sigma_{x,F} < \sigma_{x,0}$ and a larger phase Φ_0 will lead to a better focusing effect. However, as we have discussed before, large values of Φ_0 may take the wave packet outside the quadratic part of the dispersion making equation (4.25) invalid. Therefore, the best focusing effect can only be achieved by balancing the two influences.

In the case of exciton with the cosine dispersion curve represented by equation (4.4), $\beta = -\alpha a^2$. To find the optimal phase Φ_0^* that keeps the wave packet within the quadratic dispersion while focusing it, we use the condition $\sigma_{k,0} \lesssim 1$, which yields $\Phi_0^* = \pm 1/2\sigma_{x,0}$ for the optimal focusing. At time

$$t_* \approx 1/4\alpha\Phi_0^*, \quad (4.31)$$

the wave packet is most focused and has a width

$$a\sigma_{x,F}(\Phi_0^*) = \frac{a\sigma_{x,0}}{\sqrt{1+4\Phi_0^{*2}\sigma_{x,0}^4}} \sim a. \quad (4.32)$$

For the time t_* in equation (4.31) to be positive, α and Φ_0^* must have the same sign. Therefore, a convex quadratic phase profile $\Phi(n)$ with $\Phi_0 > 0$ must focus collective excitations in a system with repulsive couplings between particles in different lattice sites ($\alpha > 0$), and a concave quadratic phase profile $\Phi(n)$ with $\Phi_0 < 0$ must focus excitations in a system with attractive couplings ($\alpha < 0$).

4.3.3 Focusing a plane wave in coordinate space

Consider a completely delocalized excitation (4.2) with $C_n(k; t=0) = e^{iakn}/\sqrt{N}$ describing an eigenstate of an ideal system of N coupled monomers. Suppose $E(k)$ in equation (4.14) can be approximated as $E(k) = \Delta E_{e-g} - \alpha a^2 k^2$. As we have seen in the derivation of last section, the effect of $E(k)$ on the wave packet is to add a phase due to time evolution, i.e. $e^{-iE(k)t}$. Since ΔE_{e-g} in $E(k)$ contributes the same phase to all k component and thus adds a trivial phase to the whole wavefunction, we can safely ignore it if only the shape of the wavefunction is concerned. Therefore, we use $E(k) = -\alpha a^2 k^2$ instead in the following derivation. To focus the plane wave, the quadratic phase $\Phi(n) = \Phi_0 n^2$ are applied at $t = 0$. This changes the initial wavefunction to

$$C_n(k; t=0) = \frac{1}{\sqrt{N}} e^{ikan} e^{i\Phi_0 n^2}, \quad (4.33)$$

which renders the wavefunction a wave packet in k space with the coefficient:

$$C_q(t=0) = \frac{1}{\sqrt{N}} \sum_n e^{-iqan} C_n(k; t=0). \quad (4.34)$$

Each q component in equation (4.34) evolves according to

$$C_q(t) = e^{-iE(q)t} C_q(0) = e^{i\alpha a^2 q^2 t} C_q(0), \quad (4.35)$$

then the wavefunction in coordinate space after time t is given by

$$\begin{aligned}
C_m(t) &= \frac{1}{\sqrt{N}} \sum_q e^{iqam} C_q(t) \\
&= \frac{1}{N\sqrt{N}} \sum_q e^{iqam} e^{i\alpha a^2 q^2} \sum_n e^{-iqan} e^{ikan} e^{i\Phi_0 n^2} \\
&= \frac{e^{-i\alpha a^2 k^2}}{N} \sqrt{\frac{i\pi}{N\Phi_0}} \sum_q e^{i[a^2(k-q)^2(\alpha t - 1/4\Phi_0) + qa(m+2\alpha ak)]} \\
&\quad \times \Theta\left(-\frac{N\Phi_0}{a} < k - q < \frac{N\Phi_0}{a}\right), \tag{4.36}
\end{aligned}$$

where $\Theta(z) = 1$ if z is true and zero otherwise. In order to derive equation (4.36), we used the approximate equality

$$\int_{-M}^M dx e^{-i(ax^2+bx)} \approx \sqrt{\frac{\pi}{ia}} e^{ib^2/4a} \Theta(-2Ma < b < 2Ma), \tag{4.37}$$

obtained by approximating the error function of a complex argument $\text{Erf}(\sqrt{ix})$ by the sign function, which is accurate for large argument x .

At time $t_* = 1/4\alpha\Phi_0$, the terms quadratic in q in equation (4.36) are canceled, and the sum over q reduces to a delta-function, if the summation limits are from $-\pi/a$ to π/a . Therefore, the choice $\Phi_0 = \pi/N$ yields

$$C_m(t) = \sqrt{i} e^{-iNa^2k^2/4\pi} \delta_{m,-v_k}, \tag{4.38}$$

where v_k is the index of the initial wave vector $k = 2\pi v_k/Na$, quantized due to the discreteness of the lattice. According to step function $\Theta(z)$ in equation (4.36), the dimensionless width of the wave packet in the wave vector space is $\Delta_k(\Phi_0) \equiv a\sigma_k(\Phi_0) \approx 2N\Phi_0$. When $\Phi_0 = \pi/N$, the wave packet spreads over the entire Brillouin zone, including the linear parts of the exciton dispersion. Using equation (4.37) we find that for an arbitrary value of $\Delta_k(\Phi_0)$, the site amplitudes at the

time of focusing $t_* = 1/4\alpha\Phi_0$ are

$$C_n(k; t = t_*) \approx \frac{e^{i\Delta(\Phi_0)n^2/2N}}{n} \sqrt{\frac{2i}{\pi\Delta_k(\Phi_0)}} \sin(n\Delta_k(\Phi_0)/2). \quad (4.39)$$

In order to keep the linear part of the dispersion spectrum unpopulated, we choose the optimal focusing phase $\Phi_0^* \sim 1/2N$, so that $\Delta_k(\Phi_0^*) \sim 1$.

4.3.4 Numerical results

In Section 4.3.2 and Section 4.3.3, equation (4.32) and equation (4.39) are derived based on the cosine dispersion curve which are valid for a many-body system with nearest neighbor interactions only. In most physical systems, the energy dispersion is modified by long-range couplings. In order to confirm that the above predictions are also valid for systems with long-range interactions and illustrate the focusing of delocalized excitations, we compute the time evolution of the wave packets by solving the wave equation numerically for a system with long-range dipole-dipole interactions. In the calculations, we expanded the Hamiltonian (4.1) in the site basis, i.e. $\{|e_n\rangle \prod_{i \neq n} |g_i\rangle\}$, and applied the corresponding phase to the state $|e_n\rangle$ of each site at $t = 0$ and then run the time evolution to obtain the wavefunction at each time point and save them to files. To find the time for the optimal focusing, we searched for the largest probability at the target focusing site while scanning the wavefunctions at every time point. Figure 4.4 illustrates the focusing dynamics of a completely delocalized excitation (panels a and b) and a broad Gaussian wave packet (panels c and d) in a system with all (first neighbour, second neighbour, etc.) couplings explicitly included in the calculation. The results show that the collective excitations can be focused to a few lattice sites. The role of the long-range coupling will be explicitly discussed in Section 4.6.

The focusing scheme demonstrated above can be generalized to systems of higher dimensionality. To illustrate this, we repeated the calculations presented in Figures 4.4 (c) and 4.4 (d) for a delocalized excitation placed in a square 2D lattice with an external potential that modulates the phase as a function of both x and y . Figure (4.5) shows the focusing of an initially broad wave packet onto different parts of a 2D lattice induced by the quadratic phase transformation $\Phi(x,y) =$

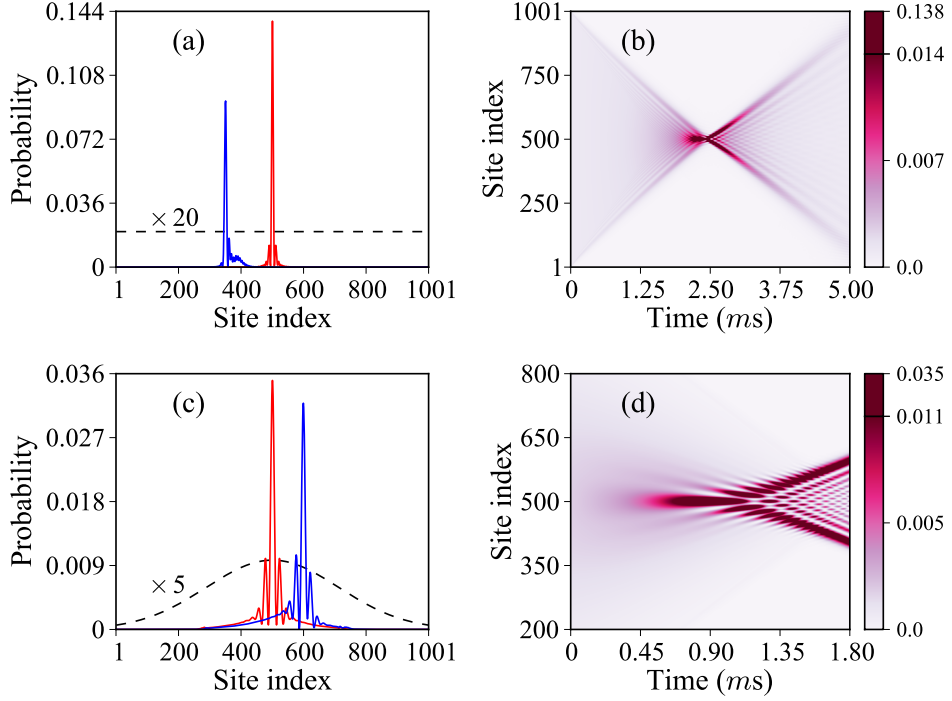


Figure 4.4: Focusing of a completely delocalized collective excitation (panels a and b) and a broad Gaussian wave packet of Frenkel excitons (panels c and d) in a one-dimensional array using the quadratic phase transformations at $t = 0$ as described in text. In panels (b) and (d), the excitation probability distribution is displayed by color. The dashed lines show the initial distribution magnified by 20 and 5 respectively in (a) and (c). The solid curves in panels (a) and (c) correspond to two different phase transformations focusing the same wave packet onto different parts of the array. The calculations are performed with the same parameters α , a , and ΔE_{e-g} as in Figure 4.2. The results are computed with all couplings accounted for.

$\Phi_0[(n_x - n_{x_0})^2 + (n_y - n_{y_0})^2]$, where n_x and n_y are the lattice site indices along the x and y directions. The calculations include all long-range couplings as in figure (4.4). The comparison of figure (4.4) and figure (4.5) illustrates that the focussing efficiency in 2D is greater. The results also demonstrate that the delocalized excitations can be effectively focused on different parts of the lattice simply by varying the reference site (n_{x_0}, n_{y_0}) in the phase transformation.

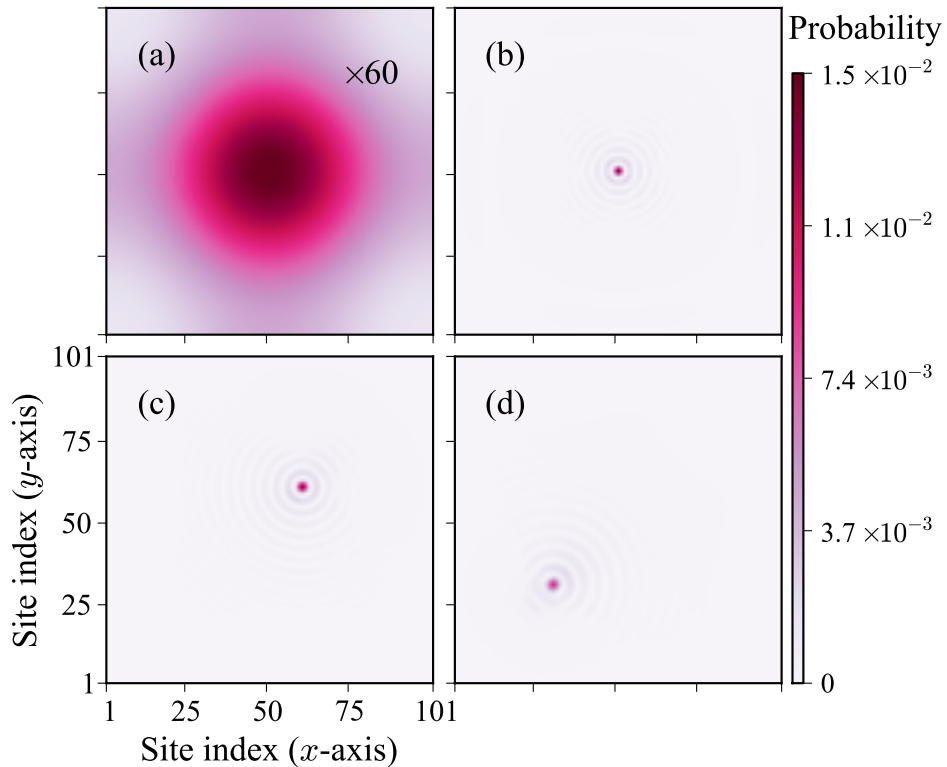


Figure 4.5: Focusing of a delocalized excitation in a 2D array shown at $t = 0$ in panel (a) onto different parts of the lattice (panels b–d). For better visualization, the probability distribution in panel (a) is magnified by a factor of 60. The calculations are performed with the same parameters α , a , and ΔE_{e-g} as in Figure 4.2 and the quadratic phase transformation at $t = 0$.

4.4 Experimental feasibility of phase transformation

In Section 4.2 and Section 4.3, we have discussed the idea of phase kicking and its application in focusing delocalized excitations, but we were mainly concerned with the theoretical perspective. So in this section, we focus on the experimental feasibility and show the techniques proposed in Section 4.2 and Section 4.3 can be realized with ultracold atoms or molecules trapped in an optical lattice with one particle per lattice site [73–76]. There are three general requirements that must be satisfied:

- (i) The time required for a phase transformation must be shorter than the spontaneous decay time of the excited state.
- (ii) The overall coherence of the system must be preserved on the time scale of the excitonic evolution in the entire array, set by $K\hbar/\alpha$, where K is the number of monomers participating in the dynamics of the collective excitation.
- (iii) The lattice constant must be large enough to allow considerable variation of the external perturbation from site to site.

Optical lattices offer long coherence times (> 1 sec) and large lattice constants (> 400 nm) [77]. The lifetime of the collective excitations depends on the internal states of the particles used in the experiment and the momentum distribution of the excitonic states in the wave packet (4.5). In the following two subsections, we discuss the case of ultracold atoms and the case of ultracold molecules separately.

4.4.1 Suppressing spontaneous emission in system of ultracold atoms

For ultracold alkali metal atoms in an optical lattice, an optical excitation may generate collective states (4.2), as discussed in Ref. [64, 65]. The lifetime of these excited states is limited by the spontaneous emission of the electronically excited atoms and is in the range of 10 - 30 ns. However, the collective excited states can be protected from spontaneous emission if the wave vector range populated by excitons in the wave packet (4.5) is outside of the so-called light cone, so that $k > \Delta E_{e-g}/\hbar c$. To understand why this is the case, we investigate the interaction of

the collective excitation state of atoms with light. An photon can excite an exciton state of ultracold atoms and the exciton can also decay as a photon. During these optical processes, the energy is conserved, which leads to

$$E_{\text{ph}} = \hbar c k = \hbar c \sqrt{k_{\parallel}^2 + k_{\perp}^2} = E_{\text{ex}}(k_{\text{ex}}) , \quad (4.40)$$

where k and k_{ex} are the wave vectors of the photon and the exciton respectively. As written in equation (4.40), the wave vector of the photon can be decomposed into two parts: the part (k_{\parallel}) that is parallel to k_{ex} ; and the other part (k_{\perp}) that is perpendicular to k_{ex} . Since only the parallel component of k is conserved in the optical excitation, we have

$$k_{\parallel} = k_{\text{ex}} < k . \quad (4.41)$$

The exciton energy $E_{\text{ex}}(k_{\text{ex}})$ in equation (4.40) can be approximated by the corresponding excitation energy ΔE_{e-g} since the interaction α between atoms is much smaller than the energy gap between the ground state and the excited state of a single atom (see equation (4.3)). Then the wave vector of the photon can be calculated from equation (4.40):

$$k_* = \frac{\Delta E_{e-g}}{\hbar c} . \quad (4.42)$$

Since the wave vector k_{ex} is just the parallel component of k_* , only the excitonic states with $k_{\text{ex}} \leq k_*$ can satisfy both the energy conservation (equation (4.40)) and the momentum conservation (equation (4.41)) at the same time, and thus interact with light. By comparing k_* and the largest value of k_{ex} in the first Brillouin zone $(-\pi/a, \pi/a]$, we can obtain the number of excitonic k -states in the bright and dark regions. For Frenkel excitons originating from electronic transitions in solid-state crystals, the wavelength of excitation light λ_0 (\sim several hundred nm) is much bigger than the lattice constant a (\sim a few Å), the bright region is narrow: $k_{\text{ex}} < k_* = 2\pi/\lambda_0 \approx 0$. For atoms trapped in optical lattices, the typical values of λ_0 are of the same magnitude as the lattice constant a (several hundred nm), and a large portion of the dispersion curve lies in the bright region and the dark region may be narrow. In an ideal infinite system those states in the dark region have infinitely long radiative lifetimes, as there is no free-space photon they can emit, assuming the conservation of both energy and momentum [3, 64, 65, 78]. In finite

and/or disordered systems, the emission of photons may occur at the array boundaries or due to perturbations breaking the translational symmetry. In this case, the time scale for spontaneous decay must depend on the size of the system (i.e. the probability of the excitation to reach the array boundary) and the disorder potential breaking the translational symmetry.

Once collective excited states are created, the phase-kicking technique introduced in Section 4.2, if implemented on a time scale faster than the radiative lifetime of a single atom, can be used to shift the excited states in the wave vector space away from the bright region (cf. figure (4.2)) and thus protect the excited states from fast spontaneous decay. This phase transformation can be induced by a pulse of an off-resonant laser field \mathcal{E}_{AC} , detuned from the $e \leftrightarrow g$ resonance by the value $\delta\omega$, leading to the AC Stark shift (see e.g. Ref.[71])

$$\Delta E_{AC} = \mathcal{E}_{AC}^2 \frac{V_{eg}^2}{4\delta\omega}, \quad (4.43)$$

where V_{eg} is the matrix element of the dipole-induced transition. By choosing $V_{eg} = 1$ a.u., $\delta\omega = 3V_{eg}$, and the laser intensity $I = 5 \times 10^{10}$ W/cm², we obtain that the shift $\phi = \Delta E_{AC} \times T_{\text{pulse}} = \pi$ can be achieved in less than 1 ns. Another phase transformation can bring the excited state back to the bright region, where it can be observed via fast spontaneous emission. The experiments with ultracold atoms have demonstrated the lattice filling factor reaching 99 % [73–75]. The phase transformations proposed here can be used to stabilize excitonic states in ultracold atomic ensembles against spontaneous emission for multiple interesting applications [63, 79].

4.4.2 Phase kicking in system of ultracold molecules

The spontaneous decay problem can be completely avoided by using rotational excitations in an ensemble of ultracold polar molecules trapped in an optical lattice. The rotational states are labeled by the quantum number of the rotational angular momentum \mathbf{J} and the projection M_J of \mathbf{J} on the space-fixed quantization axis Z . We choose the rotational ground state $|J = 0, M_J = 0\rangle$ as $|g\rangle$ and the rotational excited state $|J = 1, M_J = 0\rangle$ as $|e\rangle$. The state $|J = 1, M_J = 0\rangle$ is degenerate with the states $|J = 1, M_J = \pm 1\rangle$. This degeneracy can be lifted by

applying a homogeneous DC electric field, making the $|g\rangle$ and $|e\rangle$ states an isolated two-level system. The molecules in different lattice sites are coupled by the dipole-dipole interaction $V_{dd}(n-m)$. The magnitude of the coupling constant $\alpha(n-m) = \langle e_n, g_m | V_{dd}(n-m) | g_n, e_m \rangle$ between molecules with the dipole moment 1 Debye separated by 500 nm is on the order of 1 kHz [20]. Due to the low value of ΔE_{e-g} , the spontaneous emission time of rotationally excited molecules exceeds 1 second.

For molecules on an optical lattice, one can implement the phase kicks by modifying the molecular energy levels with pulsed AC or DC electric fields. The rotational energy levels for ${}^1\Sigma$ molecules in a combination of weak AC and DC electric fields are given by [80]

$$E_{J,M_J} \approx BJ(J+1) + \frac{\mu^2 \mathcal{E}_{DC}^2}{2B} G(J, M_J) - \frac{\alpha_\perp \mathcal{E}_{AC}^2}{4} + \frac{(\alpha_{||} - \alpha_\perp) \mathcal{E}_{AC}^2}{4} F(J, M_J) \quad (4.44)$$

where B is the rotational constant, and $G(J, M_J)$ is given by

$$G(J, M_J) = \frac{J^2 - |M_J|^2}{J(2J+1)(2J-1)} - \frac{(J+1)^2 - |M_J|^2}{(J+1)(2J+1)(2J+3)}, \quad (4.45)$$

and $F(J, M_J)$ is given by

$$F(J, M_J) = -\frac{1}{2} \left[1 - \frac{(2|M_J|-1)(2|M_J|+1)}{(2J-1)(2J+3)} \right], \quad (4.46)$$

and \mathcal{E}_{AC} is the envelope of the quickly oscillating AC field, $\alpha_{||}$ and α_\perp are the parallel and perpendicular polarizabilities and μ is the permanent dipole moment of the molecule.

The momentum shift of the exciton wave packets can be achieved by applying a time-varying DC electric field $\mathcal{E}(t) = \mathcal{E}_* + \mathcal{E}(n) \sin^2(\pi t/T)$, where $\mathcal{E}(n)$ is linear with respect to n . Assuming that $\mathcal{E}(n) = (n - n_0)A$ and $\mathcal{E}(n) \ll \mathcal{E}_*$, and using equation (4.12) and equation (4.44), we obtain the phase accumulated by the

excited state $|1,0\rangle_n$ at site n with respect to the ground state:

$$\begin{aligned}
\phi(n) &= -\frac{1}{\hbar} \int_0^T [E_n^e(t) - E_n^g(t)] dt \\
&= -\frac{1}{\hbar} \int_0^T \frac{\mu^2 \mathcal{E}_{DC}^2}{2B} [G(1,0) - G(0,0)] dt \\
&= -\frac{4\mu^2}{15\hbar B} \int_0^T [\mathcal{E}_* + A \sin^2(\pi t/T)(n-n_0)^2] dt \\
&\approx -\frac{4\mu^2}{15\hbar B} \int_0^T [\mathcal{E}_*^2 + 2\mathcal{E}_* A \sin^2(\pi t/T)(n-n_0)] dt \\
&= -\frac{4\mu^2}{15\hbar B} \int_0^T [\mathcal{E}_*^2 T + T \mathcal{E}_* A (n-n_0)] . \tag{4.47}
\end{aligned}$$

In the above equation, the term that is linear with lattice index n will give the phase kick

$$\delta = -4A\mathcal{E}_*\mu^2 T / 15\hbar Ba . \tag{4.48}$$

We have confirmed this result by a numerical computation showing that for LiCs molecules in an electric field of $\mathcal{E}_* = 1$ kV/cm, an electric field pulse with $A = 7.434 \times 10^{-4}$ kV/cm and $T = 1$ μ s results in a kick of $\delta = -\pi/2a$, bringing an excitonic wave packet from the $k = 0$ region to the middle of the dispersion zone.

An alternative strategy is to use a pulse of an off-resonance laser field, as for atoms. The phase transformations can be induced by a Gaussian laser beam with the intensity profile

$$I(r,z) = \frac{I_0}{1 + \frac{z^2}{z_R^2}} \exp \left[-\frac{2r^2}{w_0^2 \left(1 + \frac{z^2}{z_R^2} \right)} \right] , \tag{4.49}$$

where I_0 is the light intensity at the beam center, r is the radial distance from the center axis of the beam, z is the axial distance from the beam center, $z_R = \pi w_0^2 / \lambda$ is Rayleigh range, w_0 is the beam waist and λ is the wavelength. In order for the dressed rotational states $|J, M_J\rangle$ have a definite space quantization axis, the laser is linearly polarized in the direction of the DC field. As shown in figure (4.6), we put the 1D molecular array along the z-axis of the beam so that $r = 0$ for all the molecules. Based on Eq. (4.49), we can write out the intensity for each molecule

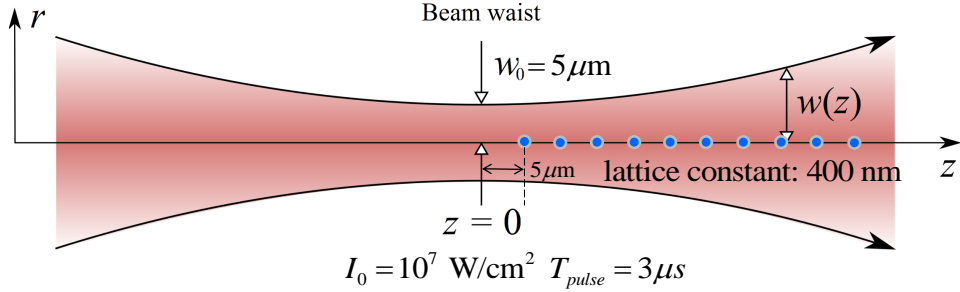


Figure 4.6: The experimental setup for the calculation corresponding to figure (4.2). A 1D array of LiCs molecules trapped on an optical lattice with lattice constant $a = 400 \text{ nm}$ is subjected to a homogeneous DC field of 1 kV/cm directed perpendicular to the intermolecular axis. The kicking potential leading to the phase transformation presented by equation (4.54) can be provided by a $\lambda = 1064 \text{ nm}$ Gaussian laser beam that is linearly polarized in the direction of the DC field, with the propagation direction along the array axis, focused to a radius of $5 \mu\text{m}$, with the intensity at the focus equal to 10^7 W/cm^2 . The laser pulse is on between 0 and $3 \mu\text{s}$.

of the array:

$$I(n) = \frac{I_0}{1 + \frac{(z_0+na)^2}{z_R^2}} , \quad (4.50)$$

where n is the molecule index and z_0 is the distance between the center of the wave packet and the beam center. Suppose the width of the wave packet in coordinate space is about S_x (positive integer) times of the lattice constant a and we want to use the laser gaussian beam to give the wave packet a momentum kick. For convenience, the molecule at the center of the wave packet is indexed as 0, the molecules to the left are indexed by negative integers and the molecules to the right by positive integers. In practices, we can assume that the wave packet is confined within the range $[-S_x a, S_x a]$ for a time period much shorter than $1/\alpha$. To make the intensity $I(n)$ varies linearly with n , the natural way is to put the molecular array far away from the beam center such that $na \ll z_0$. In this case, we can Taylor

expand the intensity function as follows:

$$I(n) = I_0 \left\{ \frac{z_R^2}{z_0^2 + z_R^2} - \frac{2an z_0 z_R^2}{(z_0^2 + z_R^2)^2} + \frac{a^2 n^2 z_R^2 (3z_0^2 - z_R^2)}{(z_0^2 + z_R^2)^3} + O(n^3) \right\}, \quad (4.51)$$

and ignore the terms that are higher than linear order in n . However, when z_0 is large enough such that omission of higher terms is justified, the slope of the approximately linear intensity function $I(n)$ is small which means that more powerful laser is needed to give the momentum kick. This is undesirable for experimentalists. Instead, we find that one doesn't need to put the molecular array very far away from the beam center to obtain a linear intensity profile. The trick is let $z_0 = z_R/\sqrt{3}$ so that some higher terms (like the second-order term) in equation (4.51) will vanish. Rather than working with the Taylor series, we find it is more convenient to work with the original intensity function directly. Substituting $z_0 = z_R/\sqrt{3}$ and assuming $1 - \frac{\sqrt{3}}{2} \frac{an}{z_R}$, we have

$$\begin{aligned} I(n) &= \frac{I_0}{1 + \frac{(z_0+na)^2}{z_R^2}} = \frac{I_0 \left(1 - \frac{\sqrt{3}}{2} \frac{an}{z_R} \right)}{\left[1 + \left(\frac{1}{\sqrt{3}} + \frac{na}{z_R} \right)^2 \right] \left(1 - \frac{\sqrt{3}}{2} \frac{an}{z_R} \right)} \\ &= \frac{1 - \frac{\sqrt{3}}{2} \frac{an}{z_R}}{\frac{4}{3} \left[1 - \frac{3\sqrt{3}}{8} \left(\frac{an}{z_R} \right)^3 \right]}. \end{aligned} \quad (4.52)$$

For $I(n)$ to be linear within the range $[-S_x, S_x]$, the second term in the square bracket in equation (4.52) should be much less than 1. This leads to a restriction on the width of the wave packet:

$$S_x a \lesssim 0.5 z_R \quad (4.53)$$

Therefore if the two conditions $z_0 = z_R/\sqrt{3}$ and $S_x a \lesssim 0.5 z_R$ are satisfied, we can implement the momentum kick for the wave packet. Using equation (4.11), equation (4.44) and equation (4.52), we carry on a similar calculation similar to that in

equation (4.47) and estimate the momentum kick by such a pulse as

$$\delta = -\sqrt{3}TI_0(\alpha_{\parallel} - \alpha_{\perp})/80z_R . \quad (4.54)$$

To demonstrate the feasibility of momentum kick by laser pulse, we have run a simulation with $z_0 = 45 \mu\text{m}$ and $z_R = 73.8 \mu\text{m}$ and find the results (shown in Figure 4.2.) only deviate about 7% from the analytical estimation.

4.4.3 Focusing in system of ultracold molecules

The Gaussian intensity profile (4.49) can also be used to implement the quadratic phase transformations needed for focusing of collective excitations. To achieve this, a molecular array (1D or 2D) must be arranged in the $z = 0$ plane of the Gaussian beam. As mentioned in Section 4.4.2, an extra DC field is also needed here to lift the degeneracy of rotational states and to avoid mixing of different exciton bands. In addition, the laser is linearly polarized along the direction of the DC field in order for the system to have a well-defined space quantization axis.

First, we consider the case of 1D molecular array. The wave packet that we want to focus is a Gaussian wave packet with the width σ_x . We put the beam center at the center of the wave packet and define the x -axis of the $z = 0$ plane to be along the intermolecular axis (see figure (4.7) (a)). Then the molecules in the lattice can be indexed by theirs x coordinates $n_x a$. If the dimension of the wave packet is smaller than one third of the beam waist, we can approximate the gaussian intensity profile in equation (4.49) by

$$I(x, y = 0, z = 0) \approx I_0 \left(1 - \frac{2n_x^2 a^2}{w_0^2} \right) , \quad (4.55)$$

with an accuracy of 90%. Equation (4.55) presents a concave quadratic intensity profile which can be used to focus a wave packet with attractive coupling ($\alpha < 0$) (see Section 4.3.2). This indicates that we need to make the coupling α between molecules negative. A calculation of the dipole-dipole interaction between molecules in DC field shows that α is proportional to $(1/3 - \cos^2 \theta)$ where θ is the angle between the DC field and the intermolecular axis (or x -axis). Therefore, we can orientate the DC field to a proper direction to achieve the attractive

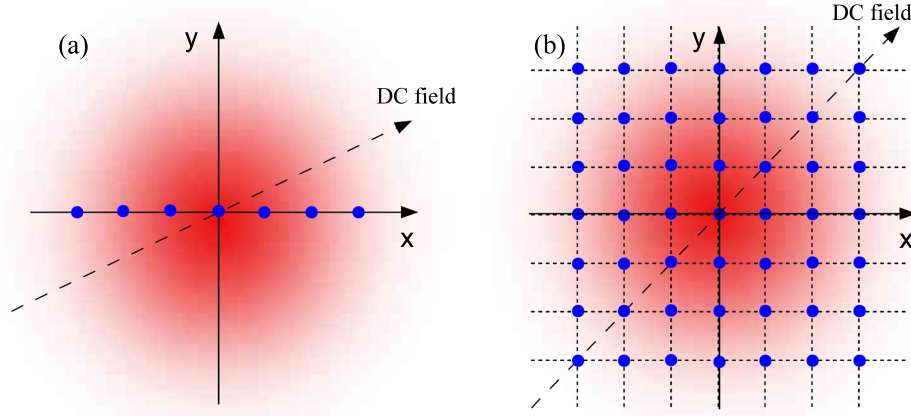


Figure 4.7: An illustration to show the orientations of 1D and 2D molecular arrays inside the gaussian beam. (a): the 1D lattice lies along the x -axis of the $z = 0$ plane and the DC field is at some angle with the x -axis such that the coupling α between molecules is negative. (b): the 2D square lattice is at the the center of the $z = 0$ plane and the DC field is at 45° degree with the x -axis. In both cases, the laser is linearly polarized along the direction of the DC field.

coupling between molecules. As shown in figure (4.8) (a), θ must be in the range $[0, 57.3^\circ]$ to ensure the attractive coupling.

From previous discussions in Section 4.3.2, we know that good focusing effect occurs when the quadratic phase profile applied is $\Phi(n) = \Phi_0 n^2$ with $\Phi_0 = -a/2\sigma_x$ if $\alpha < 0$. So we will use this particular value of Φ_0 to estimate the power of the laser that are needed for the focusing. Specifically, we are using a laser pulse with a short ramp-up and ramp-down time T_s and a long steady time T_l :

$$I_0(t) = \begin{cases} I_m \sin^2 \left(\frac{\pi \tau}{2T_s} \right) & (0 \leq \tau < T_s) \\ I_m & (T_s \leq \tau \leq T_s + T_l) \\ I_m \sin^2 \left[\frac{\pi(\tau - T_s - T_l)}{2T_s} + \frac{\pi}{2} \right] & (T_s + T_l < \tau \leq 2T_s + T_l) \end{cases} \quad (4.56)$$

Based on equation (4.12) and equation (4.44), the phase acquired by a molecule at

site n_x with respect to the molecule at the beam center is given by

$$\begin{aligned}\phi(n_x) &= -\frac{2(\alpha_{||} - \alpha_{\perp})I_0 n_x^2 a^2}{15w_0^2} \left(\frac{T_s}{2} + T_l \right) \\ &\approx -\frac{2(\alpha_{||} - \alpha_{\perp})I_0 n_x^2 a^2 T_l}{15w_0^2},\end{aligned}\quad (4.57)$$

where $T_l \ll T_s$ is assumed in the last step. Equating $\phi(n_x)$ with the optimal phase profile $\Phi(n_x) = \Phi_0 n_x^2 = -a/2\sigma_x n_x^2$, and assuming the laser power is P and the initial width of the wave packet is $\sigma_x = Sa$, we can estimate the duration of the laser pulse to be

$$T_l \approx \frac{15\pi w_0^4}{4Sa^2(\alpha_{||} - \alpha_{\perp})P}. \quad (4.58)$$

For LiCs molecules trapped on a optical lattice with the lattice constant $a = 400\text{nm}$, if the initial width of the wave packet is about 100 lattice sites and the beam waist is 3 times larger than that width, the pulse duration calculated from Eq. (4.58) is about $335\ \mu\text{s}$ for a laser Gaussian beam with the power of 10 W. To ensure the focusing works as expected, the wave packet should be exposed to the laser field for long enough time to accumulate the required phases, so the focusing time T_f for the wave packet to become most focused must be longer than the duration of the laser pulse. This is not a problem considering that T_f is inversely proportional to the coupling strength α :

$$T_f \approx \frac{1}{4\alpha\Phi_0}, \quad (4.59)$$

and α can be tuned to be very small through changing the magnitude of the DC field [20] by only a few kV/cm or by increasing the angle θ . For instance, when the DC field is about 1 kV/cm and orientate along the intermolecular axis, the focusing time

$$T_f \approx \frac{1}{4\alpha\Phi_0} = \frac{1}{4(-20\text{ kHz})(-\frac{1}{200})} = 2.5\text{ ms} \quad (4.60)$$

is much longer than the duration of the laser pulse, leaving enough time for the accumulation of the phases.

Second, we consider the case of 2D molecular array. The situation is similar to the 1D case except that anisotropy of the dipole-dipole interaction comes

into play. Instead of only considering the coupling between molecules in the x -axis, we also have to consider the dipole-dipole interactions along y -axis and along other directions between x -axis and y -axis. This is because the DC field will be at different angles with the different chains of molecules, giving rises to different dipole-dipole interactions in different directions. For simplicity, we use the nearest neighbor approximation here and only consider the dipole-dipole interactions along the x -axis and y -axis. Assuming the dimension of the wave packet is smaller than one third of the beam waist, we can approximate the gaussian intensity profile in equation (4.49) by

$$I(x, y = 0, z = 0) \approx I_0 \left[1 - \frac{2(n_x^2 + n_y^2)a^2}{w_0^2} \right]. \quad (4.61)$$

Similar to equation (4.55) in the 1D case, equation (4.61) is also a concave quadratic intensity profile which can be used to focus a wave packet with attractive coupling. But the difference here is that we need to make sure both the couplings along x -axis and y -axis are negative. Since the interaction along x -axis and y -axis are independent of each other, the dependence of α on θ in the 1D case can be applied for the 2D case. Therefore, in order for the focusing scheme to work, the angle θ_x between the DC field and the x -axis and the angle θ_y between the DC field and the y -axis should be in the range $[0, 57.3^\circ]$. As an example, figure (4.7) shows one configuration ($\theta_x = \theta_y = 45^\circ$) which will ensure attractive coupling along both axes.

4.5 Control of energy transfer in dipolar systems

Dipolar interactions play a central role in the study of long-range interaction effects using ultracold systems [81]. While, in general, the coupling constant α in equation (4.1) can be determined by a variety of interactions, the dominant contribution to α for atoms and molecules on an optical lattice is determined by the matrix elements of the dipole - dipole interaction. It is therefore particularly relevant to discuss the specifics of energy transfer in systems with dipolar interactions.

4.5.1 The effect of long-range interaction

The dipolar interactions are long-range and anisotropic. This long-range character manifests itself in the modification of the exciton dispersion (4.4). While equation (4.4) is valid for a system with nearest neighbour couplings only, higher-order couplings in the case of $\alpha(n-m) \propto 1/|n-m|^3$ modify the exciton dispersion leading to a cosine-like, but non-analytic dispersion relation, both in 1D and 2D.

To see why the dispersion curve is non-analytic, we start from the expression for $E(k)$:

$$\begin{aligned} E(k) &= \Delta E_{eg} + \sum_n \alpha(n) e^{-ikan} \\ &= \Delta E_{eg} + \sum_n \frac{\alpha}{|n|^3} e^{-ikan}, \end{aligned} \quad (4.62)$$

where n is the difference of two molecular indexes and the summation goes from $-\infty$ to -1 and from 1 to ∞ for a crystal of infinite size. Restricting n to be a positive integer, equation (4.62) can be written as

$$E(k) = \Delta E_{eg} + \sum_{n=1}^{\infty} \frac{2\alpha \cos(kan)}{n^3}. \quad (4.63)$$

Then the first derivative of the dispersion curve is given by

$$\frac{dE(k)}{d(ka)} = - \sum_{n=1}^{\infty} \frac{2\alpha \sin(kan)}{n^2}, \quad (4.64)$$

and the second derivative of the dispersion curve is given by

$$\frac{d^2E(k)}{d(ka)^2} = - \sum_{n=1}^{\infty} \frac{2\alpha \cos(kan)}{n}. \quad (4.65)$$

The series in equation (4.63) and equation (4.64) converge with respect to n , but the series in equation (4.65) doesn't. For example, when $ka = 0$ or π , the series in equation (4.65) becomes the harmonic series and it diverges with respect to n .

Therefore, the dispersion curve cannot be taylor expanded as follows:

$$E(k) = E(k_0) + \frac{dE(k)}{dk} \Big|_{k_0} (k - k_0) + \frac{d^2E(k)}{dk^2} \Big|_{k_0} (k - k_0)^2 + \dots \quad (4.66)$$

Conventionally, we only consider the interactions between nearest neighbors and take $n = 1$ in equation (4.63), this might be justified if only a rough estimate of the dispersion curve is wanted because the series in equation (4.63) converges very fast with respect to the distance n . Given the consideration on the convergence, more neighbors should be included in the summation to calculate the properties dependent on the first derivative of the dispersion curve, and all neighbors are probably needed to calculate properties determined by the second derivative.

To investigate the effect of this nonanalyticity in dispersion curve, we have performed a series of calculations with the long-range couplings neglected after a certain lattice site separation $n - m$ for the 1D system. The results become converged (to within 0.2 %) when each molecule is directly coupled with 20 nearest molecules. While the calculations with only the nearest neighbor couplings are in good agreement with the analytical predictions given by equation (4.31) and equation (4.32), the full calculations reveal that long-range couplings somewhat decrease the focusing efficiency. The long-range couplings also decrease the focusing time, by up to a factor of 2. The dynamics of collective excitations leads to interference oscillation patterns clearly visible in panels a and c of Figure 4.4. These oscillations are much less pronounced when all but nearest neighbor couplings are omitted. Given that the analytical derivation in Section 4.3 are based on possible invalid taylor expansion of dispersion curve (equation (4.66)), the numerical results of figure (4.4) and figure (4.5) are particularly important because they demonstrate that the phase transformations introduced in the present work are effective for systems with dipolar interactions.

4.5.2 Anisotropy of dipolar interaction

The anisotropy of the dipolar interactions can be exploited for controlling energy transfer in dipolar systems by varying the *orientation* of a dressing external DC electric field. For example, for polar molecules on an optical lattice, the matrix

elements $\alpha(n-m) = \langle e_n, g_m | V_{dd}(n-m) | g_n, e_m \rangle$ depend not only on the choice of the states $|g\rangle$ and $|e\rangle$, but also on the magnitude and orientation of an external dc electric field [20, 50]. Since the value of α determines the exciton dispersion (4.4), the exciton properties can be controlled by varying the angle θ between the intermolecular axis and the applied DC field. This is illustrated in figure (4.8).

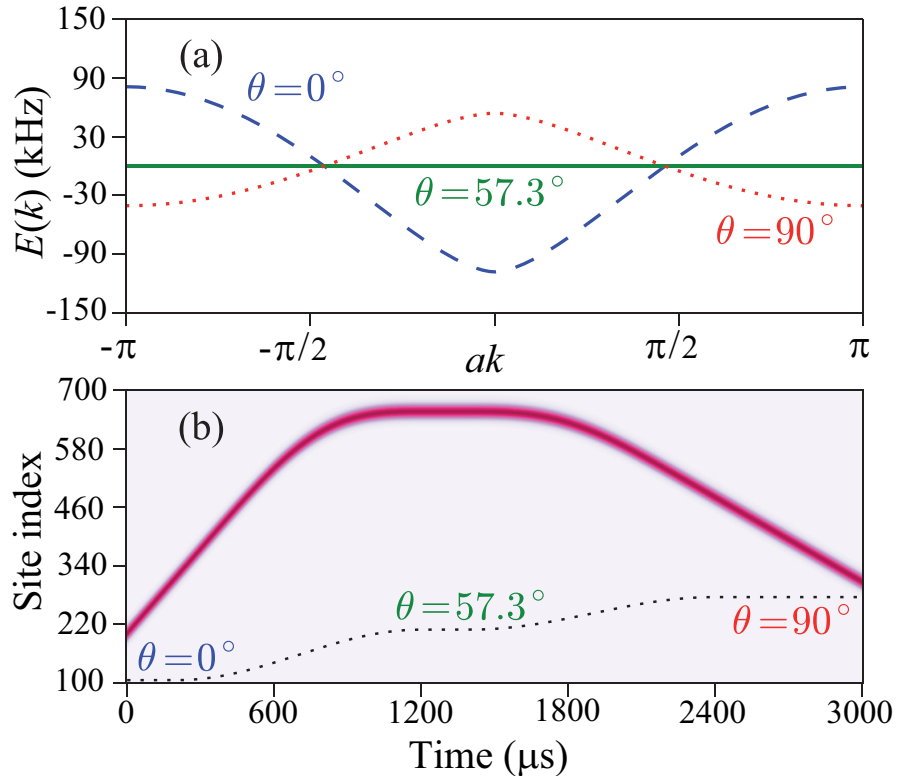


Figure 4.8: Control of excitation transfer in a 1D many-body system with dipolar interactions by varying the direction of an external electric field. Panel (a): Exciton dispersion curves for a 1D ensemble of diatomic molecules on an optical lattice for different angles θ between the direction of the external DC electric field and the axis of the molecular array. In 1D, the coupling $\alpha \propto (1/3 - \cos^2 \theta)$. Panel (b): Propagation of a wave packet centered at $ak = -\pi/3$ controlled by tuning the electric field direction. Thin dotted line depicts the corresponding angle variations with time. The brightness of color corresponds to the probability of the excitation.

The calculations presented in Figure 4.8 are for a 1D array of LiCs molecules in a lattice with $a = 400$ nm. As before, $|g\rangle$ is the absolute ground state of the molecule and $|e\rangle$ is the rotationally excited state that adiabatically correlates with the rotational state $|J = 1, M_J = 0\rangle$ in the limit of vanishing electric field. The upper panel of Figure 4 shows that the angle θ between the electric field vector and the molecular array axis determines the sign and magnitude of α , and therefore the shape of the dispersion curve. This enables control over the sign and magnitude of the group velocity of an excitonic wave packet containing contributions with $k \neq 0$. Dynamically tuning θ , one can propagate a localized excitation to different parts of the lattice, as shown in Figure 4.8 (b).

In a 2D lattice, the intermolecular interactions depend on an additional azimuthal angle ϕ that describes the rotation of the electric field axis around the axis perpendicular to the lattice. The numerical calculations presented in Figure 4.9 show that the energy flow in two dimensions can be controlled by varying both θ and ϕ . In addition to the phase transformation discussed earlier, this allows for a dynamical energy transfer in quantum many-body systems with anisotropic interparticle interactions.

4.5.3 Computation details

In this subsection, we show how to carry on the calculations presented in Section 4.5.2. We first evaluate dipole-dipole interaction in the 1D and 2D molecular arrays, then discuss how to form the Hamiltonian matrix in an efficient way, and finally present some approximations that can reduce the computation cost significantly.

As discussed in Section 2.2, the dipole-dipole operator for molecule A and molecule B separated by \mathbf{R} in optical lattices is given by

$$\hat{V}_{dd}(R) = -2\sqrt{\frac{6\pi}{5}} \left(\frac{1}{R}\right)^3 \sum_q (-1)^q Y_{2,-q}(\theta_R, \phi_R) \left[d_A^{(1)} \otimes d_B^{(1)} \right]_q^{(2)} \quad (4.67)$$

where the angles (θ_R, ϕ_R) describe the orientation of the vector \mathbf{R} in the coordinate system whose z -axis coincides with the direction of DC field and $Y_{2,-q}$ are these

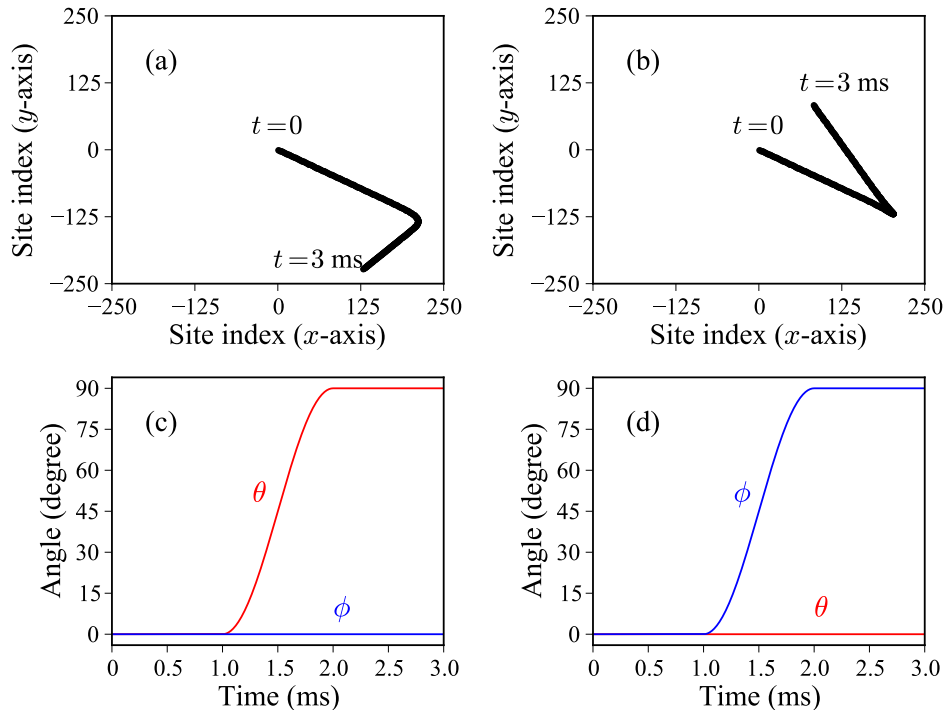


Figure 4.9: Control of excitation transfer in a 2D many-body system with dipolar interactions by varying the direction of an external electric field. Panels (a) and (b) show the trajectories of the center of an exciton wave packet in a 2D lattice during the time from 0 to 3 ms; Panels (c) and (d) represent the changing of the dressing DC field orientation (θ, ϕ) associated with (a) and (b) respectively. The initial wave packet is a 2D Gaussian distribution centered around $ak_x = ak_y = \pi/2$ and has a width of ~ 60 lattice sites in coordinate space. The magnitude of the DC field is fixed to 6 kV/cm while its direction is changing. The calculations are done for a 2D array of LiCs molecules in a lattice with $a = 400$ nm.

spherical harmonics:

$$\begin{aligned}
Y_{2,-2} &= \frac{1}{4} \sqrt{\frac{15}{2\pi}} \sin^2 \theta_R e^{-2i\phi_R} \\
Y_{2,-1} &= \frac{1}{2} \sqrt{\frac{15}{2\pi}} \sin \theta_R \cos \theta_R e^{-i\phi_R} \\
Y_{2,0} &= \frac{1}{4} \sqrt{\frac{5}{\pi}} (3 \cos^2 \theta_R - 1) \\
Y_{2,1} &= -\frac{1}{2} \sqrt{\frac{15}{2\pi}} \sin \theta_R \cos \theta_R e^{i\phi_R} \\
Y_{2,2} &= \frac{1}{4} \sqrt{\frac{15}{2\pi}} \sin^2 \theta_R e^{2i\phi_R}
\end{aligned} \tag{4.68}$$

To calculate the dipole-dipole interaction, we evaluate the matrix element of the dipole-dipole operator in the basis of bare rotational states:

$$\begin{aligned}
&\langle N_A, M_A | \langle N_B, M_B | \hat{V}_{dd}(R) | N'_A, M'_A \rangle | N'_B, M'_B \rangle \\
&= -\frac{F}{2R^3} \left\{ 3 \sin^2 \theta_R e^{-2i\phi_R} D_-^A D_-^B - 6 \sin \theta_R \cos \theta_R e^{-i\phi_R} [D_0^A D_-^B + D_-^A D_0^B] \right. \\
&\quad + 3 \sin^2 \theta_R e^{2i\phi_R} D_+^A D_+^B + 6 \sin \theta_R \cos \theta_R e^{i\phi_R} [D_0^A D_+^B + D_+^A D_0^B] \\
&\quad \left. + \sqrt{6} (3 \cos^2 \theta_R - 1) [D_+^A D_-^B + D_-^A D_+^B + D_0^A D_0^B] \right\}, \tag{4.69}
\end{aligned}$$

where F and D_S^X are given in Section 2.2. In D_S^X of equation (4.69), the superscript X ($= A$ or B) denotes molecule A or B , and the subscript S ($= +$ or $-$ or 0) indicates D_S^X is nonzero only if the projection of the rotational quantum number of molecule X changes in a certain way: “+” means $M_X = M'_X + 1$; “-” means $M_X = M'_X - 1$; 0 means $M_X = M'_X$. As depicted in figure (4.10) (a), rotating the coordinate system around its z -axis does not change the physical properties of the molecular array as the relative orientation of the DC field with respect to the intermolecular axis remains the same. Therefore we have the freedom to choose $\phi_R = 0$ in equation (4.69) for the 1D molecular array. However, a 2D molecular array has many intermolecular axes that are at different angles (θ_R, ϕ_R) with the external field, which means one cannot make all ϕ_R zero by rotating the coordinate system while keeping the relative orientation of the external field with respect

to the molecular array. So in general we have to consider both θ_R and ϕ_R when calculating the dipole-dipole interaction in a 2D molecular array.

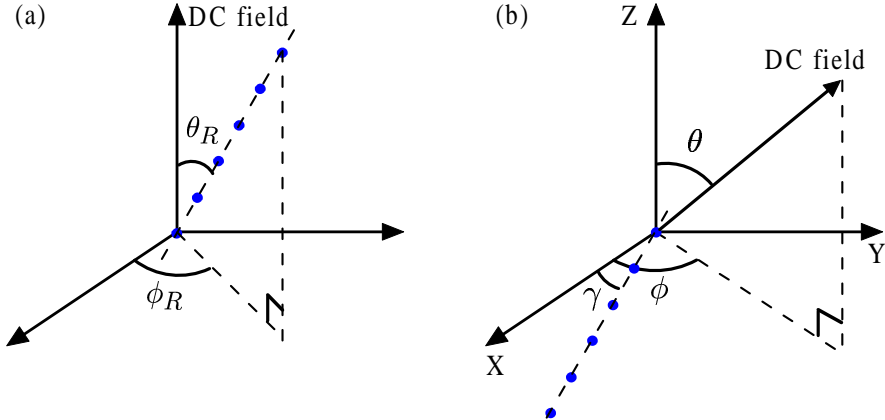


Figure 4.10: The orientations of the DC field and molecular arrays in the coordinate systems. (a): The DC field is along the z -axis and the 1D molecular array is in the direction represented by θ_R and ϕ_R . (b): The 2D molecular array is on the XY plane and the orientation of DC field is represented by (θ, ϕ) . For clarity, we have only drawn the molecules (as blue dots) along a particular axis which is at angle γ with the X -axis. It is to be understood that there are also other intermolecular axes which are at different angles with the X -axis. Note part (a) and part (b) have different coordinate systems and the meaning of (θ_R, ϕ_R) is different from that of (θ, ϕ) . In fact, the angle θ_R between the DC field and the molecular array in (b) is related to θ and ϕ by $\cos \theta_R = \cos \theta \cos(\phi - \gamma)$.

Keeping track of both angles θ_R and ϕ_R is complicated. Fortunately, we can get rid of the dependence of ϕ_R in equation (4.69) by choosing to deal with only certain rotational states. In a DC field or a linearly polarized laser field, the dressed rotational states $|\tilde{N}, |M|\rangle$ of the system is a linear combination of the bare rotational states with the same projection along the direction of DC field or along the direction of laser polarization, that is,

$$|\tilde{N}, |M|\rangle = \sum_N C_{N,M} |N, M\rangle . \quad (4.70)$$

Note that the coefficients $C_{N,M}$ only depend on the magnitude of the external field and have nothing to do with the angles θ_R and ϕ_R . Because those dressed states with different projections $|M|$ have different energies, we can choose to work with the states with a particular value of $|M|$ by tuning the excitation energy to just match the corresponding energy levels. In the current study, $|M|$ is chosen to be zero, therefore only the bare rotational states with $M_X = 0$ are involved, then only the term associated with $D_0^A D_0^B$ in equation (4.69) is nonzero, and we have

$$\langle N_A, 0 | \langle N_B, 0 | \hat{V}_{dd}(R) | N'_A, 0 \rangle | N'_B, 0 \rangle = -\frac{\sqrt{6}F}{2R^3} (3 \cos^2 \theta_R - 1) D_0^A D_0^B . \quad (4.71)$$

Then the dipole-dipole interaction between two dressed state with $|M| = 0$ can be expressed as a linear combinations of equation (4.71):

$$\begin{aligned} & \langle \tilde{N}_A, 0 | \langle \tilde{N}_B, 0 | \hat{V}_{dd}(R) | \tilde{N}'_A, 0 \rangle | \tilde{N}'_B, 0 \rangle \\ &= \sum_{N_A} \sum_{N_B} \sum_{N'_A} \sum_{N'_B} C_{N_A, 0}^* C_{N_B, 0}^* C_{N'_A, 0} C_{N'_B, 0} \langle N_A, 0 | \langle N_B, 0 | \hat{V}_{dd}(R) | N'_A, 0 \rangle | N'_B, 0 \rangle . \end{aligned} \quad (4.72)$$

Equation (4.71) and equation (4.72) show that we only need to consider the angle θ_R between the intermolecular axis and the external field if only the dressed rotational states with $|M| = 0$ are involved. This is valid for both 1D and 2D cases.

Since a 1D molecular array can be treated as a limiting case of a 2D molecular array with only a single intermolecular axis, we focus on the discussion of the 2D case. As described by figure (4.10), we suppose the 2D molecular array is on the XY plane, and the orientation of the external field is presented by (θ, ϕ) . For any two molecules in the intermolecular axis that are at angle γ with the X -axis, $\cos^2 \theta_R$ in can be calculated as

$$\begin{aligned} \cos^2 \theta_R &= \left[\cos \left(\frac{\pi}{2} - \theta \right) \cos(\phi - \gamma) \right]^2 \\ &= \sin^2 \theta (\cos \phi \cos \gamma + \sin \phi \sin \gamma)^2 . \end{aligned} \quad (4.73)$$

Therefore the dipole-dipole interaction between two molecules can be calculated from equation (4.71) and equation (4.72) provided that the angle between the in-

termolecular axis and the X -axis is known.

Once the dipole-dipole interaction is known, we can form the Hamiltonian matrix by expanding the Hamiltonian in the basis of individual sites. Suppose the 2D molecular array is a square lattice with $N \times N$ sites and the coordinate system is orientated such that its X -axis and Y -axis coincide with the bottom and left edge of the 2D lattice respectively, then the position of the molecule in the array can be represented by its coordinates (x, y) . Without the loss of generality, we consider only the case where the external field is orientated such that $0 \leq \theta \leq 90^\circ$ and $0 \leq \phi \leq 90^\circ$, and give the indexes $0, 1, 2, \dots, N^2 - 1$ to every molecule in the 2D array, starting from the bottom to the top of the array and from left to right in each row. Based on equation (4.71) and equation (4.72), the matrix element $H_{i,j}$ corresponding to two sites i and j is given by

$$\begin{aligned} H_{i,j} &= \langle \tilde{0}, 0 | i \langle \tilde{1}, 0 | j H_0 + \hat{V}_{dd} | \tilde{1}, 0 \rangle_i | \tilde{0}, 0 \rangle_j \\ &= \sum_{N_A} \sum_{N_B} \sum_{N'_A} \sum_{N'_B} -\frac{\sqrt{6}F}{2R_{i,j}^3} (3\cos^2 \theta_R(i, j) - 1) D_0^A D_0^B C_{N_A, 0}^* C_{N_B, 0}^* C_{N'_A, 0} C_{N'_B, 0} , \end{aligned} \quad (4.74)$$

where $R_{i,j}$ is the distance between molecule i and j , and $\theta_R(i, j)$ is angle between the external field and the intermolecular axis. Assuming the unit length of the coordinate system is the lattice constant of the 2D array, then the distance between the two site i and j can be calculated from their coordinates

$$R_{i,j} = a \sqrt{(x_i - x_j)^2 + (y_i - y_j)^2}, \quad (4.75)$$

where

$$\begin{aligned} x_i &= i \% N \\ y_i &= i / N . \end{aligned} \quad (4.76)$$

Since the angle γ between the external field and the intermolecular axis connecting

from molecule i to molecule j is given by

$$\gamma(i, j) = \arccos \left[\frac{x_j - y_i}{\sqrt{(x_i - x_j)^2 + (y_i - y_j)^2}} \right], \quad (4.77)$$

the value of $\cos^2 \theta_R(i, j)$ in equation (4.74) can be calculated from equation (4.73).

With the Hamiltonian matrix H , we can now run the simulations presented in Section 4.5.2. The essential problem is to solve the time-dependent Schrödinger equation

$$\dot{\Psi}(t) = \frac{1}{i\hbar} H(t) \Psi(t). \quad (4.78)$$

Solving the above differential equations involves the computation of the Hamiltonian matrix at many different time points. To make the simulation as fast as possible, we now explore how to evaluate $H(t)$ efficiently. In the calculations, we change the direction of the DC field adiabatically with respect to the time scale of excitation hopping while keeping the magnitude of the field, therefore the coefficients $C_{N_A,0}$, $C_{N_B,0}$, $C_{N'_A,0}$, and $C_{N'_B,0}$ in equation (4.74) will remain the same and the time dependence of the Hamiltonian matrix is solely due to the time dependence of $\theta_R(t)$. Based on this observation, we can separate the Hamiltonian matrix into two parts:

$$H(t) = H_1(\theta(t), \phi(t)) * H_2, \quad (4.79)$$

where “*” means element-wise multiplication, H_1 is the time-dependent part that needs to be updated whenever $\theta(t)$ and $\phi(t)$ change, and H_2 is the time-independent part that can be computed once and be saved into memory for later retrieve. It is easy to derive from equation (4.74) the expression of H_2 :

$$H_2 = \sum_{N_A} \sum_{N_B} \sum_{N'_A} \sum_{N'_B} -\frac{\sqrt{6}F}{2R_{i,j}^3} D_0^A D_0^B C_{N_A,0}^* C_{N_B,0}^* C_{N'_A,0} C_{N'_B,0}. \quad (4.80)$$

Because of the angle γ in equation (4.73) is only dependent on positions of the lattice sites, we can further separate the evaluation of H_1 into different parts for

the purpose of computing efficiency. The expression of H_1 is given by

$$H_1(\theta(t), \phi(t)) = 3 \cos^2[\theta(t)] * \left\{ \cos[\phi(t)] * K^{\cos} + \sin[\phi(t)] * K^{\sin} \right\} ** 2 - 1 \quad (4.81)$$

where “**2” means element-wise square, and K^{\cos} is a matrix whose elements is given by

$$K_{i,j}^{\cos} = \cos(\gamma(i, j)) , \quad (4.82)$$

and K^{\sin} is a matrix whose elements is given by

$$K_{i,j}^{\sin} = \sin(\gamma(i, j)) . \quad (4.83)$$

Since K^{\cos} and K^{\sin} are independent of time, we compute them once and save them into memory for later usage. In summary, the efficient computation of $H(t)$ is carried on in three steps: 1. calculate H_2 , K^{\cos} , and K^{\sin} and save them into memory; 2. compute $\theta(t)$ and $\phi(t)$ and then use the values of K^{\cos} , and K^{\sin} in memory to calculate H_1 ; 3. use the value of H_2 in memory to compute H .

In the simulation, I have used a complex ordinary differential equation solver called “ZVODE” to solve equation (4.78). Given an initial state $\Psi(t = 0)$, the derivative $\dot{\Psi}$ of the wavefunction with respect to time, and the desired accuracy for the calculation, the solver can give the wavefunction $\Psi(t)$ at a later time t . In my experience, the ZVODE solver is not good at solving a stiff system of differential equations where the potential change is very steep. If this is the case, it is better to convert the time-dependent Schrödinger equation into a real ordinary differential equation and use the corresponding ODE solver called “DVOODE” that can handle stiff systems much better. As a reference for future students, we show below the conversion from the time-dependent Schrödinger equation to a real ordinary differential equation. The starting point is the Schrödinger equation

$$i\hbar\dot{\mathbf{C}} = \mathbf{H}\mathbf{C} , \quad (4.84)$$

where \mathbf{C} is a vector representing the state of the system. After rewriting \mathbf{C} as

$$\mathbf{C} = \mathbf{C}_{\text{real}} + i \mathbf{C}_{\text{imag}} , \quad (4.85)$$

and \mathbf{H} as

$$\mathbf{H} = \mathbf{H}_{\text{real}} + i \mathbf{H}_{\text{imag}}, \quad (4.86)$$

and collecting the real part and imaginary part separately in equation (4.84), we obtains two real equations:

$$\begin{aligned} \hbar \dot{\mathbf{C}}_{\text{real}} &= \mathbf{H}_{\text{imag}} \mathbf{C}_{\text{real}} + \mathbf{H}_{\text{real}} \mathbf{C}_{\text{imag}} \\ \hbar \dot{\mathbf{C}}_{\text{imag}} &= -\mathbf{H}_{\text{real}} \mathbf{C}_{\text{real}} + \mathbf{H}_{\text{imag}} \mathbf{C}_{\text{imag}}. \end{aligned} \quad (4.87)$$

The above two equations can be written in the block matrix form:

$$\hbar \begin{pmatrix} \dot{\mathbf{C}}_{\text{real}} \\ \dot{\mathbf{C}}_{\text{imag}} \end{pmatrix} = \begin{pmatrix} \mathbf{H}_{\text{imag}} & \mathbf{H}_{\text{real}} \\ -\mathbf{H}_{\text{real}} & \mathbf{H}_{\text{imag}} \end{pmatrix} \begin{pmatrix} \mathbf{C}_{\text{real}} \\ \mathbf{C}_{\text{imag}} \end{pmatrix}, \quad (4.88)$$

which leads to a real differential equation

$$\hbar \dot{\mathbf{C}}_{\text{new}} = \mathbf{H}_{\text{new}} \mathbf{C}_{\text{new}} \quad (4.89)$$

that is equivalent to the original Schrödinger equation.

Finally, we discuss some tricks and approximations that enable us to do the 2D simulation efficiently. For a 2D molecular array with $N \times N$ sites, since the couplings between every two sites are included, the dimension of the Hamiltonian matrix is $O(N^2 \times N^2)$. For a medium-sized 2D array with $N = 100$, the number of coupled differential equations is about 10^4 , which is close to the limit that our code can handle. As N becomes larger, the number of differential equations will increase dramatically. This pose a dilemma for us. On one side, we want to limit the size of the crystal so that the computation is fast. On the other side, as we are studying the motion of an exciton wave packet in DC field whose orientation changing adiabatically with respect to excitation hopping, the simulation time period can be long. This requires a large crystal with enough space in which the wave packet can propagate for a relatively long time without hitting the boundaries. In addition, we also want the initial size of the wave packet to be large so that it is narrow in k -space and doesn't spread very fast in coordinate space. After experimenting with different initial sizes, we found a wave packet with a width of ~ 60 lattice

sites in coordinate space is good for our purposes. If such a wave packet is used in simulation, the crystal size must be much larger than 100×100 , which is beyond the limit size that our code can handle. There are two ways to resolve the small-or-large-crystal dilemma. The most obvious choice is to use the nearest neighbor approximation so that each molecule will only interact with four molecules that are closest to it. Then the dimension of the Hamiltonian matrix scales like $O(N \times N)$, and the number of differential equations drops significantly. However, this approach fails to account for the long-range interaction and miss some characteristics of anisotropy in dipole-dipole interaction as it only consider the interactions only along the X -axis and the Y -axis. In our simulation, we take another approach by treating different regions of the crystal separately. As the dipole-dipole interaction decays fast with distance, the lattice sites that are close to the position of the wave packet are most important and should be always taken account of. So we define a computation zone as the square box that encloses the wavepacket, and define the rest of the crystal as the supplement zone. At the beginning of the simulation, we choose a large enough computation zone such that the probability to find excitation at the edges of the zone is almost zero, and compute all the interactions between any two molecules inside the zone to form the Hamiltonian matrix. All the other lattice site beyond the computation zone are ignored. In this way, the size of the Hamiltonian matrix will be determined by the smaller computation zone rather than the whole lattice and the most important part of the long-range interaction is also kept. After each time step, we find out the new position of the wave packet center and shift the computation zone such that its center coincides with the wave packet center. In the processing of the shifting, we have lost a small portion of the wave packet because the sites near the boundaries of the computation zone will be removed out of the computation zone at next time point and the excitation population at those sites will also be lost. However, if the computation zone is large enough, this should not be a problem. Therefore maintaining a small computation zone and dynamically moving it based on the movement of the wave packet allows for the calculation of the motion of a wave packet in a much bigger crystal. In figure (4.9), we have used a computation zone with the size 101×101 and the size of the whole crystal is 1001×1001 (not shown in the figure). During the simulation, we notice that the wave packet spreads in the coordinate space as time goes on, but 99%

of the wavepacket is still inside the computation zone. Because the wave packet spreads over time, our simulation will eventually break up at some point as more and more part of the wave packet will get lost at the boundaries of the computation zone.

4.6 Energy transfer in the presence of vacancies

While experiments with ultracold atoms have produced states with one atom per lattice site with 99% fidelity [73–75], the latest experiments with molecules yield lattice-site populations about 10% [76]. Multiple experiments are currently underway to trap polar molecules on an optical lattice with close to the full population of the lattice. However, lattice vacancies may be unavoidable in the best experiments. In this section, we examine the effect of vacancies on the possibility of focusing collective excitations to a desired region of the lattice by the phase transformations discussed in Section 4.3. For concreteness, we perform calculations for the system described in Section 4.4, namely a 2D array of LiCs molecules on a square optical lattice with $a = 400$ nm.

To explore the effect of vacancy-induced interactions, we performed simulations for different vacancy numbers using the same parameters for molecule-field and inter-molecular interactions as in the calculations presented in Figure 4.5 (b). For each vacancy concentration, we carried out 48 calculations with random distributions of empty lattice sites. The quadratic phase transformations are applied, as described in Section 4.3, in order to focus the collective excitation at time t_* to the molecule in the middle of the 2D array.

Vacancies disturb the translational symmetry of the system and produce an effective disorder potential that tends to localize collective excitations [82]. Because the natural time evolution of the wave packet in a disorder potential may lead to enhancement of the probability in certain regions of the lattice, it is necessary to distinguish the effect of the vacancy-induced localization and the effect of the focusing phase transformation. To quantify these two effects, we define two factors: the enhancement of the probability at the target molecule with respect to the initial value,

$$\eta = \frac{p'(t = t_*)}{p(t = 0)}, \quad (4.90)$$

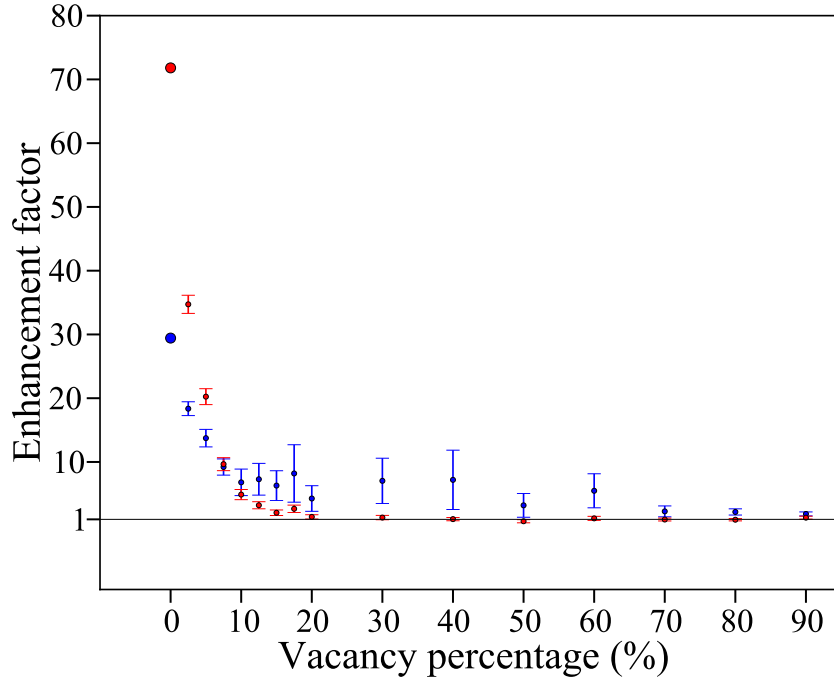


Figure 4.11: Enhancement factors η (red symbols) and χ (blue symbols) as functions of vacancy percentage in a 2D lattices. See text for the definitions of η and χ . The error bars are for 95% of confidence interval.

and the ratio of the probability to find the excitation on the target molecule with (p') and without (p) the focusing phase transformation,

$$\chi = \frac{p'(t = t_*)}{p(t = t_*)}. \quad (4.91)$$

The time t_* is the focusing time found numerically for the corresponding vacancy-free system. The quantity η illustrates the actual enhancement of the probability to focus a collective excitation, while the quantity χ illustrates the effect of the focusing phase transformation. Figure (4.11) presents the values of η and χ as functions of the vacancy concentration. It illustrates two important observations. First, the disorder potential with vacancy concentrations $> 20\%$ renders the phase transformation ineffective. In the presence of strong disorder, the dynamics of

the system is entirely determined by the disorder potential and the energy transfer becomes highly inefficient (however, see Section 4.7). On the other hand, vacancy concentrations of less than 10 % appear to have little effect on the efficacy of the focusing phase transformation.

Our calculations indicate that the focusing time may be somewhat modified by the disorder potential, even if the concentration of vacancies is less than 10 %. Figure (4.12) depicts the excitation wave functions at the time of the maximal enhancement on the target molecule, chosen as molecule (71,71). Figure 4.12 shows that despite the presence of multiple vacancies, the focusing transformation enhances the probability to find the excitation on the target molecule by 16 times.

4.7 Focusing in the presence of strong disorder

Although the focusing method demonstrated in Section 4.3 and Section 4.6 appears to be robust in the presence of a disorder potential induced by a small concentration of vacancies, it is important for practical applications to also consider controlled energy transfer in quantum arrays under a strong disorder potential. To consider focusing in a strongly disordered system, we employ an analogy with the “transfer matrix” methods for focusing of a collimated light beam in opaque medium [83–92].

In optics, a collimated laser beam passing through an opaque medium results in a random pattern of speckles arising from random scattering of light inside the medium [93]. Likewise, the random distribution of empty sites in an optical lattice with molecules scatters the exciton wavepackets, resulting in a completely random excited state. However, in optics, the randomness of the scattering centers inside the opaque medium can be compensated for by shaping the incident wavefront with a spatial light modulator such that the contributions from various parts of the medium can add constructively upon exit from the medium, producing a focus. We suggest that the same can be achieved with a many-body system on a lattice by separating the entire lattice into multiple blocks and applying proper phase transformations to those individual blocks.

The initial state for an ensemble of molecules on a lattice with multiple vacan-

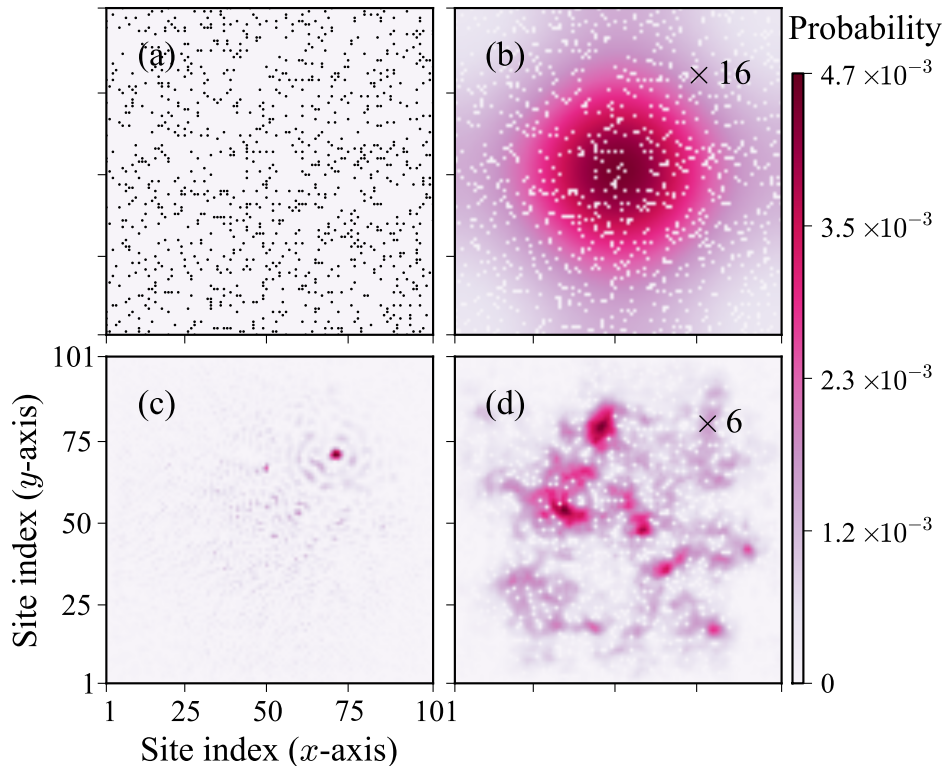


Figure 4.12: Time snapshots of a collective excitation in a 2D array with a vacancy concentration of 10 % (a) The distribution of the vacant sites; (b) The initial probability distribution of the excited state; (c) The probability distribution of the excitation at the focusing time when the focusing scheme is applied. The focusing time is found numerically as the time when the probability at the target molecule (71, 71) reaches maximum for a given phase transformation. (d) The probability distribution of the wave function at the focusing time when the focusing scheme is not applied. The calculations are performed with the same parameters as in Figure 4.5. The probabilities in (b) and (d) are magnified by 16 and 6 respectively.

cies can be written as

$$|\psi(t=0)\rangle = \sum_i c_i(t=0) |i\rangle , \quad (4.92)$$

where

$$|i\rangle = |e_i\rangle \prod_{j \neq i} |g_j\rangle \quad (4.93)$$

and the indexes i and j run over all occupied sites. After a long evolution time T , the probability amplitude for the excitation to reside on a particular target molecule is given by

$$c_o(T) = \sum_i U_{o,i}(T) c_i(t=0) \equiv \sum_i c_{oi}(T), \quad (4.94)$$

where $U_{o,i}(t) = \langle o | \exp[-iH_{\text{exc}}t] | i \rangle$ is a matrix element of the time evolution operator. In a disordered system, the transfer coefficients $U_{o,i}$ are not a-priori known and depend on the disorder potential. The phasors $c_{oi}(T)$ have quasi-random amplitudes and phases. While the amplitude of each phasor cannot be controlled experimentally, their phases are controllable via the phases of the coefficients c_i at $t = 0$, which can be tuned using the phase-kicking transformations introduced above. To achieve the highest probability at the target molecule, it is necessary to ensure that the contribution $c_{oi} = U_{o,i}(T)c_i(t=0)$ from every site i has the same phase so that they add up constructively.

In a practical implementation, it may be difficult to control the phase of each molecule in each individual site. It may be more desirable to work with blocks of several lattice sites. Assuming that the entire array of molecules can be divided into M blocks, each containing many molecules, and that the blocks can be perturbed individually, the excitation probability amplitude at the target molecule at time T is

$$c_o(T) = \sum_{\gamma=1}^M c_{\gamma}(T) \quad (4.95)$$

where the contribution from block γ is given by

$$c_{\gamma}(T) \equiv |c_{\gamma}| e^{i\phi_{\gamma}} = \sum_{i \in \gamma} U_{o,i}(T) c_i(t=0) . \quad (4.96)$$

In equation (4.96), the time evolution operator U depends on the randomness of vacancy sites and thus is out of control, but we can manipulate the initial state $c_i(t=0)$. It turns out that the contributions from different blocks can be made to interfere constructively by adding a phase $\exp(-i\phi_\gamma)$ to each occupied site in block γ . For M blocks in the array and quasi-random evolution matrix, simply setting all the phases equal may lead to $\sim M$ -fold increase of the excitation probability at the target molecule, as compared to a sum of M quasi-random phasors in equation (4.95) [83].

Similarly to optics, the phases $-\phi_\gamma$ which must be added in each block, can be found experimentally provided that the same (or similar) realization of disorder persists in a series of trials. A straightforward optimization would scan through the strengths of phase kicks applied to different blocks. In each experiment one would measure the excitation probability at the target molecule $|c_o(T)|^2$, e.g. via resonance fluorescence from the target molecule at the end of the experiment. More sophisticated optimization techniques, aimed at fast focusing multi-frequency light in optical systems, are currently under rapid development [84–92].

For a proof-of-principle calculation, we consider a 2D lattice of size 101×101 with 60% of sites vacant and each non-vacant site occupied by a single LiCs molecule. First, we figure out the phase $\exp(-i\phi_\gamma)$ applied to block γ . Due to time reversibility of the time evolution operator $U(T)$ and equation (4.96), we obtain

$$|c_\gamma| \exp(-i\phi_\gamma) = \left[\sum_{j=1}^n U_{o,j}^\gamma(T) c_j^\gamma(0) \right]^* = \left[\sum_{j=1}^n U_{j,o}^\gamma(-T) c_j^\gamma(0) \right]^*. \quad (4.97)$$

The matrix element $U_{j,o}^\gamma(-T)$ can be calculated by performing a backward time propagation starting from a local excitation at site “ o ” and calculating the coefficient $c_j(t)$ at time $-T$. Alternatively, one can propagate the evolution equations forward in time, finding $c_j(T)$: Since the Hamiltonian (1) is real, its eigenfunctions are real, and the evolution matrix U is symmetric, $U_{o,j} = U_{j,o}$. Thus we find

$$c_j(T) = \sum_i U_{j,i}^\gamma(T) c_i(0) = U_{j,o}^\gamma(T), \quad (4.98)$$

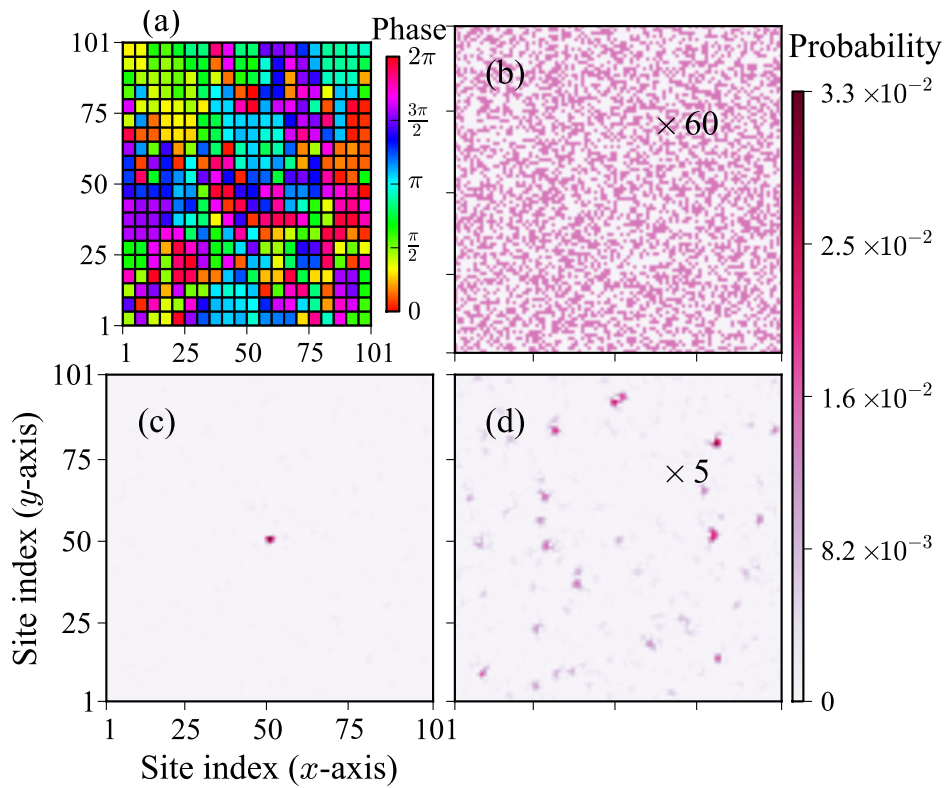


Figure 4.13: Focusing of a collective excitation in a strongly disordered system with 60% of lattice sites unoccupied. Panel (a) shows different phases applied to different blocks of the lattice before the time evolution. (b) The initial probability distribution of the excited state. (c) The probability distribution of the excited state at the focusing time $T = 3$ ms with the phase transformation depicted in panel (a) before the time evolution. (d) The probability distribution of the excited state at the focusing time $T = 3$ ms with no phase transformation applied. The calculations are performed with the same parameters as in Figure 4.5. The probabilities in (b) and (d) are magnified by 60 and 5, respectively.

since $c_o(0) = 1$ and all other coefficients are zero. For a completely delocalized initial state, we assume that all coefficients in equation (4.92) are equal, so that the phases ϕ_γ required for block γ are

$$|c_\gamma| \exp(-i\phi_\gamma) = \left[\sum_j c_j(T) \right]^*, \quad (4.99)$$

where the index j runs over all occupied sites in block γ . Figure 4.13 shows that this choice of phases leads to effective focusing of the collective excitation in a strongly disordered system.

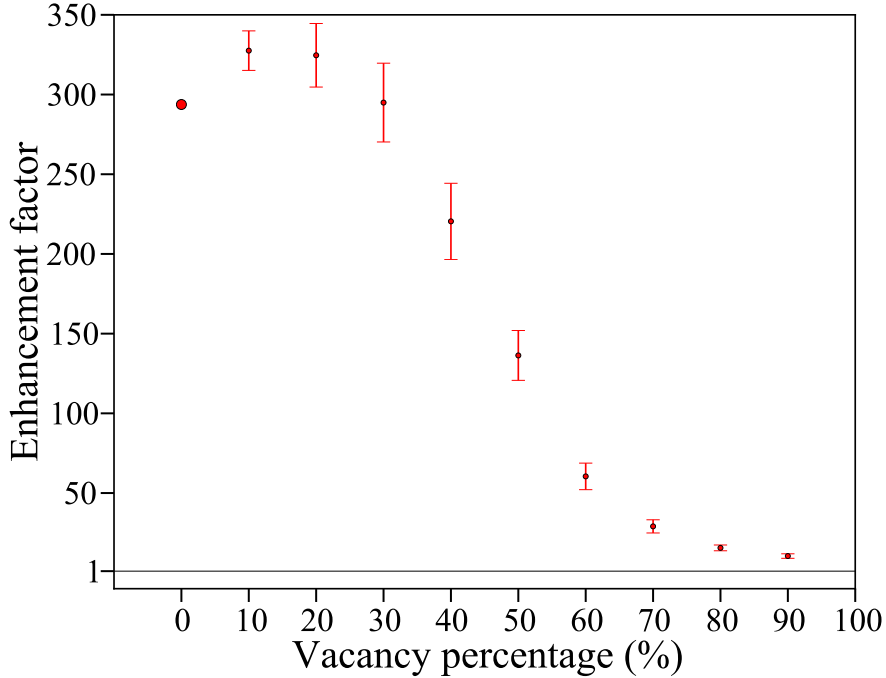


Figure 4.14: Efficiency of focusing collective excitations in strongly disordered 2D lattices. The molecular array is divided into 400 blocks as shown in Fig.4.13(a). The focusing time t_* is arbitrarily set to 4 ms. For each realization of disorder, we use Eq.(4.99) with $T = t_*$ to find the phase mask applied to different blocks. Shown are the enhancement factors η (red symbols) defined in Eq.(4.90), as a function of the vacancy percentage. The error bars are for 95% confidence interval.

To illustrate the efficiency of the focussing method described above, we have carried out a series of calculations with different vacancy concentrations. For each vacancy concentration, we performed 48 calculations with random distributions of empty lattice sites. The phase transformations are calculated individually for each random distribution of vacancy sites as described above. The results are shown in Figure 4.14. As can be seen, the transformations proposed above are effective for vacancy concentration $< 70\%$. At higher concentrations of vacancies, the excited states become strongly localized and immobile. The focusing efficiency at vacancy concentrations 10% and 20% appears to be higher than that in the absence of vacancies, which we attribute to the effect of the boundaries.

4.8 Conclusion

We have proposed a general method for controlling the time evolution of quantum energy transfer in ordered 1D and 2D arrays of coupled monomers. Any elementary excitation in an aggregate of coupled monomers can be represented as a coherent superposition of Frenkel exciton states. We propose shaping the exciton wave packets using nonadiabatic perturbations that temporarily modulate the energy levels of the monomers leading to monomer-dependent linear phase transformation and a displacement of the wave packets in the wave vector representation. This, combined with the possibility of focusing a collective excitation on a particular part of the lattice by a quadratic phase transformation and with the directed propagation of collective excitations, allows for control of energy transfer in the lattice. An experimental observation of the excitations described here can be achieved by measuring site-selective populations of the molecular or atomic states by applying a gradient of an electric field and detecting resonant transitions from Stark-shifted levels [35].

We have presented numerical calculations for an ensemble of polar molecules trapped on an optical lattice that demonstrate the feasibility of both momentum-shifting and focusing of collective excitations by applying external laser fields, with parameters that can be easily achieved in the laboratory. We have also investigated the effect of disorder potential arising from incomplete population of the lattice. Our results show that the phase transformations leading to focusing of collective

excitations on different regions of a 2D lattice remain effective in the presence of vacancies with concentrations not exceeding 10 %. For systems with larger concentrations of vacancies and affected by strong disorder potentials, we propose an alternative procedure based on engineering constructive interference of the wave function contributions arising from difference parts of the lattice.

The momentum-shifting technique proposed here can be used to protect collective excitations of ultracold atoms from spontaneous emission. The spontaneous decay processes, which in the case of an ordered many-body system must satisfy both the energy and wave vector conservation rules, can be restricted by shifting the exciton wave packets to a region of the dispersion curve, where the wave vector conservation cannot be satisfied. If performed faster than the spontaneous emission time, such phase transformations should create collective excitations with much longer lifetimes, which opens a variety of new applications for ultracold atoms on an optical lattice.

As was proposed by multiple authors [94–99], molecular wavepackets can be used to encode quantum information. Similarly, collective excitations can be used for quantum memory [23, 24]. Control over excitation transfer is needed for creating networks of quantum processors where information is transmitted over large distances with photons and stored in arrays of quantum monomers via one of the quantum memory protocols [100]. Momentum kicking can be used for wave packet transport within a single array. Focusing excitonic wave packets would enable local storage of information, while directed propagation combined with controlled interactions of multiple excitons [50] or excitons with lattice impurities [101] may be used to implement logic gates. Controlled energy transfer in molecular arrays may also be used for the study of controlled chemical interactions for a class of reactions stimulated by energy excitation of the reactants. Directing energy to a particular lattice site containing two or more reagents can be used to induce a chemical interaction [102], an inelastic collision or predissociation [103] with the complete temporal and spatial control over the reaction process.

Finally, the present work may prove to be important for simulations of open quantum systems. We have recently shown [20, 104] that the rotational excitations of ultracold molecules in an optical lattice can, by a suitable choice of the trapping laser fields, be effectively coupled to lattice phonons. The exciton - phonon cou-

plings can be tuned from zero to the regime of strong interactions [20, 104]. The possibility of shaping (accelerating, decelerating and focusing) collective excitations as described in the present work combined with the possibility of coupling these excitations to the phonon bath opens an exciting prospect of detailed study of controlled energy transfer in the presence of a controllable environment. Of particular interest would be to study the effect of the transition from a weakly coupled Markovian bath to a strongly coupled non-Markovian environment on energy transfer with specific initial parameters.

We note that the effect of site-dependent phase transformations on quantum transport was independently considered in Ref. [105] from the point of view of time-reversal symmetry breaking. The authors of Ref. [105] propose an experimental realization based on ions in a linear Paul trap. Their method relies on the possibility of tuning time-dependent phases, leading to new effects. The present work and Ref. [105] should be considered complementary.

Chapter 5

Lattice Green's function of two-particle state

5.1 Introduction

Green's function is an important theoretical tool in the study of condensed matter systems. Its applications range from

The numerical evaluation of the Green's function is a cumbersome task.

In this chapter, we extend the numerical method [106–108] developed by Berciu to a system with arbitrary disorders. Then we employ the Green's function to study the tunneling of biexciton states through a disorder.

5.2 Equation of motion for Green's function

To derive the equation of motion for Green's function, we start from the Hamiltonian for the system. We are considering a 1D periodic lattice with the Hamiltonian:

$$\hat{H} = \sum_l e_l \hat{P}_l^\dagger \hat{P}_l + \sum_l \sum_{r \neq 0} t_{l,l+r} \hat{P}_l^\dagger \hat{P}_{l+r} + \sum_l \sum_{r \neq 0} d_{l,l+r} \hat{P}_l^\dagger \hat{P}_{l+r}^\dagger \hat{P}_l \hat{P}_{l+r}, \quad (5.1)$$

where e_l is the energy of the particle at site l , \hat{P}_l^\dagger creates a particle at site l , $t_{l,l+r}$ represents the hopping interaction between site l and site $l+r$, and $d_{l,l+r}$ represents the dynamic interaction between site l and site $l+r$. Note that the Hamiltonian \hat{H}

is very general as there is no restriction on the values of e_l , $t_{l,l+r}$, and $d_{l,l+r}$, and thus it can describe both an ordered system and an disordered system. The Green's operator is defined in terms of the Hamiltonian,

$$\hat{G}(z) \equiv (z - \hat{H})^{-1}, \quad (5.2)$$

where $z = E + i\eta$ is the complex energy. From the definition of the Green's operator, it is clear that

$$(z - \hat{H})\hat{G}(z) = 1. \quad (5.3)$$

The above equation contains all information about the system.

Depending on the system in consideration, the creation and anihilation opreators will satisfy different commutation rules. For instance, if the particles are fermions, \hat{P}_n^\dagger and \hat{P}_m satisfy the anticommutation relations:

$$\begin{aligned} \{\hat{P}_n^\dagger, \hat{P}_m\} &= \hat{P}_n^\dagger \hat{P}_m + \hat{P}_m \hat{P}_n^\dagger = \delta_{n,m}, \\ \{\hat{P}_n^\dagger, \hat{P}_m^\dagger\} &= \{\hat{P}_n, \hat{P}_m\} = 0, \end{aligned} \quad (5.4)$$

and if particles are bosons, \hat{P}_n^\dagger and \hat{P}_m satisfy the commutation relations:

$$\begin{aligned} [\hat{P}_n^\dagger, \hat{P}_m] &= \hat{P}_n^\dagger \hat{P}_m - \hat{P}_m \hat{P}_n^\dagger = \delta_{n,m}, \\ [\hat{P}_n^\dagger, \hat{P}_m^\dagger] &= [\hat{P}_n, \hat{P}_m] = 0. \end{aligned} \quad (5.5)$$

In the current study, we are considering collective excitations of atom or molecules in the lattice. They have the characteristics of both fermions and bosons. When two excitations reside at different sites, they behave like bosons, that is,

$$\hat{P}_n^\dagger \hat{P}_m - \hat{P}_m \hat{P}_n^\dagger = 0 \quad (5.6)$$

if $n \neq m$; when excitations are at the same site, they behave like fermions, that is,

$$\hat{P}_n^\dagger \hat{P}_m + \hat{P}_m \hat{P}_n^\dagger = 0 \quad (5.7)$$

if $n = m$. For convenience, we can combine equation (5.6) and equation (5.7) into

one equation:

$$\hat{P}_m \hat{P}_n^\dagger = \delta_{m,n} + (1 - 2\delta_{m,n}) \hat{P}_n^\dagger \hat{P}_m . \quad (5.8)$$

Using the two-particle basis set $|n\rangle|m\rangle$ (and $n \neq m$), equation (5.3) can be rewritten as

$$\langle n| \langle m| (z - \hat{H}) \hat{G}(z) |n'\rangle|m'\rangle = \langle n| \langle m| |n'\rangle|m'\rangle . \quad (5.9)$$

To simplify the above equation, we make use of equation (5.8) and evaluate the effect of the Hamiltonian operating on the basis set:

$$\begin{aligned} \hat{H}|n\rangle|m\rangle &= (e_n + e_m)|n\rangle|m\rangle + \sum_{r \neq 0} (1 - \delta_{n-r,m}) t_{n-r,n} |n-r\rangle|m\rangle \\ &\quad + \sum_{r \neq 0} (1 - \delta_{n,m-r}) t_{m-r,m} |n\rangle|m-r\rangle + \sum_{r \neq 0} d_{n,m} \delta_{n-m,\pm r} |n\rangle|m\rangle , \end{aligned} \quad (5.10)$$

where the factors like $(1 - \delta_{n-r,m})$ appear because only the two-particle states $|n\rangle|m\rangle$ with $n \neq m$ are included in the basis set, then the left hand side of equation (5.9) becomes

$$\begin{aligned} &\langle n| \langle m| (z - \hat{H}) \hat{G}(z) |n'\rangle|m'\rangle \\ &= (z - e_n - e_m) G(n, m, n', m'; z) - \sum_{r \neq 0} (1 - \delta_{n-r,m}) t_{n-r,n} G(n-r, m, n', m'; z) \\ &\quad - \sum_{r \neq 0} (1 - \delta_{n,m-r}) t_{m-r,m} G(n, m-r, n', m'; z) - \sum_{r \neq 0} d_{n,m} \delta_{n-m,\pm r} G(n, m, n', m'; z) , \end{aligned} \quad (5.11)$$

where $G(n, m, n', m'; z)$ represents the matrix element of the Green's operator in the two-particle basis set and it is given by

$$G(n, m, n', m'; z) = \langle n| \langle m| \hat{G}(z) |n'\rangle|m'\rangle . \quad (5.12)$$

Similarly, substituting equation (5.8) into the right hand side of equation (5.9) gives rise to

$$\langle n| \langle m| |n'\rangle|m'\rangle = \delta_{m,n'} \delta_{n,m'} + \delta_{n,n'} \delta_{m,m'} . \quad (5.13)$$

Therefore, the equation of the motion for the Green's function is given by

$$\begin{aligned}
& \left(z - e_n - e_m - \sum_{r \neq 0} d_{n,m} \delta_{n-m, \pm r} \right) G(n, m, n', m'; z) \\
& - \sum_{r \neq 0} (1 - \delta_{n-r, m}) t_{n-r, n} G(n - r, m, n', m'; z) \\
& - \sum_{r \neq 0} (1 - \delta_{n, m-r}) t_{m-r, m} G(n, m - r, n', m'; z) \\
& = \delta_{m, n'} \delta_{n, m'} + \delta_{n, n'} \delta_{m, m'} . \tag{5.14}
\end{aligned}$$

Because two excitations cannot reside at the same lattice site, we know the Green's function $G(n, m, n', m'; z)$ is meaningless whenever $n = m$ or $n' = m'$. It is clear that equation (5.14) can't guarantee all the Green's functions that it contains are physical even if we restrict the basis set to be just $|i\rangle|j\rangle$ where $i \neq j$. That's why the factors like $(1 - \delta_{n, m-r})$ appear.

Since all the Green's function in equation (5.14) have the same parameters n' and m' , we define

$$\tilde{G}(n, m; z) = G(n, m, n', m'; z) \tag{5.15}$$

to simplify the notation. Then equation (5.14) can be written as

$$\begin{aligned}
& \left(z - e_n - e_m - \sum_{r \neq 0} d_{n,m} \delta_{n-m, \pm r} \right) \tilde{G}(n, m; z) \\
& - \sum_{r \neq 0} (1 - \delta_{n-r, m}) t_{n-r, n} \tilde{G}(n - r, m; z) - \sum_{r \neq 0} (1 - \delta_{n, m-r}) t_{m-r, m} \tilde{G}(n, m - r; z) \\
& = \delta_{m, n'} \delta_{n, m'} + \delta_{n, n'} \delta_{m, m'} . \tag{5.16}
\end{aligned}$$

5.3 Recursive calculation of Green's function

5.3.1 In the nearest neighbor approximation

The equation of motion of Green's function, equation (5.16), is our starting point to calculate the Green's function. In the nearest neighbor approximation, the distance between two interacting sites r can only be 1 or -1 , then the equation of motion of

Green's function becomes

$$\begin{aligned}
& (z - e_n - e_m - d_{n,m} \delta_{n-m,\pm 1}) \tilde{G}(n,m;z) \\
& - (1 - \delta_{n-1,m}) t_{n-1,n} \tilde{G}(n-1,m;z) - (1 - \delta_{n+1,m}) t_{n+1,n} \tilde{G}(n+1,m;z) \\
& - (1 - \delta_{n,m-1}) t_{m-1,m} \tilde{G}(n,m-1;z) - (1 - \delta_{n,m+1}) t_{m+1,m} \tilde{G}(n,m+1;z) \\
& = \delta_{m,n'} \delta_{n,m'} + \delta_{n,n'} \delta_{m,m'} .
\end{aligned} \tag{5.17}$$

As mentioned before, the factors like $(1 - \delta_{n-1,m})$ in equation (5.17) are used to eliminate the unphysical Green's functions like $\tilde{G}(i,i;z)$. For instance, when $n = m - 1$, $\tilde{G}(n+1,m;z)$ and $\tilde{G}(n,m-1;z)$ will disappear in equation (5.17) because of the factors in front of them. Equation (5.17) shows that $\tilde{G}(n,m;z)$ only relates directly with at most four other Green's functions in the nearest neighbor approximation. This relationship can be shown schematically as follows:

$$\begin{array}{lcl}
& \vdots & \\
\tilde{G}(n-1,m+1;z) & \rightarrow & \left\{ \tilde{G}(n-2,m+1;z), \tilde{G}(n-1,m;z), \tilde{G}(n,m+1;z), \tilde{G}(n-1,m+2;z) \right\} \\
\tilde{G}(n,m;z) & \rightarrow & \left\{ \tilde{G}(n-1,m;z), \tilde{G}(n,m-1;z), \tilde{G}(n+1,m;z), \tilde{G}(n,m+1;z) \right\} \\
\tilde{G}(n+1,m-1;z) & \rightarrow & \left\{ \tilde{G}(n,m-1;z), \tilde{G}(n+1,m-2;z), \tilde{G}(n+2,m-1;z), \tilde{G}(n+1,m;z) \right\} \\
& \vdots &
\end{array} \tag{5.18}$$

For the Green's function $\tilde{G}(i,j;z)$ on the left, the summation of parameters $i + j = n + m$ is fixed. For the Green's functions $\tilde{G}(i',j';z)$ on the right, the summation of parameters $i' + j'$ can only be either $n + m - 1$ or $n + m + 1$. This inspire us to group some Green's functions into a vector \mathbf{V}_K according to their parameters n and

m , that is,

$$\mathbf{V}_K = \begin{pmatrix} \vdots \\ \tilde{G}(i-1, j+1; z) \\ \tilde{G}(i, j; z) \\ \tilde{G}(i+1, j-1; z) \\ \vdots \end{pmatrix}, \quad (5.19)$$

then equation (5.17) can be written as

$$\mathbf{V}_K = \boldsymbol{\alpha}_K(z)\mathbf{V}_{K-1} + \boldsymbol{\beta}_K(z)\mathbf{V}_{K+1} \quad (5.20)$$

if $n' + m' \neq K$, and as

$$\mathbf{V}_K = \boldsymbol{\alpha}_K(z)\mathbf{V}_{K-1} + \boldsymbol{\beta}_K(z)\mathbf{V}_{K+1} + \mathbf{C} \quad (5.21)$$

if $n' + m' = K$. In the above two equations, $\boldsymbol{\alpha}_K(z)$ and $\boldsymbol{\beta}_K(z)$ are matrices and \mathbf{C} is a constant vector, and their values can be determined from equation (5.17). Because the two excitations are indistinguishable from each other, $\tilde{G}(n, m; z)$ is equivalent to $\tilde{G}(m, n; z)$. In the following discussion, we require $n < m$ in all $\tilde{G}(n, m; z)$ to reduce the dimension of \mathbf{V}_K by half.

Deriving the expression for $\boldsymbol{\alpha}_K(z)$ and $\boldsymbol{\beta}_K(z)$ by hand is tedious, we choose to do that in a programmable way. The pseudocode is given below:

- 1: Form all the vectors \mathbf{V}_K for $K = 1$ to $2N - 1$
- 2: Generate the index $\mathbf{I}(n, m)$ of every $\tilde{G}(n, m; z)$ such that the $\mathbf{I}(n, m)$ th element of \mathbf{V}_{n+m} is $\tilde{G}(n, m; z)$, that is $\mathbf{V}_{n+m}[\mathbf{I}(n, m)] = \tilde{G}(n, m; z)$
- 3: **for** every $\tilde{G}(i, j; z)$ in \mathbf{V}_K **do**
- 4: $n^{\text{th}} \leftarrow \mathbf{I}(i, j)$
- 5: Set every element of $\boldsymbol{\alpha}_K$ to 0
- 6: **if** $i - 1 \geq 0$ **then**
- 7: $m^{\text{th}} \leftarrow \mathbf{I}(i - 1, j)$
- 8: $\boldsymbol{\alpha}_K(n^{\text{th}}, m^{\text{th}}) \leftarrow \frac{t_{i-1,i}}{z - e_i - e_j - d_{i,j} \delta_{j-i,1}}$
- 9: **end if**
- 10: **if** $j - 1 > i$ **then**
- 11: $m^{\text{th}} \leftarrow \mathbf{I}(i, j - 1)$

```

12:    $\alpha_K(n^{\text{th}}, m^{\text{th}}) \leftarrow \frac{t_{j-1,j}}{z - e_i - e_j - d_{i,j} \delta_{j-i,1}}$ 
13:   end if
14:   Set every element of  $\beta_K$  to 0
15:   if  $i + 1 < j$  then
16:      $m^{\text{th}} \leftarrow \mathbf{I}(i + 1, j)$ 
17:      $\beta_K(n^{\text{th}}, m^{\text{th}}) \leftarrow \frac{t_{i,i+1}}{z - e_i - e_j - d_{i,j} \delta_{j-i,1}}$ 
18:   end if
19:   if  $j + 1 \leq N$  then
20:      $m^{\text{th}} \leftarrow \mathbf{I}(i, j + 1)$ 
21:      $\beta_K(n^{\text{th}}, m^{\text{th}}) \leftarrow \frac{t_{j,j+1}}{z - e_i - e_j - d_{i,j} \delta_{j-i,1}}$ 
22:   end if
23: end for

```

As we will show in the next subsection, the above algorithm is even more useful when the coupling equations like equation (5.17) get more complicated in the cases of longer range interaction and high-dimensional systems.

It is clear from equation (5.20) and equation (5.21) that \mathbf{V}_K relates only with \mathbf{V}_{K-1} and \mathbf{V}_{K+1} . This gives the opportunity to solve for individual \mathbf{V}_K recursively provided that a starting point is given. For example, given the values for two particular \mathbf{V}_K and \mathbf{V}_{K-1} , we can obtain \mathbf{V}_{K+1} , and then calculate \mathbf{V}_{K+2} from \mathbf{V}_K and \mathbf{V}_{K+1} , and etc. But where do we start? The hint comes from the following physical arguments: $G(n + \delta n, m + \delta m, n, m; z)$ is expected to approach zero as $|\delta n| \rightarrow \infty$ and $|\delta m| \rightarrow \infty$ because its Fourier transform $G(n + \delta n, m + \delta m, n, m; t)$ represents the amplitude for the two particles to move a distance δn and δm respectively in time t [38, 106]. To figures out which Green's functions can be approximated by zero, we fix the values of n' and m' . Suppose $K_c = n' + m'$, then we can assume \mathbf{V}_K approaches zero when $|K - K_c| \rightarrow \infty$. For the purpose of numerical computation, a cutoff distance M is chosen such that \mathbf{V}_{K_c-M} and \mathbf{V}_{K_c+M} are very small. In this case, the infinite crystal is replaced by a finite crystal whose central region contains site n' and site m' . To ensure the convergence of the results, the finite crystal must be large enough such that its boundaries are far away from both site n and site m . Assuming the 1D finite crystal has $N + 1$ lattice sites indexed by $0, 1, \dots, N - 1, N$, the starting point for the recursive calculation of the Green's function are the following

two approximations:

$$\begin{aligned}\mathbf{V}_{2N-1} &\approx 0, \\ \mathbf{V}_1 &\approx 0.\end{aligned}\tag{5.22}$$

Given the two approximations in equation (5.22), we are ready to calculate the Green's functions recursively. Instead of working with the vectors \mathbf{V}_K directly, we define two quantities \mathbf{A}_K and $\tilde{\mathbf{A}}_K$ that relates two consecutive vectors \mathbf{V}_K and \mathbf{V}_{K-1} . For $n \geq K_c + 1$, we have

$$\mathbf{V}_{n+1} = \mathbf{A}_{n+1} \mathbf{V}_n, \tag{5.23}$$

and for $n \leq K_c - 1$, we have

$$\mathbf{V}_n = \tilde{\mathbf{A}}_n \mathbf{V}_{n+1}. \tag{5.24}$$

The validity of the above two equations can be verified by substituting equation (5.22) into equation (5.20) and solving \mathbf{V}_K recursively. Because \mathbf{V}_{K_c} satisfies equation (5.21) rather than equation (5.20), equation (5.23) and equation (5.24) are not valid for $n = K_c$. At the left boundary of the crystal for which $n = 1$, we have

$$\mathbf{V}_1 = \boldsymbol{\beta}_1(z) \mathbf{V}_2 \tag{5.25}$$

because of equation (5.20), and compare it with equation (5.24), we conclude

$$\tilde{\mathbf{A}}_1 = \boldsymbol{\beta}_1(z). \tag{5.26}$$

There is a recursive relation between different $\tilde{\mathbf{A}}_n$. Substituting $\mathbf{V}_{n-1} = \tilde{\mathbf{A}}_{n-1} \mathbf{V}_n$ into equation (5.20), we obtain

$$\mathbf{V}_n = [1 - \boldsymbol{\alpha}_n(z) \tilde{\mathbf{A}}_{n-1}]^{-1} \boldsymbol{\beta}_n(z) \mathbf{V}_{n+1}, \tag{5.27}$$

which upon comparsion with equation (5.24) gives rise to

$$\tilde{\mathbf{A}}_n = [1 - \boldsymbol{\alpha}_n(z) \tilde{\mathbf{A}}_{n-1}]^{-1} \boldsymbol{\beta}_n(z). \tag{5.28}$$

Since equation (5.28) involves matrix inversion which is difficult to compute numerically, we may calculate $\tilde{\mathbf{A}}_n$ by solving the linear equation

$$[1 - \boldsymbol{\alpha}_n(z)\tilde{\mathbf{A}}_{n-1}] \tilde{\mathbf{A}}_n = \boldsymbol{\beta}_n(z). \quad (5.29)$$

Similarly at the right boundary of the crystal for which $n = 2N - 1$, we obtain the starting value of \mathbf{A}_K

$$\mathbf{A}_{2N-1} = \boldsymbol{\alpha}_{2N-1}(z), \quad (5.30)$$

and the recursive relation

$$\mathbf{A}_n = [1 - \boldsymbol{\beta}_n(z)\mathbf{A}_{n+1}]^{-1} \boldsymbol{\alpha}_n(z). \quad (5.31)$$

To calculate the Green's functions, we start from the left boundary of the crystal and calculate $\tilde{\mathbf{A}}_1, \tilde{\mathbf{A}}_2, \dots$, from left to center until $\tilde{\mathbf{A}}_{K_c-1}$ is reached. We have to stop there because equation (5.24) is not valid for \mathbf{V}_{K_c} . Then we proceed from the right boundary to the center and calculate $\mathbf{A}_{2N-1}, \mathbf{A}_{2N-2}, \dots$ and stop until we reach \mathbf{A}_{K_c+1} beyond which equation (5.23) is not valid. Knowing the value of \mathbf{A}_{K_c+1} and $\tilde{\mathbf{A}}_{K_c-1}$, we rewrite \mathbf{V}_{K_c+1} and \mathbf{V}_{K_c-1} in terms of \mathbf{V}_{K_c} :

$$\begin{aligned} \mathbf{V}_{K_c+1} &= \mathbf{A}_{K_c+1}\mathbf{V}_{K_c}, \\ \mathbf{V}_{K_c-1} &= \tilde{\mathbf{A}}_{K_c-1}\mathbf{V}_{K_c}, \end{aligned} \quad (5.32)$$

and substitute them into equation (5.21) to obtain the solution for \mathbf{V}_{K_c} :

$$\mathbf{V}_{K_c} = [1 - \boldsymbol{\alpha}_{K_c}(z)\tilde{\mathbf{A}}_{K_c-1} - \boldsymbol{\beta}_{K_c}(z)\mathbf{A}_{K_c+1}]^{-1} \mathbf{C}. \quad (5.33)$$

Once \mathbf{V}_{K_c} is known, all \mathbf{V}_n can be calculated from equation (5.23) and equation (5.24) given the values for \mathbf{A}_{n+1} and $\tilde{\mathbf{A}}_n$.

In summary, the aforementioned calculation of Green's function is carried on in the following steps:

1. fix the value of n' and m' in the Green's function $G(n, m, n', m'; z)$, assume the two approximations in equation (5.22), and calculate $\tilde{\mathbf{A}}_1$ from equation (5.26) and \mathbf{A}_{2N-1} from equation (5.30)

2. start from $\tilde{\mathbf{A}}_1$ and calculate $\tilde{\mathbf{A}}_2, \tilde{\mathbf{A}}_3, \dots, \tilde{\mathbf{A}}_{K_c-1}$ from equation (5.28)
3. start from \mathbf{A}_{2N-1} and calculate $\mathbf{A}_{2N-1}, \mathbf{A}_{2N-2}, \dots, \mathbf{A}_{K_c+1}$ from equation (5.31)
4. use the values of $\tilde{\mathbf{A}}_{K_c-1}$ and \mathbf{A}_{K_c+1} to calculate \mathbf{V}_{K_c} from equation (5.33)
5. start from \mathbf{V}_{K_c} and calculate $\mathbf{V}_{K_c-1}, \mathbf{V}_{K_c-2}, \dots, \mathbf{V}_1$ from equation (5.24)
6. start from \mathbf{V}_{K_c} and calculate $\mathbf{V}_{K_c+1}, \mathbf{V}_{K_c+2}, \dots, \mathbf{V}_{2N-1}$ from equation (5.23)

5.3.2 Extension to long-range interaction

As mentioned in Section 4.5.1, dipole-dipole interaction is long-ranged and the nearest neighbor approximation may not represent the physical picture accurately. So it is desirable to extend the calculation method of Green's function in Section 5.3.1 to the case of long-range interaction.

First, we consider a 1D lattice with the same Hamiltonian (see equation (5.1)) that has both first nearest-neighbor and second nearest-neighbor interactions. Then the equation of motion for the Green's function becomes

$$\begin{aligned}
& (z - e_n - e_m - d_{n,m} \delta_{m-n,\pm 1} - d_{n,m} \delta_{m-n,\pm 2}) \tilde{G}(n,m;z) \\
& - (1 - \delta_{n-1,m}) t_{n-1,n} \tilde{G}(n-1,m;z) - (1 - \delta_{n+1,m}) t_{n+1,n} \tilde{G}(n+1,m;z) \\
& - (1 - \delta_{n,m-1}) t_{m-1,m} \tilde{G}(n,m-1;z) - (1 - \delta_{n,m+1}) t_{m+1,m} \tilde{G}(n,m+1;z) \\
& - (1 - \delta_{n-2,m}) t_{n-2,n} \tilde{G}(n-2,m;z) - (1 - \delta_{n+2,m}) t_{n+2,n} \tilde{G}(n+2,m;z) \\
& - (1 - \delta_{n,m-2}) t_{m-2,m} \tilde{G}(n,m-2;z) - (1 - \delta_{n,m+2}) t_{m+2,m} \tilde{G}(n,m+2;z) \\
& = \delta_{m,n'} \delta_{n,m'} + \delta_{n,n'} \delta_{m,m'} . \tag{5.34}
\end{aligned}$$

The above equation shows that the Green's functions $\tilde{G}(n',m';z)$ are only coupled with the Green's function $\tilde{G}(i,j;z)$ whose parameters i and j sum up to $n+m-1$ or $n+m+1$ or $n+m-2$ or $n+m+2$. As in the case of nearest neighbor approximation, we can group the Green's functions according to the summation of their parameters and obtain:

$$\mathbf{Z}_K \mathbf{V}_K = \mathbf{M}_{K,K+1} \mathbf{V}_{K+1} + \mathbf{M}_{K,K-1} \mathbf{V}_{K-1} + \mathbf{M}_{K,K+2} \mathbf{V}_{K+2} + \mathbf{M}_{K,K-2} \mathbf{V}_{K-2} , \tag{5.35}$$

where \mathbf{V}_K has the same definition as in equation (5.48). Different from the NNA case where the recurrence relation links three consecutive terms \mathbf{V}_K , \mathbf{V}_{K-1} and \mathbf{V}_{K+1} , equation (5.35) has two extra terms \mathbf{V}_{K-2} and \mathbf{V}_{K+2} . At first glance, adding the second nearest-neighbor interactions invalidates the method presented in Section 5.3.1 as the calculation of Green's function relies on a recurrence relation linking three consecutive terms. But if we work with combinations of \mathbf{V}_K instead of individual \mathbf{V}_K , we can obtain the proper recurrence relation. Replacing K with $K+1$ in equation (5.35), we obtain

$$\mathbf{Z}_{K+1}\mathbf{V}_{K+1} = \mathbf{M}_{K+1,K+2}\mathbf{V}_{K+2} + \mathbf{M}_{K+1,K}\mathbf{V}_K + \mathbf{M}_{K+1,K+3}\mathbf{V}_{K+3} + \mathbf{M}_{K+1,K-1}\mathbf{V}_{K-1}. \quad (5.36)$$

Equation (5.35) and equation (5.36) can be written in the following form:

$$\mathbf{W}_{2K+1} \begin{pmatrix} \mathbf{V}_K \\ \mathbf{V}_{K+1} \end{pmatrix} = \boldsymbol{\alpha}_{2K-3} \begin{pmatrix} \mathbf{V}_{K-2} \\ \mathbf{V}_{K-1} \end{pmatrix} + \boldsymbol{\beta}_{2K+5} \begin{pmatrix} \mathbf{V}_{K+2} \\ \mathbf{V}_{K+3} \end{pmatrix} \quad (5.37)$$

where

$$\mathbf{W}_{2K+1} = \begin{pmatrix} \mathbf{Z}_K & -\mathbf{M}_{K,K+1} \\ -\mathbf{M}_{K+1,K} & \mathbf{Z}_{K+1} \end{pmatrix}, \quad (5.38)$$

$$\boldsymbol{\alpha}_{2K-3} = \begin{pmatrix} \mathbf{M}_{K,K-2} & -\mathbf{M}_{K,K-1} \\ \mathbf{0} & \mathbf{Z}_{K+1,K-1} \end{pmatrix}, \quad (5.39)$$

$$\boldsymbol{\beta}_{2K+5} = \begin{pmatrix} \mathbf{M}_{K,K+2} & \mathbf{0} \\ \mathbf{M}_{K+1,K+2} & \mathbf{Z}_{K+1,K+3} \end{pmatrix}. \quad (5.40)$$

Comparing equation (5.37) with equation (5.20), we can see that the method introduced in Section 5.3.1 will also work for the current case if we define

$$\tilde{\mathbf{V}}_{2K+1} \equiv \begin{pmatrix} \mathbf{V}_K \\ \mathbf{V}_{K+1} \end{pmatrix} \quad (5.41)$$

and use the series of vectors $\tilde{\mathbf{V}}_1, \tilde{\mathbf{V}}_5, \tilde{\mathbf{V}}_9, \dots$ rather than $\mathbf{V}_1, \mathbf{V}_2, \mathbf{V}_3, \dots$.

To further illustrate the point, we consider an even longer range interaction with the first nearest-neighbor, second nearest-neighbor, and the third nearest-neighbor

couplings. Similarly, we work with a set of equations that relate different \mathbf{V}_K :

$$\begin{aligned}\mathbf{Z}_K \mathbf{V}_K = & \mathbf{M}_{K,K+1} \mathbf{V}_{K+1} + \mathbf{M}_{K,K-1} \mathbf{V}_{K-1} + \mathbf{M}_{K,K+2} \mathbf{V}_{K+2} + \mathbf{M}_{K,K-2} \mathbf{V}_{K-2} \\ & + \mathbf{M}_{K,K+3} \mathbf{V}_{K+3} + \mathbf{M}_{K,K-3} \mathbf{V}_{K-3},\end{aligned}\quad (5.42)$$

$$\begin{aligned}\mathbf{Z}_{K+1} \mathbf{V}_{K+1} = & \mathbf{M}_{K+1,K+2} \mathbf{V}_{K+2} + \mathbf{M}_{K+1,K} \mathbf{V}_K + \mathbf{M}_{K+1,K+3} \mathbf{V}_{K+3} + \mathbf{M}_{K+1,K-1} \mathbf{V}_{K-1} \\ & + \mathbf{M}_{K+1,K+4} \mathbf{V}_{K+4} + \mathbf{M}_{K+1,K-2} \mathbf{V}_{K-2},\end{aligned}\quad (5.43)$$

$$\begin{aligned}\mathbf{Z}_{K+2} \mathbf{V}_{K+2} = & \mathbf{M}_{K+2,K+3} \mathbf{V}_{K+3} + \mathbf{M}_{K+2,K+1} \mathbf{V}_{K+1} + \mathbf{M}_{K+2,K+4} \mathbf{V}_{K+4} + \mathbf{M}_{K+2,K} \mathbf{V}_K \\ & + \mathbf{M}_{K+2,K+5} \mathbf{V}_{K+5} + \mathbf{M}_{K+2,K-1} \mathbf{V}_{K-1}.\end{aligned}\quad (5.44)$$

These equations give rise to a recurrence relation that links three vectors:

$$\begin{aligned}& \begin{pmatrix} \mathbf{Z}_K & -\mathbf{M}_{K,K+1} & -\mathbf{M}_{K,K+2} \\ -\mathbf{M}_{K+1,K} & \mathbf{Z}_{K+1} & -\mathbf{M}_{K+1,K+2} \\ -\mathbf{M}_{K+2,K} & -\mathbf{M}_{K+2,K+1} & \mathbf{Z}_{K+2} \end{pmatrix} \begin{pmatrix} \mathbf{V}_K \\ \mathbf{V}_{K+1} \\ \mathbf{V}_{K+2} \end{pmatrix} \\ &= \begin{pmatrix} \mathbf{M}_{K,K-3} & \mathbf{M}_{K,K-2} & \mathbf{M}_{K,K-1} \\ \mathbf{0} & \mathbf{M}_{K+1,K-2} & \mathbf{M}_{K+1,K-1} \\ \mathbf{0} & \mathbf{0} & \mathbf{M}_{K+2,K-1} \end{pmatrix} \begin{pmatrix} \mathbf{V}_{K-3} \\ \mathbf{V}_{K-2} \\ \mathbf{V}_{K-1} \end{pmatrix} \\ &+ \begin{pmatrix} \mathbf{M}_{K,K+3} & \mathbf{0} & \mathbf{0} \\ \mathbf{M}_{K+1,K+3} & \mathbf{M}_{K+1,K+4} & \mathbf{0} \\ \mathbf{M}_{K+2,K+3} & \mathbf{M}_{K+2,K+4} & \mathbf{M}_{K+2,K+5} \end{pmatrix} \begin{pmatrix} \mathbf{V}_{K+3} \\ \mathbf{V}_{K+4} \\ \mathbf{V}_{K+5} \end{pmatrix}\end{aligned}\quad (5.45)$$

The above recurrence relation is in the form of equation (5.37), and a new vector can be defined as

$$\bar{\mathbf{V}}_{3K+3} \equiv \begin{pmatrix} \mathbf{V}_K \\ \mathbf{V}_{K+1} \\ \mathbf{V}_{K+2} \end{pmatrix}. \quad (5.46)$$

Then we can use the series of vectors $\bar{\mathbf{V}}_3, \bar{\mathbf{V}}_{12}, \bar{\mathbf{V}}_{21}, \dots$ in the recursive calculations.

It is clear from the above discussion that the recursive method to calculate the Green's function can be applied to any finite range interactions and the dimensions

of the matrices increase linearly with respect to the number of neighbors included. As the coupling equations get more and more complicated, it becomes more difficult to derive the expressions for \mathbf{Z} 's and \mathbf{M} 's by hand. Fortunately the algorithm presented in Section 5.3.1 can be easily adapted to do this kind of computations. For example, the following algorithm can be used to calculate $\mathbf{M}_{K,K-2}$ and $\mathbf{M}_{K,K+2}$:

```

1: for every  $\tilde{G}(i, j; z)$  in  $\mathbf{V}_K$  do
2:    $n^{\text{th}} \leftarrow \mathbf{I}(i, j)$ 
3:   Set every element of  $\mathbf{M}_{K,K-2}$  to 0
4:   if  $i - 2 \geq 0$  then
5:      $m^{\text{th}} \leftarrow \mathbf{I}(i - 2, j)$ 
6:      $\mathbf{M}_{K,K-2}(n^{\text{th}}, m^{\text{th}}) \leftarrow t_{i-2,i}$ 
7:   end if
8:   if  $j - 2 > i$  then
9:      $m^{\text{th}} \leftarrow \mathbf{I}(i, j - 2)$ 
10:     $\mathbf{M}_{K,K-2}(n^{\text{th}}, m^{\text{th}}) \leftarrow t_{j-2,j}$ 
11:   end if
12:   Set every element of  $\mathbf{M}_{K,K+2}$  to 0
13:   if  $i + 2 < j$  then
14:      $m^{\text{th}} \leftarrow \mathbf{I}(i + 2, j)$ 
15:      $\mathbf{M}_{K,K+2}(n^{\text{th}}, m^{\text{th}}) \leftarrow t_{i+2,i}$ 
16:   end if
17:   if  $j + 2 \leq N$  then
18:      $m^{\text{th}} \leftarrow \mathbf{I}(i, j + 2)$ 
19:      $\mathbf{M}_{K,K+2}(n^{\text{th}}, m^{\text{th}}) \leftarrow t_{j,j+2}$ 
20:   end if
21: end for
```

5.3.3 Extension to high-dimensional system

In the last two subsections, we only discuss the 1D lattice. It turns out that extending the method to a high-dimensional system is straightforward. For instance, in

the case of a 2D lattice, we want to calculate the Green's function

$$\tilde{G}(n_x, n_y, m_x, m_y; z) \equiv \langle n_x, n_y | \langle m_x, m_y | \hat{G}(z) | n'_x, n'_y \rangle | m'_x, m'_y \rangle , \quad (5.47)$$

where $|n_x, n_y\rangle$ represents the state of the particle at site (n_x, n_y) and n'_x, n'_y, m'_x , and m'_y are fixed. Due to the structure of the equation of the motion of the Green's function, one Green's function is only coupled with a certain set of other Green's functions. In the nearest neighbor approximation, we can group the Green's functions into different vectors by defining

$$\mathbf{V}_{i_x+i_y+j_x+j_y} = \begin{pmatrix} \dots \\ \tilde{G}(i_x - 1, i_y + 1, j_x, j_y; z) \\ \tilde{G}(i_x, i_y, j_x - 1, j_y + 1; z) \\ \tilde{G}(i_x, i_y, j_x, j_y; z) \\ \tilde{G}(i_x, i_y, j_x + 1, j_y - 1; z) \\ \tilde{G}(i_x + 1, i_y - 1, j_x, j_y; z) \\ \vdots \end{pmatrix} . \quad (5.48)$$

and then the same procedure in Section 5.3.1 will follows. Note that the algorithm in Section 5.3.1 can also be applied here with only a small change.

5.3.4 Advantages of the recursive method

Conventionally, Green's function can be calculated by a brute-force approach. The first step is to diagonalize the Hamiltonian H and calculate the spectrum

$$H|\phi_n(\mathbf{R})\rangle = \lambda_n|\phi_n(\mathbf{R})\rangle , \quad (5.49)$$

where n indicates the n^{th} eigenvector of the system and \mathbf{R} represents the position of the particles. Then from the definition of the Green's operator $\hat{G} = (z - H)^{-1}$, we obtain the Green's function

$$G(\mathbf{R}, \mathbf{R}'; z) = \sum_n' \frac{\phi_n(\mathbf{R})\phi_n^*(\mathbf{R}')}{z - \lambda_n} , \quad (5.50)$$

where \sum'_n represents the summation over the discrete spectrum and the integration over the continuous spectrum.

This brute-force method is simple but the computational cost is large. Consider a two-particle states $|i\rangle|j\rangle$ in a 1D lattice with $N \times N$ sites, the number of two-particle basis set used to represent the system is $O(N^2)$ and the dimension of the matrix is $O(N^2 \times N^2)$. As most of the algorithms for eigen value computations scale like $O(n^3)$ for a $n \times n$ matrix, the computational cost of equation (5.49) scales like $O(N^6)$. To calculate one Green's function from equation (5.50), we need to compute the inner product of two vectors N^2 times, which costs $O(N^6)$ operations in total. So the total cost of the the brute-force approach is $O(N^6)$. In contrast, the recursive method is much more efficient. Out of all the vectors \mathbf{V}_K , \mathbf{V}_{K_c} has the largest size which is about N . Thus the most time-consuming step would be solving equation (5.33), which requires a run time that scales like $O(N^3)$. Since there are about N similar equation to solve, the total computational cost would be $O(N^4)$ which is much less than the cost of brute-force approach. In addition, the recursive method yields N Green's functions at the same time.

The brute-force approach is not often used in computations. Instead, the recursion method developed by Haydock [109, 110] is most widely used. For comparison purpose, we give a very brief description of the method and compare it with our method. The main idea of Haydock's method is to generate a series of orthonormal vectors $|u_0\rangle, |u_1\rangle, |u_2\rangle, \dots$ from the iterations

$$H|u_n\rangle = b_n^*|u_{n-1}\rangle + a_n|u_n\rangle + b_{n+1}|u_{n+1}\rangle \quad (5.51)$$

calculate the value of a_n and b_n until convergence. Because the Hamiltonian matrix is tridiagonal in this basis, the Green's functions can be expressed in term of a_n and b_n :

$$\langle u_0 | \hat{G}(z) | u_0 \rangle = \frac{1}{z - a_0 - \frac{|b_1|^2}{z - a_1 - \dots}}. \quad (5.52)$$

For a tight-binding model with only the nearest-neighbor interaction, those vectors $|u_n\rangle$ is a linear combination of local states $|\mathbf{R}\rangle$ with particles reside at \mathbf{R} . The

Hamiltonian has the following useful feature:

$$H|\mathbf{R}\rangle = \mathbf{t}_{\mathbf{R},\mathbf{R}-\mathbf{1}}|\mathbf{R}-\mathbf{1}\rangle + h_{\mathbf{R},\mathbf{R}}|\mathbf{R}\rangle + \mathbf{t}_{\mathbf{R},\mathbf{R}+\mathbf{1}}|\mathbf{R}+\mathbf{1}\rangle , \quad (5.53)$$

where $h_{\mathbf{R},\mathbf{R}}$ is the on-site energy and \mathbf{t} are hopping terms, and $|\mathbf{R}-\mathbf{1}\rangle$ and $|\mathbf{R}+\mathbf{1}\rangle$ denote the states whose particles positions are 1 site different from that of $|\mathbf{R}\rangle$. As a specific example, equation (5.10) clearly demonstrates this property of the local state $|\mathbf{R}\rangle = |n\rangle|m\rangle$. As a result of equation (5.53), to calculate $G(\mathbf{R},\mathbf{R};z)$, we can initiate the recursion by setting $|u_0\rangle = |\mathbf{R}\rangle$ and $b_0 = 0$. Assuming orthonormality of local states, a_0 can be obtained by taking the product of $\langle u_0|$ with equation (5.51),

$$a_0 = \langle u_0|H|u_0\rangle = h_{\mathbf{R},\mathbf{R}} . \quad (5.54)$$

Compare equation (5.51) with equation (5.53), we can easily see that and $|u_1\rangle$ is a superposition of $|\mathbf{R}-\mathbf{1}\rangle$ and $|\mathbf{R}+\mathbf{1}\rangle$ and b_1 can be computed by requiring $|u_1\rangle$ to be normalized. To continue the recursion, we take $n = 1$ in equation (5.51) to obtain

$$H|u_1\rangle = b_1^*|u_0\rangle + a_1|u_1\rangle + b_2|u_2\rangle \quad (5.55)$$

and let H operates on $|u_1\rangle$, a superposition of $|\mathbf{R}-\mathbf{1}\rangle$ and $|\mathbf{R}+\mathbf{1}\rangle$, according to equation (5.53), which gives rise to a linear combination of $|\mathbf{R}-\mathbf{2}\rangle$, $|\mathbf{R}-\mathbf{1}\rangle$, $|\mathbf{R}\rangle$, $|\mathbf{R}+\mathbf{1}\rangle$ and $|\mathbf{R}-\mathbf{2}\rangle$ on the left hand side of equation (5.55). Now it is clear that $|u_2\rangle$ will also be a superposition of $|\mathbf{R}-\mathbf{2}\rangle$, $|\mathbf{R}-\mathbf{1}\rangle$, $|\mathbf{R}\rangle$, $|\mathbf{R}+\mathbf{1}\rangle$ and $|\mathbf{R}-\mathbf{2}\rangle$, and b_2 can be calculated from the normalization condition of $|u_2\rangle$. Follow the above analysis, we conclude that $|u_n\rangle$ is a superposition of these local states: $|\mathbf{R}-\mathbf{n}\rangle$, $|\mathbf{R}-\mathbf{n}+1\rangle$, \dots , $|\mathbf{R}+\mathbf{n}-1\rangle$ and $|\mathbf{R}+\mathbf{n}\rangle$, which are within n -sites distance from \mathbf{R} .

Haydock's method and our method both rely on recursive calculations, but they differ a lot in numerical efficiency. Take the calculation of two-particle Green's function as an example, if Haydock's method terminates the recursion at step N , it has to deal with vectors of size up to $\sim N^2$. Equivalently, to employ the same number of local states as in Haydock's method, our method set $\mathbf{A}_{2N+1} = 0$ and $\tilde{\mathbf{A}}_1 = 0$, and the largest size of vectors is about N , which is much smaller. Therefore our method involves much smaller matrices and can handle much larger crystal size.

5.4 The tunneling of biexciton state through disorders

The recursive method to calculate Green's function in Section 5.3 is more computational. Green's function has many applications in condensed matter physics. has the potential to In this section, we use the Green's function to study the tunneling of a biexciton state through disorders.

Chapter (3) shows that a biexciton is a correlated state of two excitations and its wavefunction is given by

5.5 Conclusion

In summary

Bibliography

- [1] Jan R Kuklinski and Shaul Mukamel. Optical properties of wannier excitons in the linear and weakly nonlinear regime. *Physical Review B*, 42(5):2959, 1990. → pages 14
- [2] Christoph Schindler and Roland Zimmermann. Analysis of the exciton-exciton interaction in semiconductor quantum wells. *Physical Review B*, 78(4):045313, 2008. → pages 14
- [3] Vladimir Agranovich. Excitations in organic solids. 2009. → pages 14, 15, 16, 49, 57, 70
- [4] P. L. Gourley and J. P. Wolfe. Experimental determination of equilibrium constants for excitonic systems in stressed, ultrapure silicon. *Physical Review B*, 25(10):6338, 1982. → pages 14
- [5] M. L. W. Thewalt and W. G. McMullan. Green and near-infrared luminescence due to the biexcitons in unperturbed silicon. *Physical Review B*, 30(10):6232, 1984. → pages
- [6] J. C. Kim, D. R. Wake, and J. P. Wolfe. Thermodynamics of biexcitons in a gaas quantum well. *Physical Review B*, 50(20):15099, 1994. → pages
- [7] R. C. Miller, D. A. Kleinman, A. C. Gossard, and O. Munteanu. Biexcitons in gaas quantum wells. *Physical Review B*, 25(10):6545, 1982. → pages
- [8] R. Cingolani, Y. Chen, and K. Ploog. Biexciton formation in gaas/alxga1-xas multiple quantum wells: An optical investigation. *Physical review. B, Condensed matter*, 38(18):13478–13481, 1988. → pages
- [9] R. M. Stevenson, R. J. Young, P. Atkinson, K. Cooper, D. A. Ritchie, and A. J. Shields. A semiconductor source of triggered entangled photon pairs. *Nature*, 439(7073):179–182, 2006. → pages

- [10] Svatoslav Anatol'evič Moskalenko and David W Snoke. Bose-einstein condensation of excitons and biexcitons: and coherent nonlinear optics with excitons. 2000. → pages 14
- [11] G. Vektoris. A new approach to the molecular biexciton theory. *The Journal of chemical physics*, 101:3031, 1994. → pages 14, 32
- [12] Hiromi Ezaki, Tetsuji Tokihiro, and Eiichi Hanamura. Excitonic n-string in linear chains: Electronic structure and optical properties. *Physical Review B*, 50(15):10506, 1994. → pages 36
- [13] Francis C Spano, Vladimir Agranovich, and Shaul Mukamel. Biexciton states and two-photon absorption in molecular monolayers. *The Journal of chemical physics*, 95:1400, 1991. → pages
- [14] Vladimir Moiseevich Agranovich and Mikhail D Galanin. Electron-excitation energy transfer in condensed media. *Moscow Izdatel Nauka*, 1, 1978. → pages 14, 32
- [15] Y Baba, G Dujardin, P Feulner, and D Menzel. Formation and dynamics of exciton pairs in solid argon probed by electron-stimulated ion desorption. *Physical review letters*, 66(25):3269, 1991. → pages 14
- [16] P. Wiethoff, B. Kassühlke, D. Menzel, and P. Feulner. Biexcitons in solid neon. *Low Temperature Physics*, 29:266, 2003. → pages 14
- [17] T Volz, N Syassen, DM Bauer, E Hansis, S Dürr, and G Rempe. Preparation of a quantum state with one molecule at each site of an optical lattice. *Nature Physics*, 2(10):692–695, 2006. → pages 14, 15
- [18] Johann G Danzl, Manfred J Mark, Elmar Haller, Mattias Gustavsson, Russell Hart, Jesus Aldegunde, Jeremy M Hutson, and Hanns-Christoph Nägerl. An ultracold high-density sample of rovibronic ground-state molecules in an optical lattice. *Nature Physics*, 6(4):265–270, 2010. → pages
- [19] Amodsen Chotia, Brian Neyenhuis, Steven A Moses, Bo Yan, Jacob P Covey, Michael Foss-Feig, Ana Maria Rey, Deborah S Jin, and Jun Ye. Long-lived dipolar molecules and feshbach molecules in a 3d optical lattice. *Physical Review Letters*, 108(8):080405, 2012. → pages 14, 15
- [20] Felipe Herrera, Marina Litinskaya, and Roman V Krems. Tunable disorder in a crystal of cold polar molecules. *Physical Review A*, 82(3):033428, 2010. → pages 14, 15, 16, 35, 57, 72, 78, 82, 102, 103, 124

- [21] Gregory D Scholes and Garry Rumbles. Excitons in nanoscale systems. *Nature materials*, 5(9):683–696, 2006. → pages 14
- [22] R. M. Rajapakse, Timothy Bragdon, Ana Maria Rey, T. Calarco, and S. F. Yelin. Single-photon nonlinearities using arrays of cold polar molecules. *Physical Review A*, 80(1):013810, 2009. → pages 14
- [23] P Rabl, D DeMille, JM Doyle, MD Lukin, RJ Schoelkopf, and P Zoller. Hybrid quantum processors: molecular ensembles as quantum memory for solid state circuits. *Physical review letters*, 97(3):033003, 2006. → pages 14, 47, 102
- [24] P Rabl and P Zoller. Molecular dipolar crystals as high-fidelity quantum memory for hybrid quantum computing. *Physical Review A*, 76(4):042308, 2007. → pages 14, 47, 102
- [25] Ryan Barnett, Dmitry Petrov, Mikhail Lukin, and Eugene Demler. Quantum magnetism with multicomponent dipolar molecules in an optical lattice. *Physical review letters*, 96(19):190401, 2006. → pages 14, 47
- [26] A Micheli, GK Brennen, and P Zoller. A toolbox for lattice-spin models with polar molecules. *Nature Physics*, 2(5):341–347, 2006. → pages 14
- [27] Gavin K Brennen, Andrea Micheli, and Peter Zoller. Designing spin-1 lattice models using polar molecules. *New Journal of Physics*, 9(5):138, 2007. → pages
- [28] H. P. Büchler, A. Micheli, and P. Zoller. Three-body interactions with cold polar molecules. *Nature Physics*, 3(10):726–731, 2007. → pages 14
- [29] Michael L Wall and Lincoln D Carr. Emergent timescales in entangled quantum dynamics of ultracold molecules in optical lattices. *New Journal of Physics*, 11(5):055027, 2009. → pages
- [30] ML Wall and LD Carr. Hyperfine molecular hubbard hamiltonian. *Physical Review A*, 82(1):013611, 2010. → pages
- [31] C Trefzger, M Alloing, C Menotti, F Dubin, and M Lewenstein. Quantum magnetism and counterflow supersolidity of up–down bosonic dipoles. *New Journal of Physics*, 12(9):093008, 2010. → pages
- [32] JP Kestner, Bin Wang, Jay D Sau, and S Das Sarma. Prediction of a gapless topological haldane liquid phase in a one-dimensional cold polar molecular lattice. *Physical Review B*, 83(17):174409, 2011. → pages

- [33] Alexey V Gorshkov, Salvatore R Manmana, Gang Chen, Jun Ye, Eugene Demler, Mikhail D Lukin, and Ana Maria Rey. Tunable superfluidity and quantum magnetism with ultracold polar molecules. *Physical review letters*, 107(11):115301, 2011. → pages 14
- [34] Alexey V Gorshkov, Salvatore R Manmana, Gang Chen, Eugene Demler, Mikhail D Lukin, and Ana Maria Rey. Quantum magnetism with polar alkali-metal dimers. *Physical Review A*, 84(3):033619, 2011. → pages 14, 47
- [35] David DeMille. Quantum computation with trapped polar molecules. *Physical Review Letters*, 88(6):067901, 2002. → pages 14, 45, 50, 101
- [36] At zero electric field, there are three degenerate states corresponding to $N = 1$ and $M_N = 0, \pm 1$. In the presence of an electric field relevant for this study, the degeneracy is lifted. As shown in Ref. [20], the $|N = 0\rangle \rightarrow |N = 1, M_N = 0\rangle$ transition is uncoupled from the $|N = 0\rangle \rightarrow |N = 1, M_N = \pm 1\rangle$ transitions. The $M_N = \pm 1$ states can, therefore, be ignored. → pages 15
- [37] John M Brown and Alan Carrington. *Rotational spectroscopy of diatomic molecules*. Cambridge University Press, 2003. → pages 16
- [38] Eleftherios N. Economou. *Green's Functions in Quantum Physics*. Springer, 3 edition, 2006. → pages 28, 110
- [39] This analysis assumes that both D and J are isotropic. For molecules on an optical lattice, the magnitude and sign of D and J depend on the angle between the direction of the electric field and the molecular array. This may modify the properties of biexcitons in 2D and 3D systems. → pages 32
- [40] N. A. Efremov and E. P. Kaminskaya. "title". 15, 1973. → pages 36
- [41] Felipe Herrera and Roman V Krems. Tunable holstein model with cold polar molecules. *Physical Review A*, 84(5):051401, 2011. → pages 45
- [42] AA Ovchinnikov. Pis' ma zh. eksp. teor. fiz., 5 (1967). *JETP Lett*, 5:38, 1967. → pages 45
- [43] Herbert Van Amerongen, Leonas Valkūnas, and Rienk Van Grondelle. *Photosynthetic excitons*. World Scientific, 2000. → pages 45
- [44] Robert E Blankenship. *Molecular mechanisms of photosynthesis*. Wiley. com, 2008. → pages

- [45] Akihito Ishizaki and Graham R Fleming. Theoretical examination of quantum coherence in a photosynthetic system at physiological temperature. *Proceedings of the National Academy of Sciences*, 106(41):17255–17260, 2009. → pages 45
- [46] Michael Köhl, Henning Moritz, Thilo Stöferle, Kenneth Günter, and Tilman Esslinger. Fermionic atoms in a three dimensional optical lattice: Observing fermi surfaces, dynamics, and interactions. *Physical review letters*, 94(8):080403, 2005. → pages 47
- [47] D McKay, M White, M Pasienski, and B DeMarco. Phase-slip-induced dissipation in an atomic bose–hubbard system. *Nature*, 453(7191):76–79, 2008. → pages
- [48] Robert Jördens, Niels Strohmaier, Kenneth Günter, Henning Moritz, and Tilman Esslinger. A mott insulator of fermionic atoms in an optical lattice. *Nature*, 455(7210):204–207, 2008. → pages 47
- [49] U Schneider, L Hackermüller, and S Will. Th. best, i. bloch, ta costi, rw helmes, d. rasch and a. rosch. 2008. metallic and insulating phases of repulsively interacting fermions in a 3d optical lattice. *Science*, 322:1520–1525, 2008. → pages 47
- [50] Ping Xiang, Marina Litinskaya, and Roman V Krems. Tunable exciton interactions in optical lattices with polar molecules. *Physical Review A*, 85(6):061401, 2012. → pages 47, 57, 82, 102
- [51] Markus Greiner, Olaf Mandel, Tilman Esslinger, Theodor W Hänsch, and Immanuel Bloch. Quantum phase transition from a superfluid to a mott insulator in a gas of ultracold atoms. *Nature*, 415(6867):39–44, 2002. → pages 47
- [52] Mikhail Lemeshko, Roman V Krems, and Hendrik Weimer. Nonadiabatic preparation of spin crystals with ultracold polar molecules. *Physical Review Letters*, 109(3):035301, 2012. → pages 47
- [53] David P DiVincenzo. The physical implementation of quantum computation. *Fortschr. Phys.*, 48:771, 2000. → pages 47
- [54] Alain Aspect and Massimo Inguscio. Anderson localization of ultracold atoms. *Physics today*, 62:30, 2009. → pages 47
- [55] Brian A Gregg. Excitonic solar cells. *The Journal of Physical Chemistry B*, 107(20):4688–4698, 2003. → pages 47

- [56] Tamar Seideman and Edward Hamilton. Nonadiabatic alignment by intense pulses. concepts, theory, and directions. *Advances in atomic, molecular, and optical physics*, 52:289–329, 2005. → pages 48, 54
- [57] Igor V Litvinyuk, Kevin F Lee, Patrick W Dooley, David M Rayner, David M Villeneuve, and Paul B Corkum. Alignment-dependent strong field ionization of molecules. *Physical review letters*, 90(23):233003, 2003. → pages
- [58] SM Purcell and PF Barker. Tailoring the optical dipole force for molecules by field-induced alignment. *Physical review letters*, 103(15):153001, 2009. → pages
- [59] E Gershkabel, M Shapiro, and I Sh Averbukh. Stern-gerlach deflection of field-free aligned paramagnetic molecules. *The Journal of chemical physics*, 135(19):194310–194310, 2011. → pages 48
- [60] Uri Steinitz, Yehiam Prior, and Ilya Sh Averbukh. Laser induced gas vortices. *arXiv preprint arXiv:1202.2698*, 2012. → pages 48
- [61] Yuri Khodorkovsky, JR Manson, and Ilya Sh Averbukh. Modifying molecule-surface scattering by ultrashort laser pulses. *Physical Review A*, 84(5):053420, 2011. → pages 48
- [62] J Hecker Denschlag, JE Simsarian, H Häffner, C McKenzie, A Browaeys, D Cho, K Helmerson, SL Rolston, and WD Phillips. A bose-einstein condensate in an optical lattice. *Journal of Physics B: Atomic, Molecular and Optical Physics*, 35(14):3095, 2002. → pages 48
- [63] Hashem Zoubi and Helmut Ritsch. Excitons and cavity polaritons for ultracold atoms in an optical lattice. *Physical Review A*, 76(1):013817, 2007. → pages 48, 71
- [64] Hashem Zoubi and Helmut Ritsch. Lifetime and emission characteristics of collective electronic excitations in two-dimensional optical lattices. *Physical Review A*, 83(6):063831, 2011. → pages 48, 69, 70
- [65] H Zoubi and H Ritsch. Metastability and directional emission characteristics of excitons in 1d optical lattices. *EPL (Europhysics Letters)*, 90(2):23001, 2010. → pages 48, 69, 70
- [66] MHS Amin. Consistency of the adiabatic theorem. *arXiv preprint arXiv:0810.4335*, 2008. → pages 53

- [67] Mark Raizen, Christophe Salomon, and Qian Niu. New light on quantum transport. *Physics today*, 50, 1997. → pages 54
- [68] Marina Litinskaya and Roman V Krems. Rotational excitations of polar molecules on an optical lattice: from novel exciton physics to quantum simulation of new lattice models. In K. W. Madison, Y. Wang, A. M. Rey, and K. Bongs, editors, *Annual Review of Cold Atoms and Molecules*, volume 1, page 53. World Scientific Publishing Company, Singapore, 2012. → pages 57
- [69] V. M. Agranovich, O. A. Dubovskiy, D. M. Basko, G. C. La Rocca, and F. Bassani. Kinematic frenkel biexcitons. *Journal of luminescence*, 85(4):221–232, 2000. → pages 57
- [70] Annie Cuyt, Vigdis Petersen, Brigitte Verdonk, Haakon Waadeland, and William B. Jones. *Handbook of continued fractions for special functions*. Springer, 2008. → pages 58
- [71] Fedorov. *Atomic and free electrons in a strong light field*. World Scientific, Singapore, 1997. → pages 60, 71
- [72] Joseph W Goodman and Steven C Gustafson. Introduction to fourier optics. *Optical Engineering*, 35(5):1513–1513, 1996. → pages 60
- [73] Jacob F Sherson, Christof Weitenberg, Manuel Endres, Marc Cheneau, Immanuel Bloch, and Stefan Kuhr. Single-atom-resolved fluorescence imaging of an atomic mott insulator. *Nature*, 467(7311):68–72, 2010. → pages 69, 71, 93
- [74] Waseem S Bakr, Amy Peng, M Eric Tai, Ruichao Ma, Jonathan Simon, Jonathon I Gillen, Simon Foelling, Lode Pollet, and Markus Greiner. Probing the superfluid-to-mott insulator transition at the single-atom level. *Science*, 329(5991):547–550, 2010. → pages
- [75] Waseem S Bakr, Philipp M Preiss, M Eric Tai, Ruichao Ma, Jonathan Simon, and Markus Greiner. Orbital excitation blockade and algorithmic cooling in quantum gases. *Nature*, 480(7378):500–503, 2011. → pages 71, 93
- [76] Amodsen Chotia, Brian Neyenhuis, Steven A Moses, Bo Yan, Jacob P Covey, Michael Foss-Feig, Ana Maria Rey, Deborah S Jin, and Jun Ye. Long-lived dipolar molecules and feshbach molecules in a 3d optical lattice. *Physical Review Letters*, 108(8):080405, 2012. → pages 69, 93

- [77] Rudolf Grimm, Matthias Weidemüller, and Yurii B Ovchinnikov. Optical dipole traps for neutral atoms. *Advances in atomic, molecular, and optical physics*, 42:95–170, 2000. → pages 69
- [78] V. M. Agranovich and O. A. Dubovskii. Effect of retarded interaction on the exciton spectrum in one-dimensional and two-dimensional crystals. *JETP Letters*, 3:223, 1966. → pages 70
- [79] H. Zoubi and H. Ritsch. Excitons and cavity polaritons for optical lattice ultracold atoms. *Advances in Atomic, Molecular, and Optical Physics*, 62:171, 2013. → pages 71
- [80] Bretislav Friedrich and Dudley Herschbach. Polarization of molecules induced by intense nonresonant laser fields. *The Journal of Physical Chemistry*, 99(42):15686–15693, 1995. → pages 72
- [81] Lincoln D Carr, David DeMille, Roman V Krems, and Jun Ye. Cold and ultracold molecules: science, technology and applications. *New Journal of Physics*, 11(5):055049, 2009. → pages 79
- [82] Jesus Pérez-Ríos, Felipe Herrera, and Roman V Krems. External field control of collective spin excitations in an optical lattice of 2σ molecules. *New Journal of Physics*, 12(10):103007, 2010. → pages 93
- [83] IM Vellekoop and AP Mosk. Focusing coherent light through opaque strongly scattering media. *Optics letters*, 32(16):2309–2311, 2007. → pages 95, 98
- [84] SM Popoff, G Lerosey, R Carminati, M Fink, AC Boccara, and S Gigan. Measuring the transmission matrix in optics: an approach to the study and control of light propagation in disordered media. *Physical review letters*, 104(10):100601, 2010. → pages 98
- [85] I. M. Vellekoop, A. Lagendijk, and A. P. Mosk. Exploiting disorder for perfect focusing. *Nature Photonics*, 4(5):320–322, 2010. → pages
- [86] T. Cizmar, M. Mazilu, and K. Dholakia. In situ wavefront correction and its application to micromanipulation. *Nature Photonics*, 4(6):388–394, 2010. → pages
- [87] Ori Katz, Eran Small, Yaron Bromberg, and Yaron Silberberg. Focusing and compression of ultrashort pulses through scattering media. *Nature photonics*, 5(6):372–377, 2011. → pages

- [88] David J McCabe, Ayhan Tajalli, Dane R Austin, Pierre Bondareff, Ian A Walmsley, Sylvain Gigan, and Béatrice Chatel. Spatio-temporal focusing of an ultrafast pulse through a multiply scattering medium. *Nature Communications*, 2:447, 2011. → pages
- [89] Jochen Aulbach, Bergin Gjonaj, Patrick M Johnson, Allard P Mosk, and Ad Lagendijk. Control of light transmission through opaque scattering media in space and time. *Physical review letters*, 106(10):103901, 2011. → pages
- [90] Evgeny A Shapiro, Thomas M Drane, and Valery Milner. Prospects of coherent control in turbid media: Bounds on focusing broadband laser pulses. *Physical Review A*, 84(5):053807, 2011. → pages
- [91] Meng Cui. A high speed wavefront determination method based on spatial frequency modulations for focusing light through random scattering media. *Optics Express*, 19(4):2989–2995, 2011. → pages
- [92] Moonseok Kim, Youngwoon Choi, Changhyeong Yoon, Wonjun Choi, Jaisoon Kim, Q-Han Park, and Wonshik Choi. Maximal energy transport through disordered media with the implementation of transmission eigenchannels. *Nature photonics*, 6(9):583–587, 2012. → pages 95, 98
- [93] Joseph W Goodman. *Statistical optics*. John Wiley and Sons, New York, 2000. → pages 95
- [94] Zohar Amitay, Ronnie Kosloff, and Stephen R Leone. Experimental coherent computation of a multiple-input and gate using pure molecular superpositions. *Chemical physics letters*, 359(1):8–14, 2002. → pages 102
- [95] Ignacio R Sola, Vladimir S Malinovsky, and Jesus Santamaría. Implementing quantum gates on oriented optical isomers. *The Journal of chemical physics*, 120:10955, 2004. → pages
- [96] E. A. Shapiro, Michael Spanner, and Misha Yu Ivanov. Quantum logic in coarse grained control of wavepackets. *Journal of Modern Optics*, 52(6):897–915, 2005. → pages
- [97] Ulrike Troppmann and Regina de Vivie-Riedle. Mechanisms of local and global molecular quantum gates and their implementation prospects. *The Journal of chemical physics*, 122:154105, 2005. → pages

- [98] Eric Charron and Maurice Raoult. Phase information revealed by interferences in the ionization of rotational wave packets. *Physical Review A*, 74(3):033407, 2006. → pages
- [99] Yingying Gu and Dmitri Babikov. On the role of vibrational anharmonicities in a two-qubit system. *The Journal of chemical physics*, 131:034306, 2009. → pages 102
- [100] Alexander I Lvovsky, Barry C Sanders, and Wolfgang Tittel. Optical quantum memory. *Nature Photonics*, 3(12):706–714, 2009. → pages 102
- [101] AJ Daley, SR Clark, D Jaksch, and P Zoller. Numerical analysis of coherent many-body currents in a single atom transistor. *Physical Review A*, 72(4):043618, 2005. → pages 102
- [102] Roman V Krems. Cold controlled chemistry. *Physical Chemistry Chemical Physics*, 10(28):4079–4092, 2008. → pages 102
- [103] A. O. G. Wallis and R. V. Krems. Rotational predissociation of extremely weakly bound atom-molecule complexes produced by feshbach resonance association. *The Journal of chemical physics*, 135:124313, 2011. → pages 102
- [104] Felipe Herrera, Kirk W Madison, Roman V Krems, and Mona Berciu. Investigating polaron transitions with polar molecules. *Physical Review Letters*, 110(22):223002, 2013. → pages 102, 103
- [105] Z. Zimboras, M. Faccin, Z. Kadar, J. Whitfield, B. Lanyon, and J. Biamonte. Quantum transport enhancement by time-reversal symmetry breaking. *Scientific Reports*, 3:2361, 2013. → pages 103
- [106] Mona Berciu and A. M. Cook. Efficient computation of lattice green's functions for models with nearest-neighbor hopping. *Europhysics Letters*, 92, 2010. → pages 104, 110
- [107] Mona Berciu. Few-particle green's functions for strongly correlated system on infinite lattices. *Physical Review Letters*, 107, 2011. → pages
- [108] M Möller, A Mukherjee, C. P. J. Adolphs, D. J. J. Marchand, and Mona Berciu. Efficient computation of lattice green functions for models with longer range hopping. *Journal of Physics A: Mathematical and Theoretical*, 45, 2012. → pages 104

- [109] R. Haydock, V. Heine, and Kelly M. J. Electronic structure based on the local atomic environment for tight-binding bands. *J. Phys. C: Solid State Phys.*, 5, 1972. → pages 118
- [110] R. Haydock, V. Heine, and Kelly M. J. Electronic structure based on the local atomic environment for tight-binding bands: II. *J. Phys. C: Solid State Phys.*, 8, 1975. → pages 118
- [111] Cornelius Lanczos. An iteration method for the solution of the eigenvalue problem of linear differential and integral operators. *Journal of Research of the National Bureau of Standards*, 4, 1950. → pages

Appendix A

Supporting Materials

This would be any supporting material not central to the dissertation. For example:

- Authorizations from Research Ethics Boards for the various experiments conducted during the course of research.
- Copies of questionnaires and survey instruments.